INVESTIGATION OF MINERAL AND COLLAGEN ORGANIZATION IN BONE USING RAMAN SPECTROSCOPY

by

Mekhala Raghavan

A dissertation submitted in partial fulfillment
of the requirements for the degree of
Doctor of Philosophy
(Biomedical Engineering)
in the University of Michigan
2011

Doctoral Committee:

Professor Michael D. Morris, Co-Chair
Professor David H. Kohn, Co-Chair
Associate Professor Mary-Ann Mycek
Assistant Professor Krishnakumar R. Garikipati

2011

Acknowledgements

Many people have helped bring this thesis to fruition. First, I thank my advisor Prof. Michael Morris for giving me the opportunity to work with him. He has been a wonderful mentor and under his guidance I have grown both personally and professionally. I owe much more to him than what is reflected in this thesis. I am thankful to my co-chair Prof. David Kohn for his valued council and guidance. This research could not have been carried out without both their advice and encouragement. Prof. Mary-Ann Mycek and Prof. Krishna Garikipati have been a source of much learning and stimulation and provided scientific guidance which has sharpened my work.

This dissertation has been the result of a truly collaborative effort. I would like to thank Nadder Sahar for his numerous contributions to the project. His work is an inspiration to me. I also received much help from Erin McNerny and Robert Wilson. Thanks are also due to Prof. Nancy Pleshko of Temple University for generously providing us bone specimens. My wonderful colleagues in the Raman group have been constantly supportive and encouraging. I appreciate all that Kurtulus Golcuk, Karen Esmonde-White, and Gurjit Mandair have taught me. I am grateful to Francis Esmonde-White, Kate Dooley, and Jacque Cole for always being ready to help and for many engaging

discussions. I also thank Arindam Ganguly, Peizhi Zhu, John-David McElderry and Paul Okagbare for their guidance and support.

The Biomedical Engineering and Chemistry departments were great collaborative places to work at. I would like to thank Zhen Xu and Malavika Chandra for their guidance early in my graduate school career. Maria Steele in the BME office and Kate Restrick at the Center for Global Health has always been helpful and supportive. I acknowledge financial support from the National Institutes of Health and the Barbour Scholarship from Rackham Graduate School.

Some friends deserve special mention for their help in matters personal and professional - Romila for her support from more than 8000 miles away and long years of friendship, and in Ann Arbor: Swapnaa, Sadashiv, Bala, Manickam, Abhishek, Khamir, and Arvind. Finally, love and gratitude to Amma, Appa, Madhura, and Raghu, who collectively supported this research in more ways than I can describe.

Table of Contents

List of Tables

Table

List of Figures

Figure

List of Appendices

Appendix

Abstract

The extraordinary toughness and stiffness of bone are associated with its three main constituents - apatite mineral, collagen protein and water. Variations in composition and organization of these constituents are known to exist as a function of disease and aging. These variations greatly influence bone quality and need to be understood in greater detail. This thesis advances the understanding of molecular organization in bone along three directions: quantification of molecular orientation, analysis of mineral deformation in response to hydration changes and loading and investigation of age-dependent bone quality.

First, polarized Raman spectroscopy was adapted for bone tissue applications to quantify molecular organization in non-deproteinated, turbid tissue. This enabled the simultaneous quantitative measurements of altered mineral and collagen orientations in Osteogenesis Imperfecta, a bone disease associated with collagen mutations. Second, the effect of distorting the water environment in bone was investigated by replacing matrix water with deuterium oxide. Changes in hydrogen bonding affected collagen secondary structure, resulting in compression of the mineral lattice as evidenced by changes in peak positions and widths of mineral Raman bands. Further, polarized Raman spectroscopy was used to probe nano-scale deformations due to tensile loading and orientation-dependent strains

within the mineral lattice were observed. These results demonstrate the potential of Raman spectroscopy to provide insights on molecular orientation and interaction at the nano-scale.

Third, exploratory data mining tools were employed to identify tissue-level compositional (Raman) and mechanical (nanoindentation) metrics that predict bone quality, instead of the traditionally used linear regressions. The results showed that compositional properties offer only a partial understanding of mechanical properties at the tissue-level and vice versa. Hence, a specific combination of compositional and mechanical metrics was required to reliably classify femoral specimens according to age. These findings suggest that combined metrics will better predict transformations in bone quality than individual metrics and call for novel techniques to explore the complex multi-scale interactions in bone. The multiple lines of evidence presented in this thesis provide an insight into the complex roles that mineral, collagen and water play in governing tissue quality and mechanical properties of bone.

CHAPTER 1

Introduction

In this thesis, we explore the application of Raman spectroscopy to understand molecular organization in bone tissue. A method to quantify bone mineral and collagen orientations is developed to understand the molecular mechanisms of genetic disorder in bone. The role of water in bone is investigated by studying the effects of distorting the aqueous environment on the composition and orientation of bone mineral and collagen. Orientation-dependent mineral behavior in response to tensile loading of bone is studied to understand the molecular mechanisms in bone under stress. Finally, the contributions of tissue-level compositional and mechanical properties to bone quality are analyzed using exploratory data analysis tools.

1.1 Bone composition

Bone is a heterogeneous and hierarchical material composed primarily of collagen fibrils, mineral crystals and water [1]. The collagen component gives the bone material its compliance and the ability to dissipate energy under load. This organic matrix is primarily made up of type I collagen fibrils in a hydrated environment. Tropocollagen molecules assemble into triple helices that are bound together to form collagen fibrils. Cross-links join several fibrils together and therefore, are important for mechanical

strength of mature bone tissue [2]. As the bone tissue grows and matures, nanometer sized mineral crystallites are formed in the gaps between the collagen fibrils and then grow into the fibril overlap zones. The crystallites are highly substituted, poorly crystalline carbonated apatite and impart stiffness to the tissue [3]. By combining the high toughness of collagen and the high stiffness of mineral, bone achieves its remarkable mechanical properties. The third significant component is water which facilitates solute transport, contributes to viscoelastic properties and plays a key role during mineralization. Water exists on the surface of mineral crystallites, within the crystallites and in between collagen fibers [4]. The three major components are associated into the basic building block of bone, the mineralized collagen fibril. At the microscale, mineralized collagen fibrils make up fiber bundles, which are in turn arranged into lamellae. At the next higher scale are osteons and trabeculae which make up the cortical and cancellous regions of the bone. The composite nature of the material and the spatial relationship between the three components at different length scales contribute to bone's remarkable resistance to fracture [5]. However, the interactions between mineral, collagen and water are not yet fully understood.

1.2 Bone quality

Degradation of bone tissue with age and disease can be considered in terms of bone quality [6]. One aspect of bone quality is bone mass or bone mineral density (BMD), which is the current clinical standard for predicting fracture risk. Non-BMD parameters such as chemical composition, mineralization, architectural properties, material properties, remodeling and microdamage also influence the bone's resistance to fracture.

Studies have demonstrated that BMD alone does not reliably predict whether or not a patient will fracture [7, 8]. However, at present, there are no accepted measures of bone quality (a single measure or a combination of measures) that will fully characterize bone structural integrity or predict risk of fracture with great accuracy. Hence, it is important to understand bone tissue properties at various hierarchical scales and develop biomarkers combining information about different properties for improved prediction of the occurrence of fracture.

1.3 Raman spectroscopic characterization of bone

Raman microspectroscopy has been established as a versatile tool for compositional analysis at the micron-scale spatial resolution in bone tissue. In Raman spectroscopy, a form of inelastic light scattering, an exciting laser photon interacts with a sample causing light to be scattered at a new, lower frequency which is determined by the energy of its characteristic molecular vibrations [9]. Hence, the Raman spectral band positions are specific to particular chemical groups. Raman spectroscopy is non-destructive, compatible with aqueous solutions, wet and thick specimens, glass and fused silica containers and its spectral resolution approaches that of light microscopy. For these reasons, Raman spectroscopy has proved to be an exceedingly powerful tool for the characterization of bone tissue.

The Raman spectra of bone tissue provide us with much information about the structure and composition of the mineral and collagen constituents of bone [10, 11]. Figure 1.1 gives a general view of the Raman spectra from a bone sample showing the major

mineral and matrix bands. The phosphate ν_1 band at ~960 cm^{-1} and the B-type carbonate ν_1 band at ~1070 cm^{-1} are the important Raman mineral bands. The band positions, heights and shapes of the phosphate and carbonate bands report on mineral parameters such as crystal structure, crystallite size and deviations from stoichiometry [12, 13]. These bands respond to local perturbations of the mineral structure resulting from mechanical deformation, genetic defects or disease. The important Raman collagen bands are the amide I envelope at ~1660-1680 cm^{-1}, the hydroxyproline bands at 855 cm^{-1} and 875 cm^{-1}, the amide III envelope at 1245-1270 cm^{-1} and the methylene wag at 1450 cm^{-1}. The band positions, intensities and widths of these matrix bands are sensitive to changes in protein secondary structure and changes in collagen hydrogen bonding. Bone composition can be studied using four Raman metrics: mineral to matrix ratio (MMR), mineral crystallinity, carbonate to phosphate ratio and collagen crosslinking. MMR which is a measure of the mineral content in bone is calculated as the ratio of band height or area of the phosphate ν_1 band to that of amide I or hydroxyproline band. Mineral crystallinity is calculated from the width of the phosphate ν_1 band and is considered to be an indicator of mineral crystal size and also depends on disorder and strain in the crystallites [14]. Carbonate to phosphate ratio is calculated as the intensity ratio of the carbonate ν_1 to phosphate ν_1 peaks and denotes the carbonate content of the mineral in the bone specimen. Collagen crosslinking is the area or height ratio of amide I 1680 cm^{-1} component to the 1660 cm^{-1} component.

Raman spectroscopy has been used to study tissue mineralization, a physiological process where carbonated apatite is deposited in collagenous matrix of bone. Raman spectroscopy

confirmed the presence of an octacalcium phosphate like mineral in newly mineralized tissue [15] and has been used, more recently, to study mineral formation kinetics in cell cultures and fetal mouse skulls [16].

Raman spectroscopy has been applied to study age-related changes in bone material composition [17-19]. A combined mechanical testing and Raman spectroscopic study on human bones reported changes in the degree of collagen crosslinking with age [18]. These changes in crosslinking were correlated to a dramatic decrease in the resistance of bone to crack initiation and propagation. Spectroscopic abnormalities have been reported in bones from *Brtl* and *oim/oim* mice, which are models for osteogenesis imperfecta [20, 21]. Compositional differences have been observed between osteoporotic bones and matched controls [22, 23] .

1.4 Polarized Raman spectroscopy of bone

The remarkable mechanical properties of bone tissue are related to its structural organization. The conformation, orientation and arrangement of its molecular components at all different hierarchical levels are adapted to meet a wide variety of mechanical challenges [24-26]. Polarization of Raman scatter has the additional capacity to provide information on the structure and orientation of the molecular components of bone. Phosphate ν_1 and amide I Raman bands are sensitive to molecular orientation and polarization direction of incident light. The intensities of the mineral Raman bands are sensitive to the orientation of the crystallite c-axis with respect to the polarization of the

incident light. The amide I band, which is associated with the C=O stretching vibration, is more intense in the direction perpendicular to the collagen fiber axis.

Polarized Raman spectroscopy has been recently used to provide qualitative orientation information on bone molecular components. Kazanci et al. pioneered the investigation of molecular arrangement and composition in human osteons using polarized Raman spectroscopy [27]. They showed that mineral to matrix intensity ratios are influenced by both chemical composition and molecular orientation. A follow up study using polarized Raman analysis distinguished between orientation and composition changes in lamellar bone specimens [28]. Recently, spatial changes in molecular composition and orientation in the Haversian bone structure have been analyzed [29].

Polarized Raman spectroscopy can also be used to quantify the orientation distribution of molecules [30]. Unfortunately, measuring the molecular order is more complex from an experimental and theoretical point of view, compared to qualitative orientation analysis. Not surprisingly, no quantitative Raman spectroscopic measurements of molecular order in bone have been performed. X-ray diffraction studies in bone tissue provide direct measures of the molecular orientation distribution function which are, however, limited to the crystalline regions (mineral) of the sample [31]. Although polarized Raman spectroscopy yields only the orientation averages and not the distribution function directly, it can provide information on both crystalline and non-crystalline regions of the sample. Further, this technique offers a more accurate estimation of the orientation distribution function compared to polarized infrared spectroscopy.

Hence, we wanted to develop a quantitative polarized Raman spectroscopic technique for bone tissue applications. The molecular orientation functions for mineral and collagen components would be useful in establishing structure-function properties and providing a detailed understanding of deformation and disorder mechanisms at the microscale. In chapter 2, we describe the application of polarized Raman spectroscopy to study molecular orientations in bone tissue. We also explain overcoming experimental constraints that concern the choice of objective lens and the optical properties of the sample. We validated the technique by measuring orientation distribution functions in genetically disordered bone specimens for which X-ray diffraction measurements of orientation have been previously reported.

1.5 Age-related changes in bone micro-scale properties

The risk of bone fracture markedly increases with aging [32]. To understand the skeletal changes that occur in healthy bone tissue with ageing, it is necessary to study composition-function relationships at the macro-, micro- and nano-scales. While it is apparent that changes in chemical composition will be reflected in changes in mechanical properties at the tissue level, the specific relation between tissue level material properties is not fully understood. Nanoindentation and Raman spectroscopy are well suited to test the mechanical and chemical properties at the micro- and nano-scale of the material. Nanoindentation testing involves pressing a hard and stiff 50-nm diamond tip on the surface of a bone specimen and measuring simultaneously the load and deformation with micro-Newton and nanometer resolution. Because the mineral content and anisotropy of bone can vary at the microscale, nanoindentation provides insight into the spatial

distribution of mechanical properties at such small size scales [33]. Raman spectroscopy provides a complementary approach to nanoindentation by allowing comparison of chemical and mechanical properties at a similar spatial scale.

While there has been substantial progress in characterizing compositional changes with age, only a small number of studies have examined relationships between tissue composition and nanomechanical properties [34-37]. However, in these studies, spectroscopic and indentation measurements were performed on dehydrated bone specimens embedded in epoxy or resin to facilitate sample preparation. It is well known that sample processing affects the mechanical and compositional properties of bone tissue [38, 39]. Also, indentation studies on dehydrated and embedded bones have reported significant increases in indentation modulus [40, 41]. Therefore, it is important to conduct these measurements on hydrated tissue considering the viscoelastic and time-dependent deformation properties of bone. In chapter 3, we explore changes in nanomechanical properties and tissue composition between young mice that are skeletally mature and old mice that have compromised skeletal integrity. Co-localization of Raman spectroscopy and nanoindentation testing on hydrated cortical bones provided measurements at similar length scales, at the same spatial location and at similar depth.

Traditionally, studies often use univariate analysis and modeling of linear variable interactions to offer straightforward correlations between tissue composition and mechanical properties. However, the organization of bone is quantitatively complex at many scales of time and space and its mechanical and structural properties are not simply

the sum of the individual mineral and collagen components [42]. The system is more than the sum of its parts. The Raman and nanoindentation measurements which reflect bone material properties at the micro- and nano-scale are likely to exhibit multivariate dependencies and non-linear interactions. Much of the existing studies use traditional correlation and regression based methods which do not capitalize on the nature of multivariate and non-linear associations between different measured variables. Also, the direction of dependencies between composition and mechanical properties is unclear. Hence, considering correlation measures alone may provide an incomplete understanding of structure – function relationships in bone. Given the functional complexity and poorly understood nature of bone quality, data mining approaches are needed to analyze biologically relevant models or patterns from the underlying data. The advantage of machine learning and data mining is that no assumptions about linearity or interaction effects are needed. Such approaches will offer insight into how changes in bone quality (composition, mechanics, orientation, microdamage, etc) increase or decrease the risk of bone fracture through complex networks of molecular components that are hierarchically organized, highly interactive.

In chapter 3, we describe the use of non-linear, multivariate visualization and classification algorithms, RadViz and VizRank, to identify a set of compositional and mechanical properties that will predict age-related skeletal changes. These algorithms were chosen because of their ability to combine visualization and mining to provide interpretable predictive models whose biological relevance can be easily understood [43].

We used the open source Orange data mining suite (http://www.ailab.si/orange/) to implement the algorithms through an easy-to-use graphical interface.

1.6 Influence of water on collagen – mineral interactions

Bone tissue has a significant water component that influences its mechanical and structural properties and has been observed to decrease with age [44-47]. Water in bone is distributed as water bound to collagen and mineral crystallites [4] and as mobile water in the microscopic pores such as canaliculi, lacunae and Haversian canals [48]. It is well known that water plays an important role in maintaining collagen conformation and matrix stability [49]. Hydration related changes in Raman mineral to matrix ratios have been reported in bone specimens fixed with ethanol and glycerol [38]. Dehydration is known to increase collagen stiffness, decrease spacing between collagen fibrils leading to a decrease in bone toughness and an increase in hardness [50, 51]. Polar solvents have also been shown to affect the physical and mechanical properties of collagen and bone [52].

The nature of the interface between collagen and mineral at the nano-scale is still under discussion. Water bound to the mineral surface, non-collagenous glutamate containing protein and sacrificial ionic bonds have been hypothesized to mediate the interaction between mineral and matrix [4, 53, 54]. X-ray diffraction studies of bone deformation at the nano-scale demonstrated the influence of the hydration state of collagen on the amount of strain distributed to the mineral crystallites [55]. In dry bone specimens, a stiffer collagen matrix increased the strain fraction carried by the mineral phase compared

to that in hydrated bone. Hence, irrespective of the actual mechanism of interaction between collagen and mineral, the hydration state of collagen seems to influence this interaction.

In chapter 4, we explore the influence of water on bone mineral and collagen by artificially manipulating the hydration state through H/D exchange. Raman spectroscopy is well suited to study disorder of collagen secondary structure caused by substitution of deuterium oxide (D_2O) for a fraction of the labile collagen water. We report the effects of H/D exchange on collagen and mineral Raman bands. We found that the mineral lattice was slightly distorted by changes in collagen conformation on H/D exchange.

1.7 Effects of tensile loading on bone mineral

Nano-scale deformation in bone has been investigated using X-ray scattering leading to the quantification of mineral strains and collagen fibril strains [55, 56]. Mineral lattice strain is measured as the deformation of the interplanar spacing in crystals as calculated from the widths of the X-ray diffraction (XRD) peaks before and after loading [56]. Changes in mineral structure have also been observed using Raman spectroscopy as a consequence of mechanical loading and high pressure deformation [57-61]. XRD and Raman methods probe disorder on different size scales. Raman probes disorder within the unit cell, i.e. at the lowest hierarchical level of ordering, whereas XRD probes at a higher scale of ordering within a crystallite [14]. Given the nano-crystalline size of bone mineral, distortion in the internal structure is expected to show up as increased peak widths in both Raman spectra and XRD patterns.

It is known that the principal orientation of bone minerals is along the long axis of bone. Therefore, the stiffness of bone is determined by the orientation of mineral crystallites with respect to the loading direction. XRD studies have provided useful information on orientation dependent deformation of crystallites under load [62]. Differently oriented crystallites were observed to experience varying deformations along the loading direction. In chapter 5, we explore the application of polarized Raman spectroscopy to study anisotropic deformation of mineral crystallites on tensile loading. We observed that the phosphate peak width was strongly dependent on the optical polarization direction and the applied load. This result confirmed that polarized Raman spectroscopy can be used to map direction-dependent strains in bone and will be complementary to XRD in probing nano-scale deformation mechanisms in normal and diseased bone.

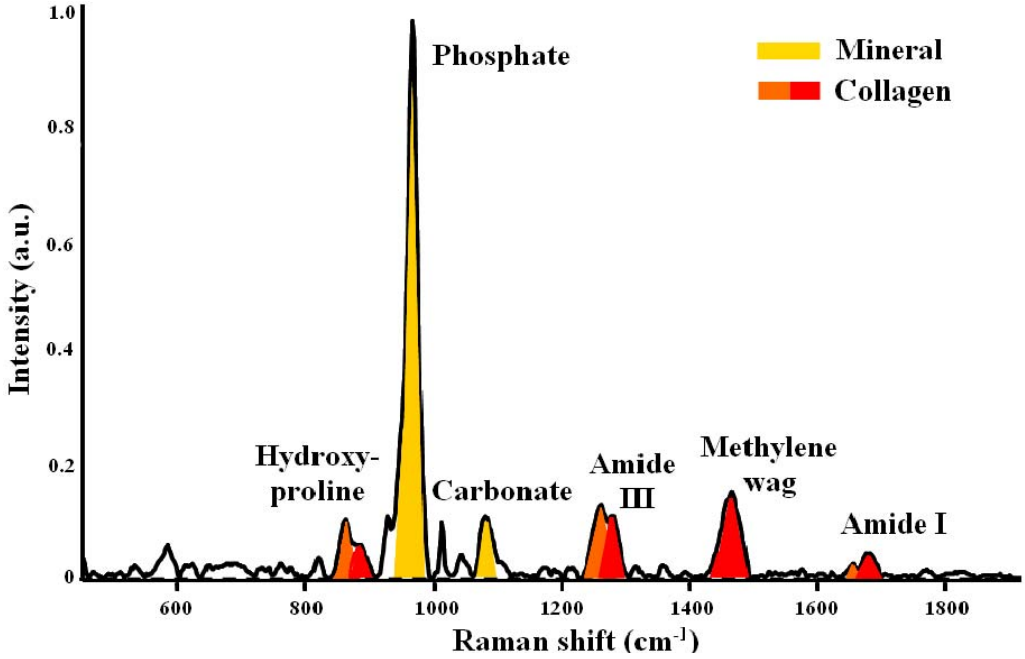

Figure 1.1 Typical Raman spectrum of cortical murine bone

References

[1] S. Weiner, H. D. Wagner, The material bone: structure-mechanical function relations, Annual Reviews of Material Science 28 (1998) 271-298.

[2] L. Knott, A. J. Bailey, Collagen cross-links in mineralizing tissues: A review of their chemistry, function, and clinical relevance, Bone 22 (1998) 181-187.

[3] M. J. Glimcher, Bone: nature of the calcium phosphate crystals and cellular, structural, and physical chemical mechanisms in their formation, Reviews in Mineralogy and Geochemistry 64 (2006) 223-282.

[4] E. E. Wilson, A. Awonusi, M. D. Morris, D. H. Kohn, M. M. J. Tecklenburg, L. W. Beck, Three structural roles for water in bone observed by solid-state NMR, Biophysical Journal 90 (2006) 3722-3731.

[5] S. Weiner, W. Traub, Bone structure: from angstroms to microns, The FASEB Journal 6 (1992) 879-885.

[6] M. Bouxsein, Bone quality: where do we go from here?, Osteoporosis International 14 (2003) S118-S127.

[7] S. C. E. Schuit, M. van der Klift, A. E. A. M. Weel, C. E. D. H. de Laet, H. Burger, E. Seeman, A. Hofman, A. G. Uitterlinden, J. P. T. M. van Leeuwen, H. A. P. Pols, Fracture incidence and association with bone mineral density in elderly men and women: the Rotterdam Study, Bone 34 (2004) 195-202.

[8] S. Sarkar, B. H. Mitlak, M. Wong, J. L. Stock, D. M. Black, K. D. Harper, Relationships between bone mineral density and incident vertebral fracture risk with Raloxifene therapy, Journal of Bone and Mineral Research 17 (2002) 1-10.

[9] C. V. Raman, A new type of secondary radiation, Nature 121 (1928) 501.

[10] A. Carden, M. D. Morris, Application of vibrational spectroscopy to the study of mineralized tissues (review), Journal of Biomedical Optics 5 (2000) 259-268.

[11] M. D. Morris, W. F. Finney, Recent developments in Raman and infrared spectroscopy and imaging of bone tissue, Spectroscopy 18 (2004) 155-159.

[12] G. Penel, G. Leroy, C. Rey, E. Bres, Micro-Raman spectral study of the PO 4 and CO 3 vibrational modes in synthetic and biological apatites, Calcified Tissue International 63 (1998) 475-481.

[13] A. Awonusi, M. D. Morris, M. M. J. Tecklenburg, Carbonate assignment and calibration in the Raman spectrum of apatite, Calcified Tissue International 81 (2007) 46-52.

[14] B. Wopenka, J. D. Pasteris, A mineralogical perspective on the apatite in bone, Materials Science and Engineering: C 25 (2005) 131-143.

[15] N. J. Crane, V. Popescu, M. D. Morris, P. Steenhuis, J. M. A. Ignelzi, Raman spectroscopic evidence for octacalcium phosphate and other transient mineral species deposited during intramembranous mineralization, Bone 39 (2006) 434-442.

[16] J.-D. P. McElderry, G. Zhao, Q. Yang, G. Mandair, R. T. Franceschi, M. D. Morris. Raman spectroscopic evidence of crystalline phosphate precursor to bone apatitic mineral. In: Proceedings of SPIE: Photonic Therapeutics and Diagnostics VI. 1 ed. San Francisco, California, USA; 2010. p. 754849-754847.

[17] J. J. Freeman, B. Wopenka, M. J. Silva, J. D. Pasteris, Raman spectroscopic detection of changes in bioapatite in mouse femora as a function of age and in vitro fluoride treatment, Calcified Tissue International 68 (2001) 156-162.

[18] J. W. Ager III, R. K. Nalla, K. L. Breeden, R. O. Ritchie, Deep-ultraviolet Raman spectroscopy study of the effect of aging on human cortical bone, Journal of Biomedical Optics 10 (2005) 034012-034018.

[19] O. Akkus, F. Adar, M. B. Schaffler, Age-related changes in physicochemical properties of mineral crystals are related to impaired mechanical function of cortical bone, Bone 34 (2004) 443-453.

[20] K. M. Kozloff, A. Carden, C. Bergwitz, A. Forlino, T. E. Uveges, M. D. Morris, J. C. Marini, S. A. Goldstein, Brittle IV mouse model for Osteogenesis Imperfecta IV demonstrates postpubertal adaptations to improve whole bone strength, Journal of Bone and Mineral Research 19 (2004) 614-622.

[21] E. R. C. Draper, M. D. Morris, N. P. Camacho, P. Matousek, M. Towrie, A. W. Parker, A. E. Goodship, Novel assessment of bone using time-resolved transcutaneous Raman spectroscopy, Journal of Bone and Mineral Research 20 (2005) 1968-1972.

[22] B. R. McCreadie, M. D. Morris, T.-c. Chen, D. Sudhaker Rao, W. F. Finney, E. Widjaja, S. A. Goldstein, Bone tissue compositional differences in women with and without osteoporotic fracture, Bone 39 (2006) 1190-1195.

[23] J. Shen, L. Fan, J. Yang, A. Shen, J. Hu, A longitudinal Raman microspectroscopic study of osteoporosis induced by spinal cord injury, Osteoporosis International 21 (2010) 81-87.

[24] H. D. Wagner, S. Weiner, On the relationship between the microstructure of bone and its mechanical stiffness, Journal of Biomechanics 25 (1992) 1311-1320.

[25] P. Fratzl, Biomimetic materials research: what can we really learn from nature's structural materials?, Journal of the Royal Society Interface 4 (2007) 637-642.

[26] H. J. Gao, B. H. Ji, I. L. Jager, E. Arzt, P. Fratzl, Materials become insensitive to flaws at nanoscale: Lessons from nature, Proceedings of the National Academy of Sciences of the United States of America 100 (2003) 5597-5600.

[27] M. Kazanci, P. Roschger, E. P. Paschalis, K. Klaushofer, P. Fratzl, Bone osteonal tissues by Raman spectral mapping: Orientation-composition, Journal of Structural Biology 156 (2006) 489-496.

[28] M. Kazanci, H. D. Wagner, N. I. Manjubala, H. S. Gupta, E. Paschalis, P. Roschger, P. Fratzl, Raman imaging of two orthogonal planes within cortical bone, Bone 41 (2007) 456-461.

[29] G. Falgayrac, S. Facq, G. Leroy, B. Cortet, G. Penel, New method for raman investigation of the orientation of collagen fibrils and crystallites in the haversian system of bone, Applied Spectroscopy 64 (2010) 775-780.

[30] D. I. Bower, Investigation of molecular orientation distributions by polarized raman scattering and polarized fluorescence, Journal of Polymer Science: Polymer Physics Edition 10 (1972) 2135-2153.

[31] S. Rinnerthaler, P. Roschger, H. F. Jakob, A. Nader, K. Klaushofer, P. Fratzl, Scanning small angle X-ray scattering analysis of human bone sections, Calcified Tissue International 64 (1999) 422-429.

[32] Z. Cole, E. Dennison, C. Cooper, Osteoporosis epidemiology update, Current Rheumatology Reports 10 (2008) 92-96.

[33] G. Lewis, J. S. Nyman, The use of nanoindentation for characterizing the properties of mineralized hard tissues: State-of-the art review, Journal of Biomedical Materials Research Part B: Applied Biomaterials 87B (2008) 286-301.

[34] B. Busa, L. Miller, C. Rubin, Y. X. Qin, S. Judex, Rapid establishment of chemical and mechanical properties during lamellar bone formation, Calcified Tissue International 77 (2005) 386-394.

[35] L. M. Miller, W. Little, A. Schirmer, F. Sheik, B. Busa, S. Judex, Accretion of bone quantity and quality in the developing mouse skeleton, Journal of Bone and Mineral Research 22 (2007) 1037-1045.

[36] E. Donnelly, A. L. Boskey, S. P. Baker, M. C. H. Van Der Meulen, Effects of tissue age on bone tissue material composition and nanomechanical properties in the rat cortex, Journal of Biomedical Materials Research - Part A 92 (2010) 1048-1056.

[37] J. Burket, S. Gourion-Arsiquaud, L. M. Havill, S. P. Baker, A. L. Boskey, M. C. H. van der Meulen, Microstructure and nanomechanical properties in osteons relate to tissue and animal age, Journal of Biomechanics In Press, Corrected Proof.

[38] Y. Yeni, J. Yerramshetty, O. Akkus, C. Pechey, C. Les, Effect of fixation and embedding on Raman spectroscopic analysis of bone tissue, Calcified Tissue International 78 (2006) 363-371.

[39] M. L. Oyen, Poroelastic nanoindentation responses of hydrated bone, Journal of Materials Research 23 (2008) 1307-1314.

[40] A. J. Bushby, V. L. Ferguson, A. Boyde, Nanoindentation of bone: Comparison of specimens tested in liquid and embedded in polymethylmethacrylate, Journal of Materials Research 19 (2004) 249-259.

[41] S. Hengsberger, A. Kulik, P. Zysset, Nanoindentation discriminates the elastic properties of individual human bone lamellae under dry and physiological conditions, Bone 30 (2002) 178-184.

[42] B. Ji, H. Gao, Mechanical properties of nanostructure of biological materials, Journal of the Mechanics and Physics of Solids 52 (2004) 1963-1990.

[43] M. Mramor, G. Leban, J. Demsar, B. Zupan, Visualization-based cancer microarray data classification analysis, Bioinformatics 23 (2007) 2147-2154.

[44] R. K. Nalla, M. Balooch, J. W. Ager III, J. J. Kruzic, J. H. Kinney, R. O. Ritchie, Effects of polar solvents on the fracture resistance of dentin: role of water hydration, Acta Biomaterialia 1 (2005) 31-43.

[45] J. Yamashita, X. Li, B. R. Furman, H. R. Rawls, X. Wang, C. M. Agrawal, Collagen and bone viscoelasticity: A dynamic mechanical analysis, Journal of Biomedical Materials Research 63 (2002) 31-36.

[46] J. S. Nyman, A. Roy, X. Shen, R. L. Acuna, J. H. Tyler, X. Wang, The influence of water removal on the strength and toughness of cortical bone, Journal of Biomechanics 39 (2006) 931-938.

[47] J. S. Nyman, Q. Ni, D. P. Nicolella, X. Wang, Measurements of mobile and bound water by nuclear magnetic resonance correlate with mechanical properties of bone, Bone 42 (2008) 193-199.

[48] A. E. Tami, M. B. Schaffler, M. L. K. Tate, Probing the tissue to subcellular level structure underlying bone's molecular sieving function, Biorheology 40 (2003) 577-590.

[49] J. Bella, B. Brodsky, H. M. Berman, Hydration structure of a collagen peptide, Structure 3 (1995) 893-906.

[50] S. Lees, L. C. Bonar, H. A. Mook, A study of dense mineralized tissue by neutron diffraction, International Journal of Biological Macromolecules 6 (1984) 321-326.

[51] W. B. Lievers, A. S. Poljsak, S. D. Waldman, A. K. Pilkey, Effects of dehydration-induced structural and material changes on the apparent modulus of cancellous bone, Medical Engineering & Physics 32 (2010) 921-925.

[52] A. K. Bembey, M. L. Oyen, A. J. Bushby, A. Boyde, Viscoelastic properties of bone as a function of hydration state determined by nanoindentation, Philosophical Magazine 86 (2006) 5691.

[53] G. E. Fantner, T. Hassenkam, J. H. Kindt, J. C. Weaver, H. Birkedal, L. Pechenik, J. A. Cutroni, G. A. G. Cidade, G. D. Stucky, D. E. Morse, P. K. Hansma, Sacrificial bonds and hidden length dissipate energy as mineralized fibrils separate during bone fracture, Nature Materials 4 (2005) 612-616.

[54] C. Jaeger, N. S. Groom, E. A. Bowe, A. Horner, M. E. Davies, R. C. Murray, M. J. Duer, Investigation of the nature of the protein - mineral interface in bone by solid-state NMR, Chemistry of Materials 17 (2005) 3059-3061.

[55] H. S. Gupta, J. Seto, W. Wagermaier, P. Zaslansky, P. Boesecke, P. Fratzl, Cooperative deformation of mineral and collagen in bone at the nanoscale, Proceedings of the National Academy of Sciences of the United States of America 103 (2006) 17741-17746.

[56] J. D. Almer, S. R. Stock, Internal strains and stresses measured in cortical bone via high-energy X-ray diffraction, Journal of Structural Biology 152 (2005) 14-27.

[57] A. Carden, R. M. Rajachar, M. D. Morris, D. H. Kohn, Ultrastructural changes accompanying the mechanical deformation of bone tissue: a Raman imaging study, Calcified tissue international 72 (2003) 166-175.

[58] M. D. Morris, W. F. Finney, R. M. Rajachar, D. H. Kohn, Bone tissue ultrastructural response to elastic deformation probed by Raman spectroscopy, Faraday Discussions 126 (2004) 159-168.

[59] O. de Carmejane, M. D. Morris, M. K. Davis, L. Stixrude, M. Tecklenburg, R. M. Rajachar, D. H. Kohan, Bone chemical structure response to mechanical stress studied by high pressure Raman spectroscopy, Calcified Tissue International 76 (2005) 207-213.

[60] K. A. Dooley, J. McCormack, D. P. Fyhrie, M. D. Morris, Stress mapping of undamaged, strained, and failed regions of bone using Raman spectroscopy, Journal of Biomedical Optics 14 (2009) 044018-044018.

[61] G. Pezzotti, Raman piezo-spectroscopic analysis of natural and synthetic biomaterials, Analytical and Bioanalytical Chemistry 381 (2005) 577-590.

[62] B. Giri, S. Tadano, K. Fujisaki, N. Sasaki, Deformation of mineral crystals in cortical bone depending on structural anisotropy, Bone 44 (2009) 1111-1120.

CHAPTER 2

Quantitative polarized Raman spectroscopy in highly turbid bone tissue

2.1 Introduction

Polarized Raman spectroscopy has long been used to study orientation in crystalline solids [1] and in both natural and synthetic fibers [2], because it is possible to determine the most probable distributions of molecular orientations. Because diseases are frequently marked by changes in molecular organization of tissues, it is useful to have methodologies that can quantitatively report on molecular orientation. Bone is a composite tissue consisting of apatite mineral crystallites embedded within a predominantly collagen matrix. We focus on bone because maintenance of bone tissue organization at all hierarchical levels is important to its mechanical functioning. In long bones, the collagen fibers are preferentially aligned parallel to the long axis of the bone. The crystallographic c-axes of the crystals align along the long axis of the collagen fibrils [3, 4]. Many disorders of bone are characterized, qualitatively, by changes in collagen and/or mineral organization [5, 6]. It is therefore imperative to quantitatively assess how this ordering is influenced by genetic defects, metabolic disorders and other factors that affect bone quality.

Techniques such as X-ray diffraction [7, 8], and scanning small-angle X-ray scattering (SAXS) [9, 10] have been used to measure quantitative orientation distributions for collagen and mineral crystallites in bone and other mineralized tissues. X-ray diffraction is limited to the crystalline regions within the tissue and involves harsh preparation techniques such as deproteination [11]. Hence, such orientation distributions have never been simultaneously obtained for collagen and mineral crystallites and never on fresh bone specimens.

Previous polarized Raman spectroscopy studies of dental enamel [12, 13] and model apatite compounds [14] have only been qualitative. Qualitative polarized Raman spectroscopic imaging has been used to study mineral and matrix orientation in cortical bone tissue by examination of the polarization components of phosphate ν_1 (P-O symmetric stretch) and amide I (carbonyl stretch) [15, 16]. Because the crystallites are oriented with their c-axes along the length of collagen fibrils, phosphate ν_1 scattering is more intense along this axis. Similarly, because collagen carbonyl groups are oriented perpendicular to the collagen chain, amide I scattering is more intense in the direction perpendicular to the collagen fibril orientation.

The polarized Raman data on bone confirm what was shown by polarized Fourier transform infrared spectroscopic (FTIR) studies [17]. It is widely understood that FTIR and Raman spectroscopies provide similar information. Spectral correspondences have recently been validated [18]. Raman spectroscopy provides experimental advantages that include minimal specimen preparation and applicability to specimens of irregular shape

or even intact bones. The problem of interference from fluorescence can be minimized by using excitation in the 650-800 nm range and by appropriate spectral processing methods, such as background subtraction. Polarized Raman spectroscopy yields both the second and fourth coefficients of the orientation distribution function, whereas IR spectroscopy yields only the second coefficient [2]. Both coefficients are needed to calculate the most probable orientation distribution function.

Bone tissue poses special challenges to the use of polarized Raman spectroscopy for measurement of quantitative orientation distribution functions because the tissue is turbid and birefringent. Standard theory assumes that the medium is completely transparent. However, multiple scattering in turbid media depolarizes light and introduces errors in the polarized Raman measurements [19]. It is difficult or impossible to correct orientation functions for multiple scattering, so measurements must be made under conditions in which multiple scattering is negligible. Similarly, the simplest polarized Raman theory assumes that refractive index is the same in all Cartesian directions. Thus, a birefringence correction may be needed to describe bone tissue [20].

In this context, the conditions under which polarized Raman spectroscopy can be used to quantitatively measure mineral and matrix orientation in bone were examined. Objectives of increasingly higher numerical aperture (NA) were used to find the values at which polarized Raman measurements are independent of NA. The use of polarized Raman spectroscopy was tested and validated using genetically modified osteogenesis imperfecta (*oim/oim*) murine bones for which mineral crystallite orientation distribution functions

have been measured by small angle X-ray scattering [9]. Finally, polarized Raman spectroscopy was used to compare mineral and matrix orientation distributions in cortical bone tissue from *oim/oim* mice and wild type mice.

2.2 Specimen preparation

Both tibiae from four five-week old wild type and four *oim/oim* female mice were used. The mice were part of a larger Institutional Animal Care and Use Committee approved study at the Hospital for Special Surgery, NY. specimens were harvested and immersed in phosphate buffered saline (PBS) and frozen at -20˚C until use. The specimens were thawed to room temperature before collection of spectra. They were kept moist throughout the experiment by a drip of phosphate buffered saline. Bone powders used to acquire isotropic Raman spectra were prepared from the mid-diaphyses of the wild type specimens using a cryogenic impact grinder (Spex 6750 Freezer Mill, Spec CertiPrep, Metuchen, New Jersey). The age, bone and background strain of the *oim/oim* specimens used in this study match that of the specimens (tibiae from five week-old *oim/oim* mouse) used in the small angle X-ray scattering study [9].

2.3 Light scattering measurements

To quantify the changes in elastic light scattering in wild type vs. *oim/oim* bone specimens, an integrating sphere (RT-060-SF, Labsphere, North Sutton, New Hampshire) setup was used to extract the scattering coefficient of the wild type and *oim/oim* tibiae [21]. A lamp attached to a Kohler Illuminator (KI-120, Labsphere, North Sutton, New Hampshire) and powered by an LPS preset power supply (LPS-150-0660, Labsphere,

North Sutton, New Hampshire) was used to deliver a uniform beam of light to the mid-diaphysis of the bone specimens, with the beam diameter (1μm) controlled by a 1:2 telescope and an adjustable iris. The specimens were placed between the telescope and the sphere, such that diffusely transmitted light was sent into the sphere and ultimately detected by a spectrograph (HR 2000+, Ocean Optics, Dunedin, Florida, 200-1100 nm). All measured transmittance spectra were corrected for both dark current and the lamp spectrum. Since the wavelength regime of interest was in the near infrared (800 - 896 nm), it was assumed that tissue absorption would have a negligible effect on the transmittance of the samples. The reduced scattering coefficient μ_s' was calculated by setting the corrected measured transmittance of the samples equal to a Beer-Lambert factor of the form $exp(-\mu_s' d)$, where d is the thickness of the tissue (set equal to the cross-sectional diameter of the bone specimens: 1.37 ± 0.06 mm for wild type and 1.25 ± 0.08 mm for *oim/oim* specimens). For linearly polarized light depolarization length calculations, the anisotropy was taken to be 0.9 [22].

2.4 Polarized Raman spectroscopy

The locally-constructed Raman microprobe has been described previously [23]. The system was constructed around a Nikon E600 microscope frame (Nikon USA, Melville, New York). The exciting laser was a 400 mW, 785 nm diode laser (Invictus, Kaiser Optical Systems Inc., Ann Arbor, Michigan) from which the circularizing optics had been removed to allow line-focusing. An axial transmissive imaging spectrograph (HoloSpec, Kaiser Optical Systems Inc., Ann Arbor, Michigan) with 25 μm entrance slit (approximately 3 cm^{-1} to 4 cm^{-1} resolution) and a 1024x256 pixel deep depletion charge-

coupled device detector (Andor Technology, Model DU 401-BR-DD, South Windsor, Connecticut) were used to disperse and record the spectrum. The polarization direction of the beam was selected using a half-wave plate. The collected Raman scatter was passed through an analyzing polarizer and directed onto the slit of the spectrograph. A wedge depolarizer after the analyzer eliminated intensity artifacts caused by the polarization dependence of the grating transmission efficiency.

Polarized Raman spectra were collected from at least 3 mid-diaphyseal locations along the length of the bone in each of the eight wild type and *oim/oim* tibial bone specimens and from powdered bones. For comparisons of wild type to *oim/oim*, each mouse is treated as an independent measure. In all experiments the polarization of the incident laser beam was maintained either parallel (x) or perpendicular (y) to the long axis of the bones. The analyzer was adjusted to pass either the component of Raman scatter polarized parallel or perpendicular to the polarization direction of the incident laser. The intensities (I) of the four possible polarization components of the Raman scatter are described by their excitation and detection polarizations along the conventional directions: I_{xx}, I_{xy}, I_{yy} and I_{yx} respectively.

2.5 Effect of elastic scattering on polarized Raman measurements

To assess the effect of light scattering on the molecular orientation measurements, the depth of field was varied using a series of objectives with differing numerical apertures (*NA*). These were 4X (0.20 *NA*), 20X (0.50 *NA*), 20X (0.75 *NA*) and 40X (0.90 *NA*). The

depth of field, z_{min}, was taken to be equal to the diffraction-limited axial resolution of an objective [24] and is given by,

$$z_{\min} = 2\lambda n / (NA)^2$$

where n is the refractive index of bone tissue, NA is the numerical aperture of the objective and λ is the laser wavelength (785 nm). Polarized Raman spectra (I_{xx} and I_{yy}) from the wild type specimens measured using the different objectives were compared to define the numerical aperture needed for artifact-free polarization measurements independent of NA.

2.6 Data analysis

The wavenumber scale of the spectrograph was calibrated against the emission lines of a neon lamp discharge. Intensities were corrected for polarization dependence of the optics by calibration against cyclohexane [25]. The spectra were corrected for spectrograph image curvature. Dark current subtraction and white light correction (flat-fielding) were performed using locally written scripts on MATLAB (Mathworks Inc., Natick, Massachusetts). Spectra were analyzed using GRAMS/AI 7.01 (Thermo Galactic, Waltham, Massachusetts).

For the wild type and *oim/oim* specimens, peak fitting was performed using GRAMS/AI 7.01 (ThermoGalactic, Waltham, Massachusetts) and the intensities of the characteristic mineral band (phosphate ν_1 at 959 cm^{-1}), and the collagen band (amide I at 1665 cm^{-1}) were measured. Band intensities were used because they can be measured with less error from spectral background subtraction than areas. The Raman intensity ratios ($R_x = I_{xy} / I_{xx}$

and $R_y = I_{yx} / I_{yy}$) for the mineral and amide I bands were corrected for the influence of sample birefringence (reflectivity, internal field, divergence) by assuming the typical collagen and mineral birefringence values of $3x10^{-3}$ and $7x10^{-3}$ respectively [18, 26]. Statistical tests were performed on band intensities and intensity ratios using two-tailed unpaired t-tests to compare the effect of NA and to compare wild type with *oim/oim* specimens. A value of $p < 0.05$ was considered significant.

Polarized Raman spectroscopy provides both the second- and fourth- order parameters, $\langle P_2 \rangle$ and $\langle P_4 \rangle$, which are the first two coefficients of the expansion in Legendre polynomials of the orientation distribution function [27, 28]. The refractive index of the bone specimens was set as 1.55 [29, 30]. Assuming a uniaxial cylindrical symmetry, the orientational order parameters, henceforth referred to as P_2 and P_4, were calculated for both phosphate ν_1 and amide I components of the wild type and *oim/oim* groups from their respective intensity ratios, R_x and R_y, and the parameter *a*. The parameter *a* of the Raman tensor for both phosphate ν_1 and amide I was determined from their isotropic depolarization ratio, R_{iso}, using the bone powder. From P_2 and P_4, the most probable orientation distribution functions, $N(\theta)$, of the phosphate ν_1 and amide I groups for the wild type and *oim/oim* groups were estimated. A detailed description of the procedure used to derive the orientational order parameters and the most probable orientation distribution function can be found in the paper by Rousseau et al. [27] and is reproduced in Appendix A1.

As a uniaxial cylindrical symmetry is assumed, y and z directions are not distinguished in an x-y-z plane. Hence, the probability that these groups are oriented at an angle θ with respect to the axis of reference was calculated by multiplying N(θ) by sin(θ).The maximum position of this N(θ)*sin(θ) distribution corresponds to the direction of preferred orientation with respect to the axis defined and the mean of the distribution calculated as the first moment characterizes the average orientation angle [9]. The average orientation angle for the phosphate group obtained by Raman spectroscopy was compared to the typical tilt angle (i.e. distribution of orientation angles) of mineral crystals obtained using small-angle X-ray scattering [9, 10]. The MATLAB scripts used for calculating the orientation distribution function are given in appendices A2 - A4.

2.7 Results

Representative peak fitted spectra of the mineral and collagen amide I bands are shown in figure 2.1. The reduced scattering coefficient, μ_s', of the wild type and *oim/oim* specimens was obtained from integrating sphere measurements of diffuse transmittance in the 800 – 896 nm wavelength range. The mean μ_s' for the wild type and *oim/oim* specimens using a flat slab model were calculated to be 14.7 ± 0.5 cm^{-1} and 12.3 ± 0.8 cm^{-1}, respectively ($p < 0.05$). The lower scattering coefficient in *oim/oim* bones is consistent with observations that molecular spacing in collagen fibrils from *oim/oim* mice is larger than normal [31].

Polarized mineral spectra (I_{xx} and I_{yy}) from the wild type specimens as functions of depth of field were measured using different objectives (figure 2.2). For the largest depth of

field (0.2 NA), complete depolarization occurs and no polarization effects are observed, i.e., I_{xx} and I_{yy} are identical. As the depth of field decreases (NA increases to 0.90), the polarization effects in the phosphate ν_1 band become more prominent, i.e., I_{xx} is stronger.

Table 2.1 compares the intensity ratios and P_2 value of the phosphate ν_1 component of the wild type specimens as a function of depth of field. The P_2 order parameter qualitatively defines the molecular orientation, with a value of -0.5 defining perfect perpendicular orientation and a value of +1 corresponding to perfect parallel orientation. A P_2 value of 0 indicates random orientation with respect to the reference axis. With decreasing depth of field, depolarization decreases resulting in higher P_2 values. The 0.90 NA objective (i.e. smallest depth of field) gives P_2 values indicating parallel or near parallel orientation of mineral crystallites and therefore, was found suitable for further quantitative polarized Raman measurements. Lower NA objectives (0.75 NA or 0.80 NA) could be employed for qualitative measures, but are not suitable for quantitative estimations of molecular orientation. Higher NA objectives (water or oil-immersion) might indeed give slightly higher P_2 values, but calibration and correction for partial depolarization by the high gathering angle would be challenging and laborious.

Table 2.2 compares the order parameters, P_2 and P_4, of the 959 cm^{-1} phosphate ν_1 band and the 1665 cm^{-1} amide I band for the wild type and *oim/oim* specimens obtained using a 0.90 NA objective. The order parameters were calculated from the intensity ratios, R_x and R_y. The parameter *a* was calculated to be -0.04 for the phosphate ν_1 band and -0.48 for the amide I 1665 cm^{-1} band using isotropic samples of murine cortical bone powder.

Correcting for the effects of birefringence has a small effect, i.e., less than 1% change in the computed values of P_2 and P_4 and can be neglected for these samples.

The $N(\theta)*\sin(\theta)$ plot for amide I is shown in figure 2.3 for the wild type and *oim/oim* groups. For the wild type group, the plot peaks at $\theta = 90^\circ \pm 19^\circ$ demonstrating that the amide I groups have a preferred orientation perpendicular to the longitudinal axis of the bone (x direction of the diaphysis in the nomenclature used here), although there is a distribution of approximately 20˚. For the *oim/oim* group, the amide I $N(\theta)*\sin(\theta)$ peaks at $\theta = 90^\circ \pm 32^\circ$. This indicates that although the preferred orientation is still perpendicular to the x direction of the diaphysis, collagen orientation is more variable in *oim/oim* mice. The influence of uncertainty in the P_4 order parameter value on the orientation distribution function should be noted here. For example, at one standard deviation below the mean, the calculated amide I distribution for the *oim/oim* group (Table 2.2) is an improbable asymmetric unimodal shape peaked at 69˚, rather than the Gaussian shape that is expected.

Calculation of the first moments for these distributions for amide I give an average orientation angle of $76^\circ \pm 2^\circ$ for the wild type group and that of $72^\circ \pm 4^\circ$ for the *oim/oim* group. For comparison purposes, we have calculated the average orientation angles for the collagen backbone considering that amide I carbonyl groups are perpendicular to the collagen backbone. The average orientation angle for collagen backbone with respect to the x direction is 14˚ (90˚- 76˚) in the wild type group. In the *oim/oim* group the average orientation angle is 18˚ (90˚- 72˚). There could be a tendency for a larger average

orientation in *oim/oim,* although the difference is not statistically significant. In case of random orientation of the collagen backbone, the average orientation angle would be 57.3˚.

The N(θ)*sin(θ) plot for phosphate ν_1 is shown in figure 2.4. The N(θ)*sin(θ) distribution peaks at $\theta = 10^{\circ} \pm 8^{\circ}$ for the wild type group and at $\theta = 11^{\circ} \pm 11^{\circ}$ for the *oim/oim* group indicating that the mineral crystallites are highly oriented along the x direction of the bone diaphysis and have a narrower distribution than collagen. Calculation of the mean of these distributions yields an average orientation angle of 22˚ ± 3˚ for the mineral crystallites in the wild type group. This is in agreement with values published in earlier X-ray scattering [32] and electron microscopic tomography studies [33] on normal mice (typically around 20˚). For the *oim/oim* group, the mean of the distribution yields an average orientation angle of 28˚ ± 3˚ for the mineral crystallites, which is significantly larger than that measured in the wild type specimens ($p<0.05$). This average orientation angle is in agreement with the distribution of orientation angles of aligned crystals (25˚ ± 3˚ with respect to the bone long axis) observed in a small-angle X-ray scattering study on cortical bone samples also from 5-week old *oim/oim* mice [9]. These changes in the mineral crystallites could be due to the increased molecular spacing and reduced packing order of osteogenesis imperfecta type collagen fibrils [31].

2.8 Discussion

The orientation distributions of mineral crystallites and collagen fibers in the cortical regions of murine wild type and *oim/oim* bone specimens have been determined for the

first time by polarized Raman spectroscopy. The orientation distribution functions for mineral and collagen in the wild type group are in agreement with mineral and collagen orientation distributions obtained using small angle X-ray scattering and X-ray pole figure analysis on bone [32, 34] and X-ray diffraction on demineralized bone [35]. Further, the average orientation angle of mineral crystallites in the *oim/oim* group from our measurements agrees with that observed in an earlier SAXS study [9]. These measurements provide validation for the use of Raman spectroscopy to assess mineral and matrix orientation simultaneously in intact normal and diseased or damaged tissues.

Using line illumination or point illumination requires trade-offs. A slit aperture has worse axial and lateral performance than a pinhole aperture, making the line illumination technique more vulnerable to artifacts rising from scattering effects [36]. However, line illumination has the advantage of power distribution, which limits thermal damage to the tissue specimen [37]. Further, line illumination allows faster data acquisition over a wider region of interest. Hence, line illumination was the method of choice for this study. The line focus enabled the simultaneous collection of 126 spectra (one for each row of pixels on the CCD detector).

Systematic errors from elastic scattering in bone tissue can be reduced by the use of a high numerical aperture objective to minimize depolarization. In tissues with higher turbidity and anisotropy factor greater than 0.9, an oil-immersion or water-immersion objective might be required to limit depth of field. However, such objectives themselves partially depolarize Raman scatter because of their high gathering angles. Corrections for

this effect are complicated. In soft tissues with a lower anisotropy factor and reduced turbidity, a lower NA objective might prove sufficient for quantitative polarized Raman measurements. Techniques such as spatially offset Raman spectroscopy and transmission Raman spectroscopy have been used to study bulk scattering materials, but it is unclear if they will be suitable for quantitative polarization analysis.

In the present study, the mathematical description of orientation effects in Raman spectra has been derived for single fibers, not for extended arrays of fibers that are found in bone. We used a microscope objective with NA = 0.90 with a nominal axial resolution of approximately 3.0 μm. Taking the thickness of a lamella to be approximately 300 nm, our microscope is integrating over almost 10 lamellae of intact bone. In the case of small angle X-ray scattering, the orientation information is averaged over a 200 μm thick section of demineralized bone [9]. That we obtain agreement with SAXS orientation measurements in our wild type and *oim/oim* groups suggests that extension of polarization theory to bone is valid. The elastic scattering problem would have to be addressed in human bone specimens, such as those that have previously been used in polarized FTIR [17]. In humans, the lamellae are about 2-9 μm thick [38] so confounding effects of multiple lamellae would be diminished, but multiple scattering would still occur.

2.9 Conclusion

This chapter reports the first simultaneous quantitative measurements of matrix collagen and mineral orientation in non-deproteinated, genetically disordered (OI) bone

specimens. Systematic errors in the orientation distribution calculations due to contributions from sample turbidity and multiple elastic scattering effects have been minimized by employing a high numerical aperture objective. Mineral crystallite orientations in OI mouse bones calculated using polarized Raman spectroscopy have been validated against small angle X-ray scattering results. The techniques described in this chapter may have widespread utility because the mechanical properties of calcified tissue are dependent on the molecular structure and the arrangement of the constituent mineral crystals within the organic matrix [39]. For example, in the SAMP6 mouse model for skeletal fragility, the reduced strength of the bone matrix is attributed to poorer organization of collagen fibers and reduced collagen content, although the animals have normal levels of collagen cross-links and normal mineral crystallite structure [40]. In biglycan-deficient mice, alterations in collagen and over-expression of non-collagenous proteins lead to an increase in mineralization, yet reduced mechanical properties [41]. The ability to probe simultaneously mineral and matrix composition and orientation makes Raman spectroscopy a valuable tool to study such problems.

Table 2.1 Intensity ratios and orientational order parameter, P_2, for phosphate ν_1 as a function of the objective depth of field (z_{min}) for wild type group.

Objective	Intensity Ratios		Order Parameter, P_2
	R_x	R_y	
4X, 0.20 NA (z_{min}=60.8 μm)	0.60 ± 0.2	0.78 ± 0.1	0.03 ± 0.02
20X, 0.50 NA (z_{min}= 9.7 μm)	0.26 ± 0.1	0.36 ± 0.11	0.06 ± 0.01
20X, 0.75 NA (z_{min}= 4.3 μm)	0.29 ± 0.05	0.59 ± 0.09	0.20 ± 0.02
40X, 0.90 NA (z_{min}= 3.0 μm)	0.06 ± 0.03	0.74 ± 0.1	0.72 ± 0.06

Table 2.2 Orientational order parameters, P_2 and P_4, for phosphate ν_1 and amide I with a 0.90 NA objective for wild type and oim/oim groups. (* $p < 0.05$)

Raman bands	Order Parameters	Wild Type Group (Mean + SD)	*oim/oim* Group (Mean + SD)
Phosphate ν_1	P_2	0.72 ± 0.06	0.60 ± 0.06*
	P_4	0.58 ± 0.08	0.48 ± 0.06
Amide I	P_2	-0.37 ± 0.09	-0.32 ± 0.05
	P_4	0.15 ± 0.05	0.06 ± 0.03*

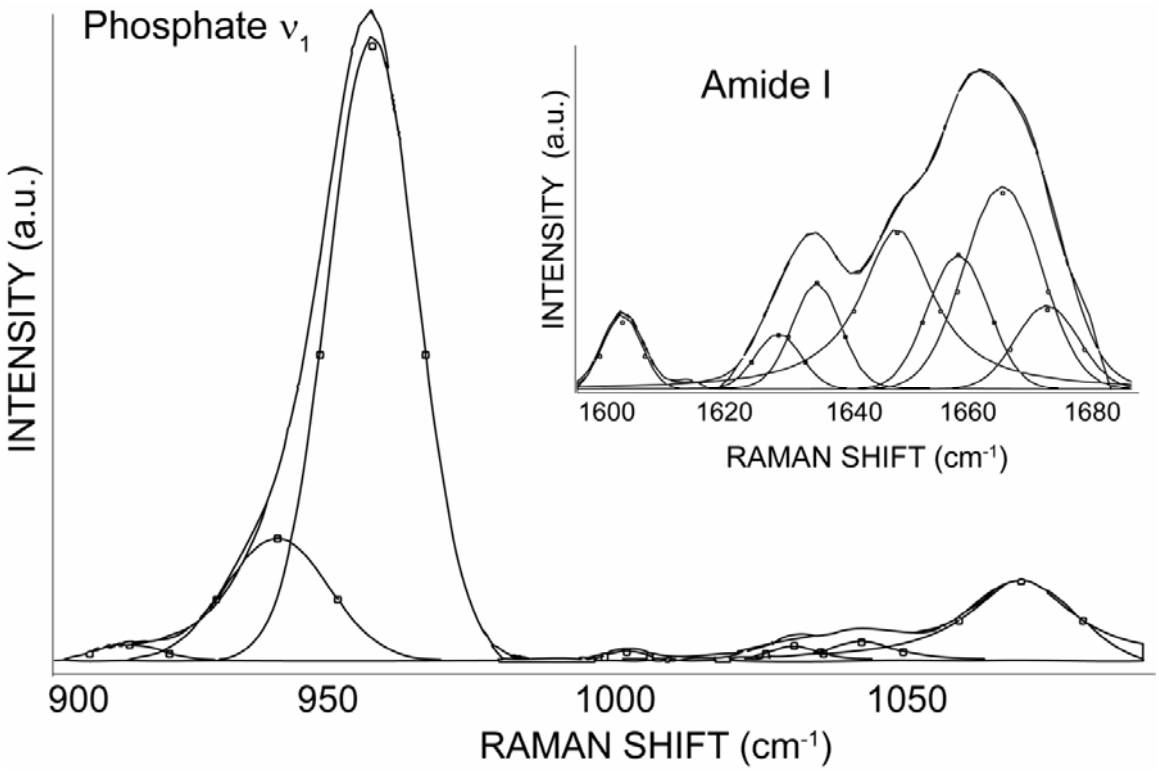

Figure 2.1 Typical curve-fit spectra illustrating the sub-bands contributing to the overall contour of the mineral (phosphate and carbonate) and amide I bands. The spectrum shown is from a wild type specimen using a 0.90 NA objective.

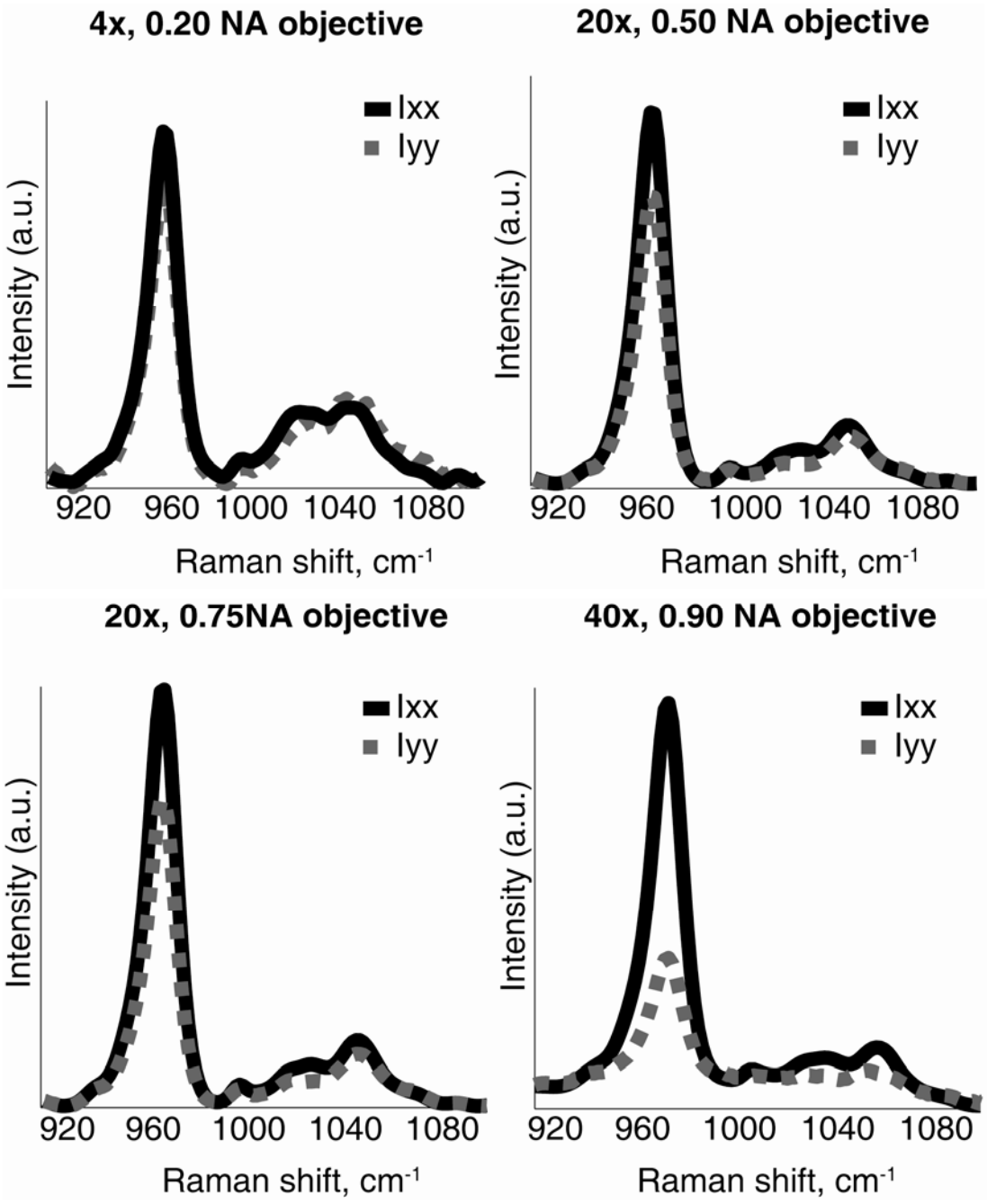

Figure 2.2 Mineral bands of the parallel-polarized bone spectra of a representative wild type specimen as a function of depth of field. The polarization effects in the phosphate band ($I_{xx} > I_{yy}$) are more prominent with the use of a high NA objective.

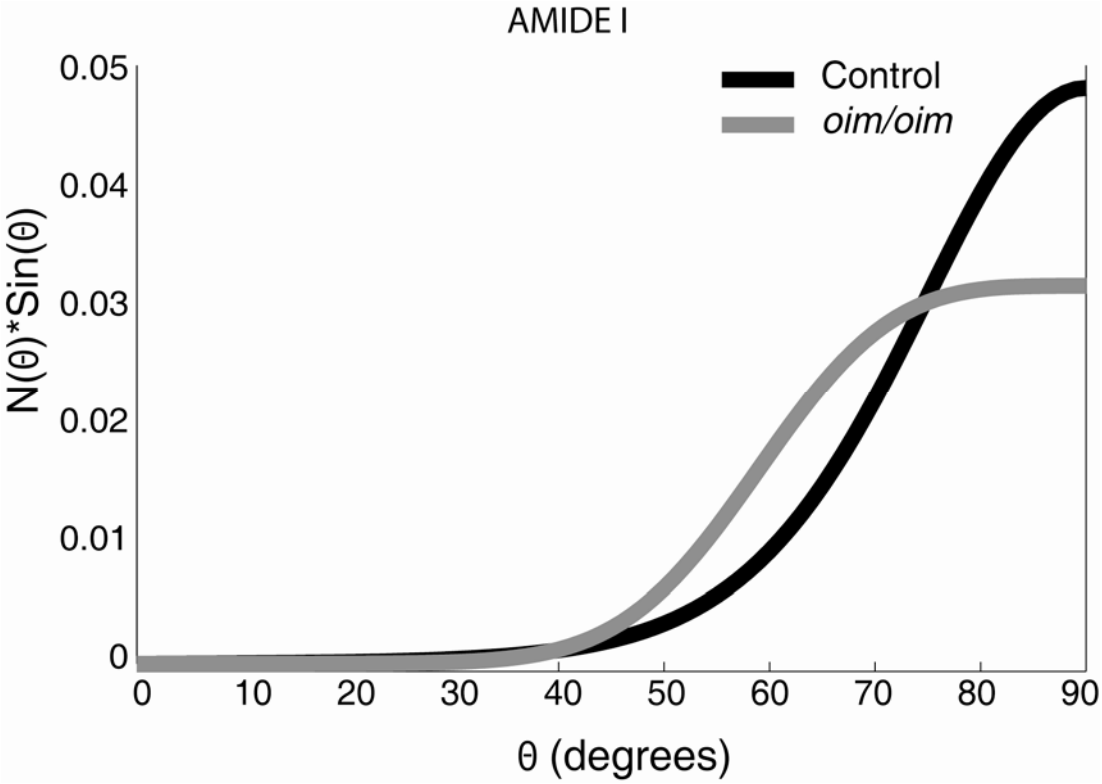

Figure 2.3 Rectangular coordinate plot of the orientation distribution function, N(θ)*sin(θ), of amide I for wild type and *oim/oim* groups. The average orientation angles are 76 ± 2˚ for the wild type group and 72 ± 4˚ for the *oim/oim* group. The average orientation of collagen backbone can be calculated by subtracting the average orientation angle of amide I group from 90˚.

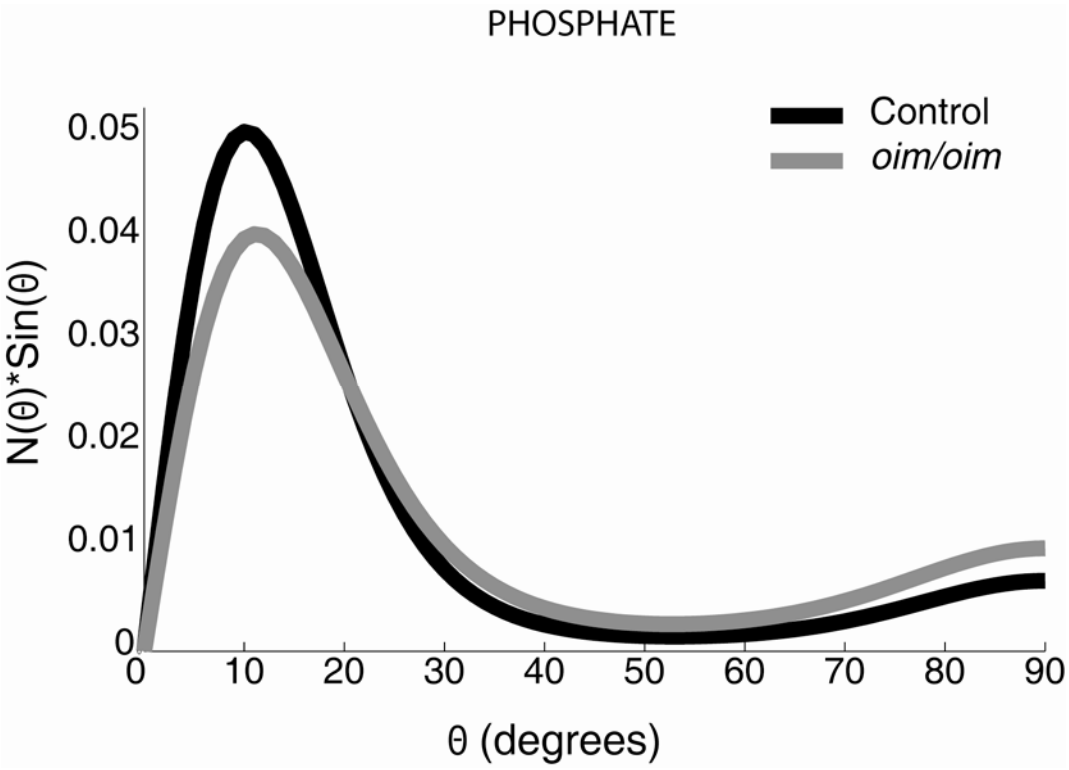

Figure 2.4 Rectangular coordinate plot of the orientation distribution function, N(θ)*sin(θ), of phosphate for wild type and *oim/oim* groups. The average orientation angles are 22 ± 3˚ for the wild type group and 28 ± 3˚ for the *oim/oim* group. Note that the carbonated apatite is preferentially aligned along the backbone axis of collagen (x direction).

References

[1] D. C. Smith, C. Carabatos-Nedelec, Raman spectroscopy applied to crystals: phenomena and principles, concepts and conventions, In: I. R. Lewis, H. G. M. Edwards, editors. Handbook of Raman Spectroscopy. New York: Marcel Dekker; 2001, pp. 349-422.

[2] S. Michielsen, Application of Raman spectroscopy to organic fibers and films, In: I. R. Lewis, H. G. M. Edwards, editors. Handbook of Raman Spectroscopy. New York: Marcel Dekker; 2001, pp. 749-798.

[3] W. Traub, T. Arad, S. Weiner, Three-dimensional ordered distribution of crystals in turkey tendon collagen fibers, Proceedings of the National Academy of Sciences of the United States of America 86 (1989) 9822-9826.

[4] S. Weiner, W. Traub, Organization of hydroxyapatite crystals within collagen fibrils, FEBS Letters 206 (1986) 262-266.

[5] R. B. Martin, D. L. Boardman, The effects of collagen fiber orientation, porosity, density, and mineralization on bovine cortical bone bending properties, Journal of Biomechanics 26 (1993) 1047-1054.

[6] R. B. Martin, J. Ishida, The relative effects of collagen fiber orientation, porosity, density, and mineralization on bone strength, Journal of Biomechanics 22 (1989) 419-426.

[7] M. C. Kirby, R. M. Aspden, D. W. L. Hukins, Determination of the orientation distribution function for collagen fibrils in a connective tissue site from a high-angle X-ray diffraction pattern, Journal of Applied Crystallography 21 (1988) 929-934.

[8] R. M. Aspden, D. W. L. Hukins, Collagen organization in articular cartilage, determined by X-ray diffraction, and its relationship to tissue function, Proceedings of the Royal Society of London. Series B, Biological Sciences 212 (1981) 299-304.

[9] P. Fratzl, O. Paris, K. Klaushofer, W. J. Landis, Bone mineralization in an osteogenesis imperfecta mouse model studied by small-angle x-ray scattering, The Journal of Clinical Investigation 97 (1996) 396-402.

[10] S. Rinnerthaler, P. Roschger, H. F. Jakob, A. Nader, K. Klaushofer, P. Fratzl, Scanning small angle X-ray scattering analysis of human bone sections, Calcified Tissue International 64 (1999) 422-429.

[11] D. Y. Yoon , C. Chang, R. S. Stein, An improved model for crystalline orientation of spherulitic polymers, Journal of Polymer Science: Polymer Physics Edition 12 (1974) 2091-2110.

[12] H. Tsuda, J. Arends, Orientational micro-Raman spectroscopy on hydroxyapatite single crystals and human enamel crystallites, Journal of Dental Research 73 (1994) 1703-1710.

[13] A. C. T. Ko, L.-P. i. Choo-Smith, M. Hewko, M. G. Sowa, C. C. S. Dong, B. Cleghorn, Detection of early dental caries using polarized Raman spectroscopy, Optics Express 14 (2006) 203-215.

[14] G. Leroy, n. Leroy, G. Penel, C. Rey, P. Lafforgue, E. Bres, Polarized micro-Raman study of fluorapatite single crystals, Applied Spectroscopy 54 (2000) 1521-1527.

[15] M. Kazanci, P. Roschger, E. P. Paschalis, K. Klaushofer, P. Fratzl, Bone osteonal tissues by Raman spectral mapping: Orientation-composition, Journal of Structural Biology 156 (2006) 489-496.

[16] M. Kazanci, H. D. Wagner, N. I. Manjubala, H. S. Gupta, E. Paschalis, P. Roschger, P. Fratzl, Raman imaging of two orthogonal planes within cortical bone, Bone 41 (2007) 456-461.

[17] N. P. Camacho, S. Rinnerthaler, E. P. Paschalis, R. Mendelsohn, A. L. Boskey, P. Fratzl, Complementary information on bone ultrastructure from scanning small angle X-ray scattering and Fourier-transform infrared microspectroscopy, Bone 25 (1999) 287-293.

[18] S. Gourion-Arsiquaud, D. Faibish, E. Myers, L. Spevak, J. Compston, A. Hodsman, E. Shane, R. R. Recker, E. R. Boskey, A. L. Boskey, Use of FTIR spectroscopic imaging to identify parameters associated with fragility fracture, Journal of Bone and Mineral Research 24 (2009) 1565-1571.

[19] X. Wang, L. V. Wang, Propagation of polarized light in birefringent turbid media: A Monte Carlo study, Journal of Biomedical Optics 7 (2002) 279-290.

[20] N. J. Everall, Measurement of orientation and crystallinity in uniaxially drawn poly(ethylene terephthalate) using polarized confocal Raman microscopy, Applied Spectroscopy 52 (1998) 1498-1504.

[21] M. Chandra, K. Vishwanath, G. D. Fichter, E. Liao, S. J. Hollister, M.-A. Mycek, Quantitative molecular sensing in biological tissues: an approach to non-invasive optical characterization, Optics Express 14 (2006) 6157-6171.

[22] V. Tuchin, Methods and algorithms for the measurement of the optical parameters of tissues, In: Tissue optics: light scattering methods and instruments for medical diagnosis Bellingham, WA: SPIE Press; 2000, pp. 143-256.

[23] N. J. Crane, M. D. Morris, J. M. A. Ignelzi, G. Yu, Raman imaging demonstrates FGF2-induced craniosynostosis in mouse calvaria, Journal of Biomedical Optics 10 (2005) 031119-031118.

[24] S. Inoue, Foundations of confocal scanned imaging in light microscopy, In: J. B. Pawley, editor. Handbook of Biological Confocal Microscopy. New York: Plenum Press; 1995, pp. 1-17.

[25] M. J. Pelletier, Effects of temperature on cyclohexane Raman bands, Applied Spectroscopy 53 (1999) 1087-1096.

[26] E. L. V. Lewis, D. I. Bower, Raman tensors for the 1614 and 633 cm−1 modes of bis(2-hydroxyethyl) terephthalate, Journal of Raman Spectroscopy 18 (1987) 61-70.

[27] M.-E. Rousseau, T. Lefavre, L. Beaulieu, T. Asakura, M. Pezolet, Study of protein conformation and orientation in silkworm and spider silk fibers using Raman microspectroscopy, Biomacromolecules 5 (2004) 2247-2257.

[28] F. Lagugne Labarthet, T. Buffeteau, C. Sourisseau, Orientation distribution functions in uniaxial systems centered perpendicularly to a constraint direction, Applied Spectroscopy 54 (2000) 699-705.

[29] A. Ascenzi, C. Fabry, Technique for dissection and measurement of refractive index of osteones, Journal of Biophysical and Biochemical Cytology 6 (1959) 139-142.

[30] N. W. Taylor, C. Sheard, Microscopic and X-ray investigations on the calcification of tissue Journal of Biological Chemistry 81 (1929) 479-493.

[31] D. J. McBride, V. Choe, J. R. Shapiro, B. Brodsky, Altered collagen structure in mouse tail tendon lacking the [alpha]2(I) chain, Journal of Molecular Biology 270 (1997) 275-284.

[32] P. Fratzl, M. Groschner, G. Vogl, H. Plenk, J. Eschberger, N. Fratzl-Zelman, K. Koller, K. Klaushofer, Mineral crystals in calcified tissues: A comparative study by SAXS, Journal of Bone and Mineral Research 7 (1992) 329-334.

[33] W. J. Landis, M. J. Song, A. Leith, L. McEwen, B. F. McEwen, Mineral and organic matrix interaction in normally calcifying tendon visualized in three dimensions by high-voltage electron microscopic tomography and graphic image reconstruction, Journal of Structural Biology 110 (1993) 39-54.

[34] N. Sasaki, Y. Sudoh, X-ray pole figure analysis of apatite crystals and collagen molecules in bone, Calcified Tissue International 60 (1997) 361-367.

[35] S. J. Wilkinson, D. W. L. Hukins, Determination of collagen fibril structure and orientation in connective tissues by X-ray diffraction, Radiation Physics and Chemistry 56 (1999) 197-204.

[36] A. A. Tanbakuchi, A. R. Rouse, A. F. Gmitro, Monte Carlo characterization of parallelized fluorescence confocal systems imaging in turbid media, Journal of Biomedical Optics 14 (2009) 044024-044016.

[37] D. Zhang, J. D. Hanna, Y. Jiang, D. Ben-Amotz, Influence of laser illumination geometry on the power distribution advantage, Applied Spectroscopy 55 (2001) 61-65.

[38] M.-G. Ascenzi, A. Ascenzi, A. Benvenuti, M. Burghammer, S. Panzavolta, A. Bigi, Structural differences between "dark" and "bright" isolated human osteonic lamellae, Journal of Structural Biology 141 (2003) 22-33.

[39] W. J. Landis, The strength of a calcified tissue depends in part on the molecular structure and organization of its constituent mineral crystals in their organic matrix, Bone 16 (1995) 533-544.

[40] M. J. Silva, M. D. Brodt, B. Wopenka, S. Thomopoulos, D. Williams, M. H. M. Wassen, M. Ko, N. Kusano, R. A. Bank, Decreased collagen organization and content are associated with reduced strength of demineralized and intact bone in the SAMP6 mouse, Journal of Bone and Mineral Research 21 (2006) 78-88.

[41] J. M. Wallace, R. M. Rajachar, X.-D. Chen, S. Shi, M. R. Allen, S. A. Bloomfield, C. M. Les, P. G. Robey, M. F. Young, D. H. Kohn, The mechanical phenotype of biglycan-deficient mice is bone- and gender-specific, Bone 39 (2006) 106-116.

CHAPTER 3

Age-based classification using Raman and nanoindentation metrics from murine cortical bone specimens

3.1 Introduction

The strength and fracture resistance of bone are primarily dependent on its mass, architecture, and material properties. Bone mass density (BMD) measured using dual-energy X-ray absorptiometry (DXA) remains the gold standard for diagnosis of osteoporosis. While BMD is correlated with fracture, it inadequately predicts increase in fracture risk and explains only a limited proportion of the anti-fracture efficacy observed with anti-resorptive therapies [1]. The heterogeneous and hierarchical nature of bone makes it unlikely for a single measurement to fully characterize its structural integrity or accurately predict fracture risk. A diagnostic marker can be a combination of quantifiable features on the level of an organ, tissue, cell, protein or gene. Hence, studies are increasingly focused on understanding the contributions of architecture, composition and remodeling dynamics to the maintenance of bone strength [2-5].

At the tissue level, contributions from collagen and mineral components to bone quality and strength are not yet fully understood. Quantification of molecular structure and material properties at the tissue level would assist in examining the composite nature of bone and its effect on whole bone strength [6]. Factors such as aging and disease alter

bone mass, architecture and tissue properties. Age-related degradation of bone mass and architecture can compromise bone integrity. While compositional changes with age may precede failure, the relationship between tissue composition and material behavior at different ages is not fully characterized [7-9]. Combining different well-established methods for characterizing the material quality of bone allows us to study how age-related material changes relate to tissue and whole bone mechanics. For instance, by co-localizing Raman microspectroscopy and nanoindentation testing, the material quality of bone tissue can be studied at defined spatial positions at the sub-micrometer scale. Raman spectroscopy provides important compositional measures of the mineral and matrix components such as amount of mineralization, crystallinity, degree of carbonate substitution in the mineral, collagen content and cross-linking. Nanoindentation testing provides information on the hardness, elastic modulus and creep behavior of the tissue.

A common assumption in studies investigating relationships between composition and mechanical properties is linearity. Univariate strategies make an assumption that variables are independent and exclude potentially informative interactions that might exist with other variables. For example, composition and nanomechanical properties have either been examined independently [10, 11] or by assuming linear relationships [12, 13]. One would expect that biological variables may be associated in a non-linear fashion and hence, more information can be gained by observing a set of metrics as a group, rather than averaging their individual effects. Probing the complex relationships between composition and mechanics at the tissue level will provide us with a better understanding

of how aging and disease affect bone function at different hierarchical levels. Eventually, this information can be useful in developing clinical predictive models of fracture risk.

Exploratory data analysis techniques such as machine learning and high-dimensional data visualization can be applied to extract useful knowledge from a heterogeneous assortment of data. Machine learning involves applying statistical modeling algorithms to a data set. These models follow a ‘top down’ approach and attempt to learn the underlying concept rather than fit a provided model. Applications to microarray analysis [14], mass spectrometry [15] and spectroscopy [16] for biomarker discovery are examples of where data mining has made contributions. Popular dimension reduction methods such as linear principal component analysis and linear discriminant analysis find linear combinations of variables that best predict a class type. However, they do not account for the inherent underlying nonlinear structure associated with most biomedical data and the new features they create are difficult to interpret.

Our previous study combined complementary techniques, Raman spectroscopy and nanoindentation testing, to investigate tissue level material properties at specific spatial locations [17]. Compositional and mechanical changes at the tissue microscale as a consequence of aging were measured. Compositional measurements were significantly correlated with mechanical properties in an age-dependent manner, highlighting the complex changes in bone material properties with age. In this study, we adopted a retrospective data mining approach to describe changes in femoral material properties between young and old mice. We applied two exploratory data analysis tools, RadViz

which a non-linear visualization method, and VizRank which is a classification and visual projection scoring algorithm. The utility of these data mining tools in identifying compositional and mechanical properties that are important in determining age-related differences is demonstrated here.

3.2 Data sets

Mechanical and compositional measurements from the right femora of 4, 5, and 19 month old male C57Bl/6 mice were used in this study. 4 month old mice are nearing skeletally maturity but still growing, 5 month old mice have fully developed skeletal integrity, and 19 month old mice have compromised structural integrity [18-20]. The 5 and 19 month age groups included both non-exercised mice and mice subjected to an exercise program (running on a treadmill, 12 m/min, 5 degree incline, 30 minutes/day) for the 21 days prior to euthanization. There were 8 femora from four month old mice (all non-exercised), 13 from five month old mice (6 non-exercised and 7 exercised), and 12 from nineteen month old mice (6 non-exercised and 6 exercised).

Femora were prepared for co-localized analysis so that Raman and nanoindentation measurements could be taken at the same location on the mid-diaphysis [21]. Specimens were first analyzed using Raman microspectroscopy and followed by nanoindentation. The depth of field from the Raman analysis and the indentation depth were matched to be about 2-3 μm. The data set contained four Raman (carbonate to phosphate ratio, mineral to matrix ratio (MMR), crystallinity and cross-linking) and seven nanoindentation (hardness, plasticity index, elastic modulus, creep displacement, creep viscosity_series,

creep viscosity_parallel and creep modulus) variables for 33 specimens. The creep variables were used without any transformation.

3.3 Multidimensional visualization

RadViz is a nonlinear radial visualization method which maps *n* data dimensions (variables) onto two dimensional space for the purpose of clustering [22]. Variables describing specimen characteristics are equally spaced around the perimeter of a circle and called dimension anchors. The values of each dimension (variable) are standardized to the interval between 0 and 1. Each specimen is shown as a point inside the unit circle with its location determined by the influence of its dimension anchors [23]. A physical metaphor would be multiple springs attaching a specimen point to its dimension anchors. The influence ('force') that any dimension exerts on a specimen point is determined by Hooke's law: $f = k*d$. The spring constant, k, is the value of the scaled dimension of that specimen (value ranges from 0 to 1) and d is the distance between the specimen point and the perimeter point on the circle assigned to that dimension. Given a set of *n* dimensions (or variables), each specimen point is placed inside the circle where the sum of its dimension spring forces equals zero. The equations used to calculate the locations of specimens points are described in Appendix A5 and have been adapted from [24].

In the representative RadViz illustration in figure 3.1, there are eight variables or dimensions associated with the one specimen point plotted. All dimensions are equally spaced around the circle in numerical order and eight imaginary springs connect these variables to the specimen point inside the circle. The spring constants or dimensional

values are higher for variables 7 and 8 (black springs) and lower for the other variables (grey springs). Hence, the specimen point is positioned closer to variables 7 and 8 than the others. If all dimensions had equal values, then the specimen point would be placed close to the center. Thus, the specimen points visualized by RadViz are described uniquely by their x-y position and could carry class labels, if any.

3.4 Variable selection and classification

The selection and ordering of variables around the circle circumference influences the RadViz visualization. For instance, with given set of *n* variables, a total of (*n*-1)!/2 unique RadViz projections are possible. To find interesting and informative projections of class-labeled data, the VizRank algorithm assesses possible RadViz projections and scores them by their ability to visually discriminate between classes [25]. The classification quality is the predictive accuracy of *k*-nearest neighbor (*k*-NN) classifier on the RadViz data set as estimated through 10-fold cross validation, with *k* is set to sqrt(N), where N is the number of specimen points. Projections are given a score between 0 and 100 with projections providing perfect class separation receiving 100 and less informative projections receiving correspondingly lower scores. In this study, we used only the single best-ranked projection for classification. For a good quality RadViz projection, only a certain number of top ranked variables need to be used, instead of all available variables in the data. These top ranked variables can be considered as the significant variables that characterize the data features.

3.5 Classifier accuracy

To compare VizRank's accuracy to that of other machine learning approaches, we trained and classified upon the same dataset using support vector machines (SVM) with a linear kernel, a k-nearest neighbor learner (kNN, where k equal to square root of number of data instances in learning set), a naive Bayesian classifier and a C4.5 decision tree. A bootstrap resampling technique was used with the sampling repeated 100 times, as this technique provides a less variable estimate than cross-validation despite its computational cost [25]. The classification performance was obtained using the 0.632 bootstrap estimator that combines both the bootstrap sampling error rate and the resubstitution error rate [26]. The area under the receiver operating curve (AUC) was also calculated as a performance measure. A classifier is considered better if it has a larger AUC compared to a different classifier.

3.6 Implementation

RadViz and VizRank methods were implemented within Orange (http://www.ailab.si/orange), an open-source data mining suite featuring Python scripting and a graphic interface [27]. The other machine learning approaches such as linear SVM, kNN, naïve Bayesian and decision tree were also implemented within Orange.

3.7 Results

3.7.1 Univariate statistics: Raman spectroscopic and nanoindentation variables from the data set are presented in table 3.1. The material properties of 4 month old specimens were not significantly different from that of 5 month old specimens. Therefore, these two age

groups were combined and considered as a single age group (young). Mineral to matrix ratio (MMR), carbonate to phosphate ratio and crystallinity were significantly greater in the old specimens compared to that of young specimens. Crosslinking ratio and nanoindentation measurements were not different between the two groups. Exercise had no significant or marginally significant effect of the means of any metric. Between 4 and 5 month old specimens, only collagen cross-linking ratio and hardness were marginally different ($p < 0.1$). Multivariate linear regressions with Raman covariates and nanoindentation dependent variables were previously reported [17].

3.7.2 Nanoindentation measures as the dependent metric: Non-linear projection and classification were performed with nanoindentation metrics as the dependent class, and Raman metrics, age (young/old) and exercise (control/exercise) groups as independent variables. All data were grouped under two age classes (4 and 5 months combined as 'young' and 19 month as 'old'). Nanoindentation variables were binned into two classes (high and low) using an equal-frequency discretization method, because the classification algorithm requires a discrete dependent class. Table 3.2 (top panel) outlines the best RadViz projections for the dataset containing both the age classes. The cutoff point for two-class equal-frequency discretization is provided for each nanoindentation metric. VizRank algorithm was restricted to combinations of up to four variables. MMR, crystallinity, carbonate/phosphate and age metrics distinguished specimens with high or low plasticity index with a classification accuracy of 80%. The other nanoindentation metrics were classified with less than 80% accuracy.

Tables 3.2 (center and bottom panels) outline the best RadViz projections for the dataset containing only young and old specimens respectively. Independent variables consisted of Raman metrics and exercise group. VizRank algorithm was restricted to combinations of up to four variables. Classification accuracy greater than 80% was observed for plasticity index, creep modulus parallel and creep viscosity parallel in the young age group and hardness in the old age group.

3.7.3 Raman measures as the dependent metric: The direction of dependencies between compositional and mechanical variables is not clear. Hence, non-linear projection and classification were also performed with Raman metrics as the dependent class, and nanoindentation metrics, age (young/old) and exercise (control/exercise) groups as independent variables. All data were grouped under two age classes (4 and 5 months combined as ‘young’ and 19 month as ‘old’). Raman variables were binned into two classes (high and low) using an equal-frequency discretization method, while nanoindentation variables were left continuous and untransformed. Table 3.3 (top panel) outlines the best RadViz projections for the dataset containing both age groups. The cutoff point for equal-frequency discretization is provided for each Raman metric. VizRank algorithm was restricted to combinations of up to four variables. MMR and crystallinity were classified with greater than 90% accuracy.

Tables 3.3 (center and bottom panels) outline the best RadViz projections for the dataset containing only young and old specimens respectively. Independent variables consisted of nanoindentation metrics and exercise group. VizRank algorithm was restricted to

combinations of up to four variables. In the young age group, classification accuracy greater than 80% was seen for MMR and carbonate to phosphate ratio. In the old age group, classification accuracy greater than 80% was observed for cross-linking and MMR.

3.7.4 Multivariate discrimination of age classes: There might not always be a linear or non-linear dependence between bone compositional and mechanical metrics at the tissue level. Therefore, multidimensional projection and classification was used to distinguish young and old mice using Raman and nanoindentation variables. Different data sub-sets were considered for age-based classification: with only Raman variables, with only nanoindentation variables, and with combined Raman and nanoindentation variables. Classification was performed with 2 age classes (4 or 5 months and 19 months) and 3 age classes (4, 5 and 19 months).

The best ranked RadViz projections for all three data sets are shown in figures 3.2, 3.3 and 3.4 respectively and the corresponding best classification scores are given in table 3.4. The best ranked projections in figures 3.2 and 3.3 show that no suitable projections were found where class separation could be achieved with all measurements taken from either only Raman or only nanoindentation experiments. Figure 3.4 shows that VizRank identified a combination of Raman and nanoindentation variables that distinguish the age classes with greater than 80% accuracy. It is evident from figure 3.4 (bottom panel) that 4-month and 5-month old specimens could not be easily distinguished. Hence, the best

projection for classifying three age groups required 8 variables (bottom panel) as compared to only 4 variables for classifying two age groups (top panel).

The prediction accuracy of the best ranked projections found by Vizrank were compared to four standard machine learning approaches: support vector machines (SVM with a linear kernel), k-nearest neighbors (with k equal to square root of number of training instances), naive Bayesian classifier and decision trees. The predictive accuracies were assessed on the 2-age and 3-age class datasets using bootstrap resampling (repeated 100 times) and the performance scores computed using the 0.632 bootstrap estimator. The performance of the classifiers in labeling blinded data was assessed during this procedure. The average classification accuracies and the area under the ROC curve with their respective standard deviations are reported in table 3.5.

Figure 3.5 shows histograms of the seven variables most often used in top-rated RadViz visualizations of the datasets with 2-age classes and 3-age classes respectively. The y-axis score shows the number of appearances of a variable in 100 best ranked projections. The colors of the bars indicate the class that has the highest average association for that variable, which is computed by examining the role of a variable taking into account its interaction with other variables in the data set [28]. The order in which features appear in the histogram reflects their importance. The list of variables defining the best ranked projections holds the most information for class discrimination as seen in top and bottom panels of figure 3.4.

3.8 Discussion

The results revealed an age-dependent pattern in the relationships between nanoindentation and Raman metrics. In young specimens nearing skeletal maturity (table 3.2 center panel), Raman compositional metrics contained more information on the visco-elastic properties (plasticity index, creep metrics), whereas in old specimens with compromised structural integrity (table 3.2 bottom panel), they related better to the measure of hardness (resistance to plastic deformation). The classification accuracies of these results showed that these composition metrics offer only a partial understanding of the mechanical properties at the tissue scale.

Age-dependent patterns were again evident in the results where Raman metrics are the dependent variables. In young specimens (table 3.3 center panel), nanoindentation metrics contained more information on MMR and carb/phos, whereas in aged specimens (table 3.3 bottom panel), they related better to collagen crosslinking. When both age groups were combined (table 3.3 top panel), nanoindentation variables offered more information on the mineralization state (MMR and crystallinity) of the bone. While changes in compositional metrics may be responsible for variations in mechanical properties and vice versa, these results demonstrated that changes in composition and mechanics might be due to other factors that remain unmeasured and interactions that remain unexplored.

The visual projections in figures 3.2 and 3.3 confirmed the hypothesis that it is unlikely that a single variable or a single analytical technique will provide complete information

about bone quality and its transformation through various stages of aging. By analyzing a combination of Raman and nanoindentation variables together, a good classification performance was achieved and a set of variables that contain the most discriminative information were identified. Figure 3.4 depicts the biologically relevant Raman and nanoindentation variables from the present dataset. In the 2 age group dataset, the variables containing the most discriminative information were MMR, crystallinity, plasticity index and modulus. The visualization suggests that the contributions of compositional changes were different in young mice (4 or 5 months) and old (19 months) mice. Higher mineralization and crystallinity were characteristic of 19-month old specimens and possibly contributed to a decrease in structural integrity. In young specimens (4 or 5 months old), increased elastic and viscoelastic modulus contributed to mechanical competence. In the 3 age group dataset, the best projection used a higher number of variables to yield a good separation of the three age classes. While MMR and crystallinity distinguished specimens from the 19-month old group, the visual quality of the classification showed that 4-month old (nearing skeletal maturity) and 5-month old (skeletally mature) mice specimens exhibited similar material properties at the ultrastructural scale. Therefore, metrics corresponding to these two age groups were harder to interpret. This is in agreement with an earlier finding in C57BL/6 mice that while increases in cross-sectional femur geometry continued up to 5 months, material properties appeared to reach peak values at 4 months [29].

Based on classification accuracy (table 3.5 top panel), VizRank performed better than other algorithms in the 2-age classes dataset and ranked third in the 3-age classes dataset. The area under ROC values, as given in table 3.5 (bottom panel), also confirmed that

VizRank performed comparably to other classification algorithms and was stable and robust. Further, VizRank offers an interpretable graphical model that indicates which variables in the data are responsible for class discrimination. The classifier performance can be improved through preprocessing by data transformation. For instance, logarithmic transformation and normalization methods can be used to stabilize variance in the dataset and thereby, improve classification accuracy.

A small set of potentially significant features were identified using VizRank algorithm. MMR and plasticity index were the two most important variables present in the almost 30% of the top-rated projections with the role of separating young (4 or 5 months) and old (19 months) specimens (figure 3.5 top panel). MMR, crystallinity, modulus and hardness were present in almost 30% of the top-rated projections in figure 3.5 (bottom panel). The other variables - crosslinking, plasticity index and creep displacement, appeared in almost 25% of the top 100 projections. Figure 3.5 (bottom panel) portrays the complexity in interpreting short term, age-related changes in bone quality. This study would benefit from adding more clinically relevant age groups and measurements of mechanical and chemical properties across multiple scales. The results presented here suggest that, given a large enough data set, it may be possible to derive sets or rules of metrics that are predictive of ageing effects on the material quality of bone tissue.

3.9 Conclusion

In summary, we have probed the statistical combination of bone quality measures from Raman spectroscopy and nanoindentation testing to distinguish young and old femora.

This was performed by applying RadViz and VizRank classification algorithms to model a combined diagnostic composed of compositional and mechanical measures. Our results demonstrate that not all variables have good discriminatory information. A few selected Raman and nanoindentation variables can reflect the complex changes in bone material properties that occur with aging. Classification was better for the 2-age class dataset than for the 3-age class dataset, because the 4-month and 5-month old specimens exhibited similar material properties. Combinations of multi-scale, multi-technology measures can provide valuable insight into factors affecting bone quality. Such combined measures would be more likely to offer better sensitivities and specificities than individual markers and single out critical features that are relevant for diagnostic purposes.

Table 3.1 Compositional and mechanical metrics determined by Raman spectroscopy and nanoindentation testing for the two age groups (* $p \leq 0.05$)

Variable	Young (4 or 5 months)	Old (19 months)	Difference vs. young (%)
MMR	7.327 ± 0.996	10.18 ± 1.28*	+39
Carbonate/Phosphate	0.267 ± 0.018	0.284 ± 0.029*	+6
Crystallinity	0.0534 ± 0.0004	0.0544 ± 0.0005*	+2
Cross-linking	2.08 ± 0.36	1.92 ± 0.22	-4
Modulus (GPa)	7.55 ± 1.97	8.11 ± 2.30	+7
Hardness (GPa)	1.22 ± 0.41	1.40 ± 0.45	+13
Plasticity index	0.77 ± 0.03	0.76 ± 0.03	-0.2
Creep displacement (nm)	833 ± 336	823 ± 360	-1
Creep modulus parallel (GPa)	884 ± 782	992 ± 740	+12
Creep viscosity parallel(GPa-s)	11200 ± 8826	12175 ± 8280	+9
Creep viscosity series (GPa-s)	15179 ± 15166	15508 ± 17900	+2

Table 3.2 Nanoindentation vs. Raman metrics for both age groups (top), young age group (center) and old age group (bottom)

Dependent class (Discretized)	Classification Accuracy	Independent variables used in the top projection
Modulus (Cutoff = 7.64)	66%	C/P, Crystallinity, MMR, Cross-linking
Hardness (Cutoff = 1.23)	77%	Crosslinking, MMR, Exercise
Plasticity index (Cutoff = 0.77)	80%	MMR, Crystallinity, C/P, Age
Creep displacement (Cutoff = 812.4)	67%	Cross-linking, Crystallinity, MMR, Exercise
Creep modulus parallel (Cutoff = 674)	65%	Age, MMR, Exercise, Cross-linking
Creep viscosity parallel (Cutoff = 9117)	66%	MMR, Crosslinking, Age, Exercise
Creep viscosity series (Cutoff = 8556)	78%	MMR, Crosslinking, Age, Exercise
Modulus (Cutoff = 7.37)	75%	MMR, Crosslinking, C/P, Crystallinity
Hardness (Cutoff = 1.15)	67%	MMR, Crosslinking, Exercise
Plasticity index (Cutoff = 0.76)	86%	C/P, Crosslinking, MMR, Exercise
Creep displacement (Cutoff = 812.4)	63%	Crosslinking, MMR, Exercise
Creep modulus parallel (Cutoff = 565)	84%	MMR, Crystallinity, Crosslinking, Exercise
Creep viscosity parallel (Cutoff = 8324)	84%	MMR, Crystallinity, Crosslinking, Exercise
Creep viscosity series (Cutoff = 8605)	75%	MMR, Crystallinity, Crosslinking, Exercise
Modulus (Cutoff = 8.0)	50%	MMR, Crystallinity, Crosslinking, Exercise
Hardness (Cutoff = 1.32)	87%	MMR, Crystallinity, Crosslinking, Exercise
Plasticity index (Cutoff = 0.77)	75%	Crystallinity, MMR, C/P, Exercise
Creep displacement (Cutoff = 819)	65%	Crosslinking, Exercise, MMR
Creep modulus_parallel (Cutoff = 907)	65%	Crosslinking, Exercise, MMR
Creep viscosity_parallel (Cutoff = 11352)	65%	Crosslinking, Exercise, MMR
Creep viscosity_series (Cutoff = 7703)	65%	Crosslinking, MMR, Exercise

Table 3.3: Raman vs. nanoindentation metrics for both age groups (top), young age group (center) and old age group (bottom)

Dependent class (Discretized)	Classification Accuracy	Independent variables used in the top projection
Carb/Phos (cutoff = 0.27)	80%	Hardness, Plasticity index, Modulus, Age
Crystallinity (Cutoff = 0.054)	92%	Creep viscosity parallel, Plasticity index, Age, Creep modulus parallel
MMR (cutoff = 8.79)	96%	Creep displacement, Age, Hardness, Modulus
Crosslinking (cutoff = 1.96)	71%	Hardness, Modulus, Age and Plasticity index

Dependent class (Discretized)	Classification Accuracy	Independent variables used in the top projection
Carb/Phos (cutoff = 0.27)	86%	Creep modulus parallel, Hardness, Modulus, Creep viscosity parallel
Crystallinity (Cutoff = 0.053)	69%	Creep displacement, Hardness, Creep viscosity parallel, Modulus
MMR (cutoff = 7.15)	88%	Modulus, Hardness, Creep viscosity parallel, Creep viscosity series
Crosslinking (cutoff = 1.96)	78%	Modulus, Creep viscosity series, Plasticity index, Creep modulus parallel

Dependent class (Discretized)	Classification Accuracy	Independent variables used in the top projection
Carb/Phos (cutoff = 0.27)	76%	Hardness, Modulus Creep viscosity parallel, Creep modulus parallel
Crystallinity (Cutoff = 0.054)	74%	Creep modulus parallel, Plasticity index, Hardness, Exercise
MMR (cutoff = 8.79)	83%	Hardness, Modulus, Plasticity index, Creep viscosity series
Crosslinking (cutoff = 1.96)	90%	Creep modulus parallel, Creep displacement, Hardness, Exercise

Table 3.4: Raman and nanoindentation data sets used in the experimental analysis

Data Set	Specimens (Sample points)	Variables (dimensions)	Age classes	Best projection score
Raman	33	4	2*	79.0%
			3	59%
Nanoindentation	33	7	2*	63.0%
			3	62.3%
Combined	33	11	2*	**96 %**
			3	**86%**

* 4-month & 5-month old specimens combined into a single group

Table 3.5: Bootstrap estimated classification accuracy (top) and area under ROC (bottom) of VizRank compared to four standard machine learning algorithms

Classification Accuracy	Data set	
	2 age classes	**3 age classes**
VizRank	89.5 ± 11.5	73.0 ± 14.3
SVM	87.6 ± 19.8	76.2 ± 18.9
kNN	85.7 ± 11.9	77.5 ± 13.1
Naive Bayes	84.6 ± 11.8	62.9 ± 14.1
Decision trees	87.2 ± 8.2	72.6 ± 13.3

Area under ROC	Data set	
	2 age classes	**3 age classes**
VizRank	0.94 ± 0.12	0.85 ± 0.12
SVM	0.91 ± 0.21	0.92 ± 0.13
kNN	0.90 ± 0.13	0.87 ± 0.11
Naive Bayes	0.87 ± 0.11	0.77 ± 0.12
Decision trees	0.87 ± 0.09	0.83 ± 0.11

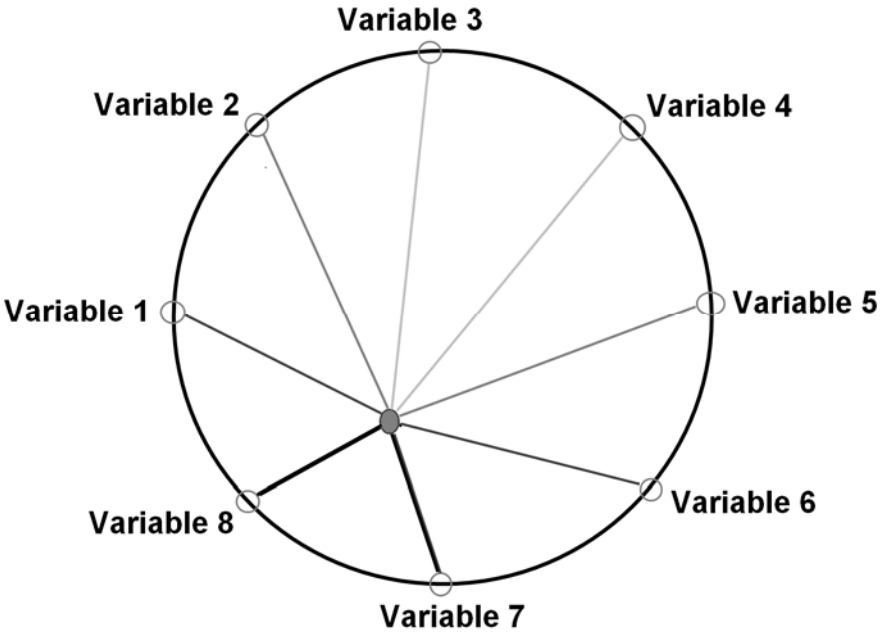

Figure 3.1 RadViz representation of a specimen point with eight dimensions.

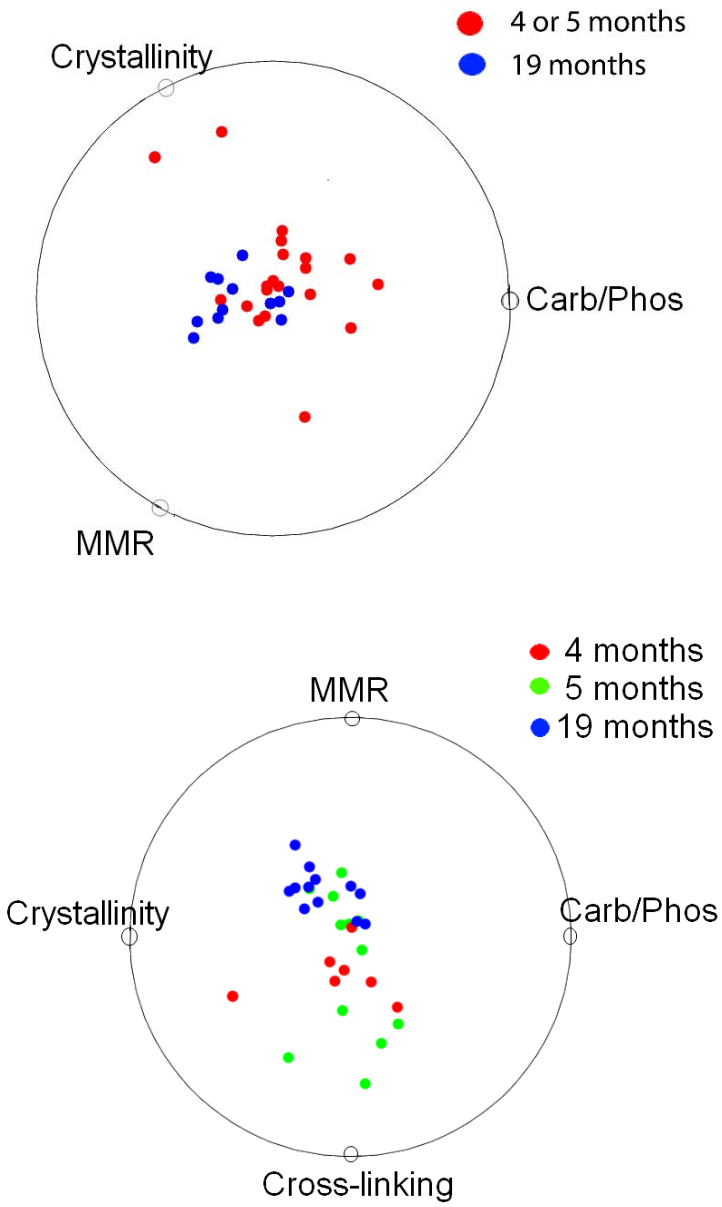

Figure 3.2 Classification using only Raman variables for 2 age groups (top) and 3 age groups (bottom). The projection scores for the best quality RadViz projections computed by VizRank are 79% and 59% respectively.

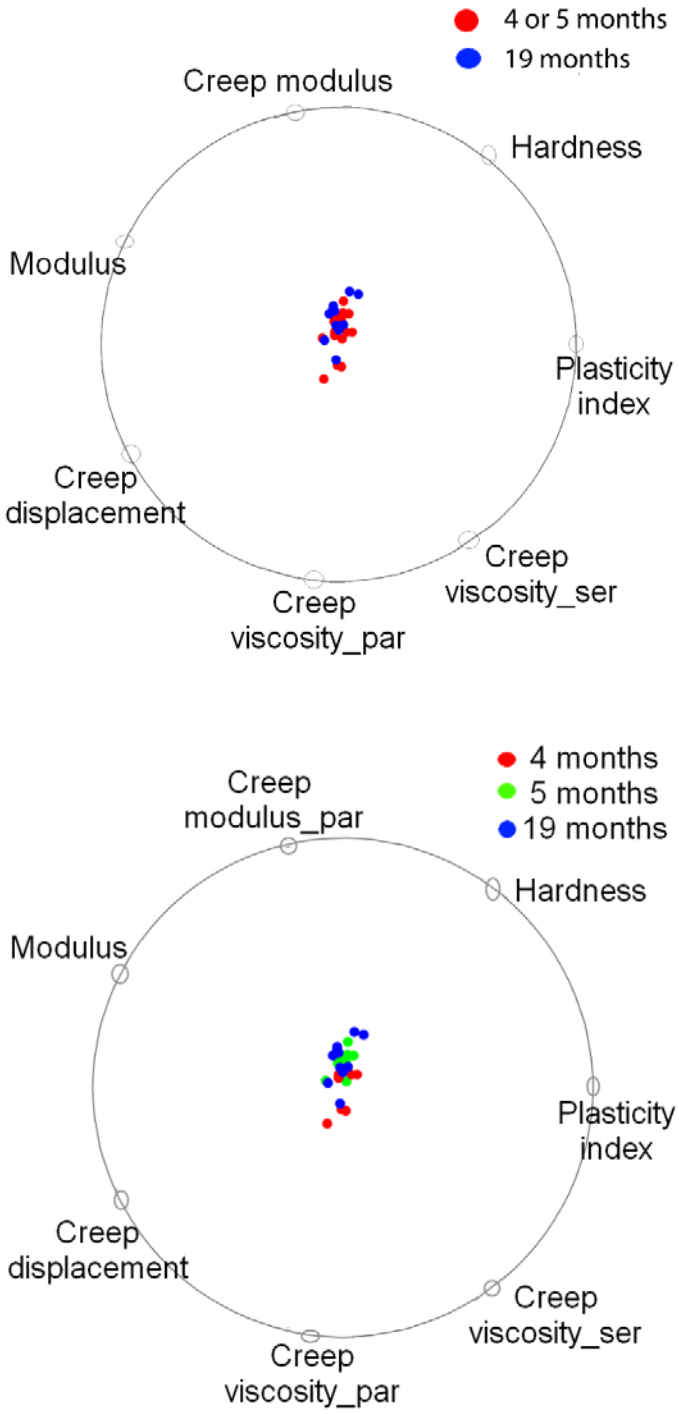

Figure 3.3 Classification using only nanoindentation variables for 2 age groups (top) and 3 age groups (bottom). Projection scores for the best quality RadViz projections computed by VizRank are 63% and 62% respectively.

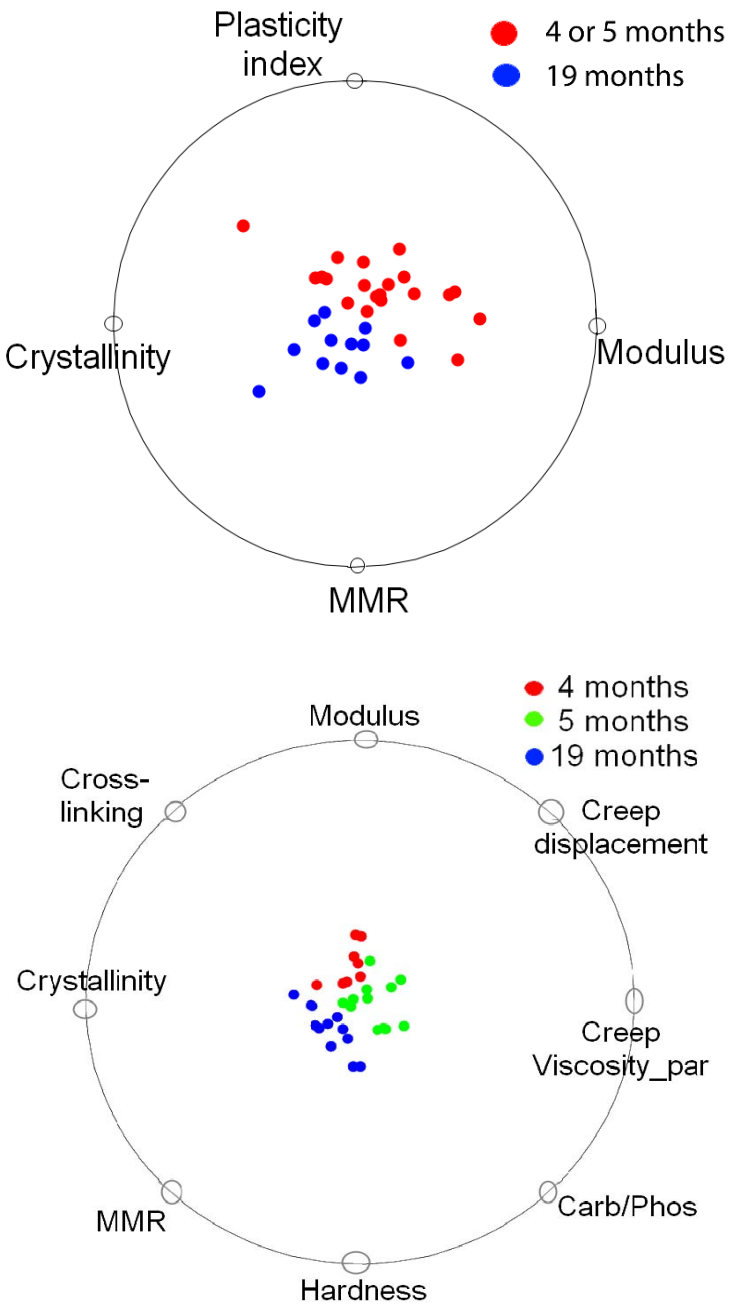

Figure 3.4 Classification using both Raman and nanoindentation variables to classify 2 age groups (top) and 3 age groups (bottom). Projection scores for the best quality RadViz projections computed by VizRank are 96% and 86% respectively.

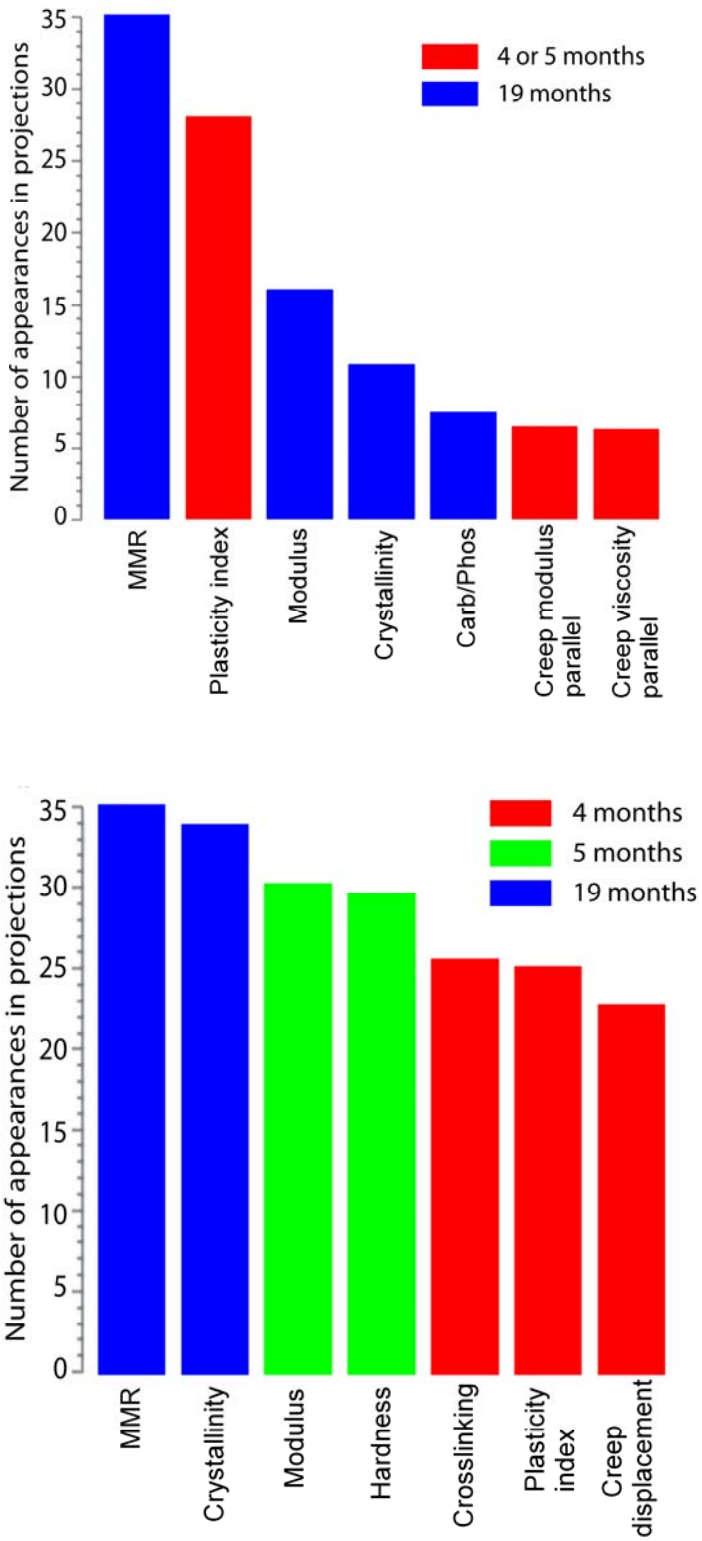

Figure 3.5 A histogram of the seven Raman and nanoindentation variables most often used in the top 100 RadViz visualizations of the dataset with 2 age groups (top) and with 3 age groups (bottom).

References

[1] S. R. Cummings, D. B. Karpf, F. Harris, H. K. Genant, K. Ensrud, A. Z. LaCroix, D. M. Black, Improvement in spine bone density and reduction in risk of vertebral fractures during treatment with antiresorptive drugs, The American Journal of Medicine 112 (2002) 281-289.

[2] J. Currey, Bone architecture & fracture, Current Osteoporosis Reports 3 (2005) 52-56.

[3] E. Paschalis, Fourier transform infrared analysis and bone, Osteoporosis International 20 (2009) 1043-1047.

[4] M. D. Morris, Raman spectroscopy of bone and cartilage, In: P. Matousek, M. D. Morris, editors. Emerging Raman Applications and Techniques in Biomedical and Pharmaceutical Fields: Springer Berlin Heidelberg; 2009, pp. 347-364.

[5] D. Leeming, P. Alexandersen, M. Karsdal, P. Qvist, S. Schaller, L. Tankó, An update on biomarkers of bone turnover and their utility in biomedical research and clinical practice, European Journal of Clinical Pharmacology 62 (2006) 781-792.

[6] P. Fratzl, H. S. Gupta, E. P. Paschalis, P. Roschger, Structure and mechanical quality of the collagen-mineral nano-composite in bone, Journal of Materials Chemistry 14 (2004) 2115-2123.

[7] O. Akkus, F. Adar, M. B. Schaffler, Age-related changes in physicochemical properties of mineral crystals are related to impaired mechanical function of cortical bone, Bone 34 (2004) 443-453.

[8] J. S. Yerramshetty, O. Akkus, The associations between mineral crystallinity and the mechanical properties of human cortical bone, Bone 42 (2008) 476-482.

[9] R. K. Nalla, J. J. Kruzic, J. H. Kinney, M. Balooch, J. W. Ager Iii, R. O. Ritchie, Role of microstructure in the aging-related deterioration of the toughness of human cortical bone, Materials Science and Engineering: C 26 (2006) 1251-1260.

[10] E. P. Paschalis, F. Betts, E. DiCarlo, R. Mendelsohn, A. L. Boskey, FTIR microspectroscopic analysis of human iliac crest biopsies from untreated osteoporotic bone, Calcified Tissue International 61 (1997) 487-492.

[11] S. Hengsberger, A. Kulik, P. Zysset, Nanoindentation discriminates the elastic properties of individual human bone lamellae under dry and physiological conditions, Bone 30 (2002) 178-184.

[12] L. M. Miller, W. Little, A. Schirmer, F. Sheik, B. Busa, S. Judex, Accretion of bone quantity and quality in the developing mouse skeleton, Journal of Bone and Mineral Research 22 (2007) 1037.

[13] E. Donnelly, A. L. Boskey, S. P. Baker, M. C. H. van der Meulen, Effects of tissue age on bone tissue material composition and nanomechanical properties in the rat cortex, Journal of Biomedical Materials Research. Part A 92A (2009) 1048-1056.

[14] Y. Saeys, I. Inza, P. Larranaga, A review of feature selection techniques in bioinformatics, Bioinformatics 23 (2007) 2507-2517.

[15] D. P. Enot, W. Lin, M. Beckmann, D. Parker, D. P. Overy, J. Draper, Preprocessing, classification modeling & feature selection using flow injection electrospray mass spectrometry metabolite fingerprint data, Nature Protocols 3 (2008) 446-470.

[16] S. M. Norton, P. Huyn, C. A. Hastings, J. C. Heller, Data mining of spectroscopic data for biomarker discovery, Current Opinion in Drug Discovery & Development 4 (2001) 325 - 331.

[17] N. Sahar, M. Raghavan, M. D. Morris, D. H. Kohn, Compositional changes of bone mineral and matrix have correlations with mechanical properties that may depend on bone age, Orthopaedic Research Society Transactions 35 (2010) 0067.

[18] V. L. Ferguson, R. A. Ayers, T. A. Bateman, S. J. Simske, Bone development and age-related bone loss in male C57BL/6J mice. Bone 33 (2003) 387-398.

[19] J. M. Somerville, R. M. Aspden, K. E. Armour, K. J. Armour, D. M. Reid, Growth of C57BL/6 mice and the material and mechanical properties of cortical bone from the tibia. Calcified Tissue International 74 (2004) 469-475.

[20] M. D. Brodt, C. B. Ellis, M. J. Silva, Growing C57Bl/6 mice increase whole bone mechanical properties by increasing geometric and material properties. Journal of Bone & Mineral Research 14 (1999) 2159-2166.

[21] N. D. Sahar. Investigating the effects of age and exercise on bone composition and the impact of composition on mechanical integrity (Doctoral dissertation). In: University of Michigan Ann Arbor; 2009.

[22] P. Hoffman. DNA visual and analytic data mining. In: IEEE Visualization. Phoenix, AZ; 1997. p. 437-441.

[23] M. Ankerst, D. Keim, H.-p. Kriegel. Circle segments: A technique for visually exploring large multidimensional data sets. In: IEEE Visualization, Hot Topic Session. San Francisco, CA; 1996.

[24] W. J. Fu, R. J. Carroll, S. Wang, Estimating misclassification error with small samples via bootstrap cross-validation, Bioinformatics 21 (2005) 1979-1986.

[25] G. Leban, B. Zupan, G. Vidmar, I. Bratko, VizRank: data visualization guided by machine learning, Data Mining and Knowledge Discovery 13 (2006) 119-136.

[26] U. M. Braga-Neto, E. R. Dougherty, Is cross-validation valid for small-sample microarray classification?, Bioinformatics 20 (2004) 374-380.

[27] J. Demsar, B. Zupan, G. Leban, T. Curk. Orange: from experimental machine learning to interactive data mining. In: J.-F. Boulicaut, F. Esposito, F. Giannotti, D. Pedreschi, editors. Knowledge Discovery in Databases: PKDD; 2004. p. 537-539.

[28] M. Mramor, G. Leban, J. Demsar, B. Zupan, Visualization-based cancer microarray data classification analysis, Bioinformatics 23 (2007) 2147-2154.

[29] M. D. Brodt, C. B. Ellis, M. J. Silva, Growing C57Bl/6 mice increase whole bone mechanical properties by increasing geometric and material properties, Journal of Bone and Mineral Research 14 (1999) 2159-2166.

CHAPTER 4

Raman spectroscopic study of deuterated bone tissue

4.1 Introduction

Water is an important, but often overlooked component of bone tissue, with influences on the structure and stability of both the mineral and the collagenous matrix. For example, collagen has an internal hydration layer that mediates hydrogen bonding in the triple helix. The collagen hydrogen bonds are of two types: interchain peptide-peptide and peptide-water hydrogen bonds [1, 2]. Referring to the conventional Gly-X-Y notation, the interchain peptide-peptide hydrogen bonds include direct hydrogen bonds between the backbone NH group of glycine and the backbone C=O group of a residue in the X-position of the neighboring chain, usually proline [3], and indirect hydrogen bonds formed by water bridges between the backbone NH group of proline in the X-position and the C=O group of glycine [4]. In bone mineral, several different water environments including water in the c-axis vacancies, in vacancies elsewhere in the crystallites and in the electrolyte-rich monolayer or very thin layer at the crystallite surfaces, have been previously identified [5].

Studies investigating bone dehydration and replacement of water with polar solvents in bone and dentin have demonstrated tissue shrinkage and an increase in the tensile strength, brittleness and stiffness of the tissue. These effects are a consequence of

increased direct collagen-collagen hydrogen-bonding as fewer hydrogen-bonding sites are occupied by the solvent. This leads to change in the bonding patterns and the hydration structure and hence, changes in the matrix protein conformation [6-12].

A model system to study the aqueous environment of bone tissue is achieved by replacing water (H_2O) with deuterium oxide (D_2O). Deuterium oxide forms hydrogen bonds that are stronger by ~0.1 - 0.2 kcal mol^{-1} than water while having a similar size. Equilibration of a bone tissue specimen with a D_2O-based buffer will result in partial or complete replacement of collagen water with D_2O [13]. Side chains in the X and Y positions of the collagen Gly-X-Y sequence are exposed to the molecular surface and hence, could be affected by solvent exchange. The labile water on the mineral crystallite surface layer is also expected to exchange with D_2O. Knowledge of the influence of D_2O on the molecular components of bone may be important in identifying how water interacts with collagen and mineral at the ultrastructural scales.

Raman spectroscopy makes it possible to explore the effects of solvent environment on protein and mineral structure. As a general rule, hydrogen bonding lowers the frequency of stretching vibrations, but increases the frequency of bending vibrations [14]. For vibrational modes of carbonyl groups the shifts may be no more than a few wavenumbers, although there can be much larger shifts for OH and NH vibrations. The effect of H-bonding on the peptide linkage is to shorten the C-N bond and to lengthen the C=O bond. The amide I band in the bone infrared spectrum (1665 cm^{-1} & 1685 cm^{-1}) has been used as an indirect measure of the maturity of collagen cross-links with realization

that collagen secondary structure changes are the source of the effect [15, 16]. The same spectroscopic measures of collagen secondary structure have been used in bone Raman spectroscopy as metrics for cross-link distortion and rupture under mechanical load [17]. The 1665 cm^{-1} band of amide I arises mainly from the C=O stretching vibration with minor contributions from the out-of-phase CN stretching vibration, the CCN deformation and the NH in-plane bend. The latter is responsible for the sensitivity of the amide I band to N-deuteration of the backbone.

In this study, we analyzed the effects of D_2O equilibration on the collagen and mineral components of bone tissue using Raman spectroscopy. The solvent environment was manipulated by equilibrating bone tissue with phosphate-buffered saline (PBS) prepared in different concentrations of D_2O. Changes in mineral and matrix Raman bands on H/D (H_2O to D_2O) exchange were observed in the different treatment groups.

4.2 Specimen preparation

Left and right femora were harvested from fifteen mice (strain: C57BL/6J male, age: 4 weeks) were used. Five samples of about 1 mm length were sectioned from the mid-diaphyses of the right and left femora using a low-speed sectioning saw. For each mouse, five bone samples each were equilibrated in PBS prepared with known D_2O/H_2O mixtures (0%, 25%, 50%, 75% and 100%) for twelve hours. D_2O (99.99 atom%) was purchased from Sigma-Aldrich (St. Louis, MO). After equilibration, the cross-sections were frozen until use. The specimens were thawed before collection of spectra. They

were kept moist throughout an experiment by a drip of PBS prepared with the appropriate D_2O/H_2O mixture.

4.3 Raman spectroscopy

Raman spectra were collected from the femoral cross-sections using a locally-constructed Raman microprobe that has been described [18]. The system was constructed around a Nikon E600 microscope frame (Nikon USA, Melville, NY). The exciting laser was a 400 mW, 785 nm diode laser (Invictus, Kaiser Optical Systems Inc., Ann Arbor, MI) from which the circularizing optics had been removed to allow line-focusing. The line focus enabled the simultaneous collection of 126 spectra (one for each row of pixels on the CCD detector). An axial transmissive imaging spectrograph (Holospec, Kaiser Optical Systems Inc., Ann Arbor, MI) with 25 μm entrance slit (approx. 4 cm^{-1} resolution) and a 1024x256 pixel deep depletion charge-coupled device detector (Andor Technology, South Windsor, CT) were used to disperse and record the spectrum.

Raman spectra were acquired from the D_2O/H_2O-equilibrated samples through a 40X, 0.90 NA objective (Nikon USA, Melville, NY) at an exposure time of 120s for unpolarized spectra and 180s for polarized spectra. The polarization direction of the beam was selected using a half-wave plate. The collected Raman scatter was passed through an analyzing polarizer and a wedge depolarizer and directed onto the slit of the spectrograph. In order to measure the polarization dependence of Raman bands, parallel-polarized (I_{par}) and cross-polarized spectra (I_{perp}) were obtained with the analyzer polarization oriented parallel and perpendicular to the incident linearly polarized light.

4.4 Spectral processing and data analysis

The wavenumber scale of the spectrograph was calibrated against the emission lines of a neon lamp discharge. Intensities were corrected for polarization dependence of the optics by calibration against cyclohexane. The spectra were corrected for spectrograph image curvature. Dark current subtraction and white light correction (flat-fielding) were performed using locally written scripts on MATLAB (Mathworks Inc., Natick, MA). Spectra were analyzed and peak fitting was performed using GRAMS/AI 7.01 (Thermo Galactic, Waltham, MA). The peak positions, widths and intensities of the characteristic mineral bands were measured: phosphate ν_1 (959 cm^{-1}) and carbonate ν_1 (1071 cm^{-1}). Likewise, the peak positions and areas of the collagen bands were measured: amide I (1665 cm^{-1} and 1685 cm^{-1}) and hydroxyproline (855 cm^{-1} and 876 cm^{-1}). Depolarization ratios, $R = I_{perp}/ I_{par}$, were calculated for the phosphate band for the different D_2O/H_2O-equilibrated groups.

Raman metrics measured on the different D_2O/H_2O-equilibrated groups were analyzed using Friedman's two-way analysis of variance, a nonparametric equivalent of repeated-measures ANOVA (SPSS 18, Chicago, IL). A nonparametric post hoc test was used for multiple comparisons between D_2O concentrations. For all analyses, $p \leq 0.05$ was considered significant. Effect size, *r*, was calculated using the Wilcoxon signed-rank test. The value of *r* for small, medium and large sizes was considered to be 0.1, 0.3 and 0.5 respectively. Non-linear visualization and classification algorithms were then applied to identify Raman metrics which are most important in classifying the different D_2O/H_2O

treatment groups. RadViz and VizRank algorithms have been described earlier in Chapter 3 and were implemented within Orange data mining software.

4.5 Results

Table 4.1 shows the descriptive statistics for the Raman spectroscopic measures of bone mineral and matrix in each of the D_2O/H_2O treatment groups. All Raman measures except mineral to matrix ratio (MMR) significantly differed among D_2O/H_2O treatment groups, such as (a) phosphate peak position ($p<0.05$, Friedman's chi-square 24.4), (b) mineral crystallinity ($p<0.05$, Friedman's chi-square 9.76), (c) carbonate peak position ($p<0.05$, Friedman's chi-square 9.52), (d) carbonate to phosphate ratio ($p<0.05$, Friedman's chi-square 10.03), (e) phosphate depolarization ratio ($p<0.05$, Friedman's chi-square 10.64), (f) hydroxyproline 855 cm^{-1} peak ($p<0.05$, Friedman's chi-square 34.96) and 875 cm^{-1} peak position ($p<0.05$, Friedman's chi-square 18.16), (g) amide I 1660 cm^{-1} peak ($p<0.05$, Friedman's chi-square 28.4) and 1680 cm^{-1} peak position ($p<0.05$, Friedman's chi-square 20.8).

Post hoc multiple comparisons on the mineral bands showed that the shift in phosphate peak position to a higher wavenumber in the 100% D_2O/H_2O treatment group compared to 0%, 25% and 50% D_2O/H_2O treatment groups was statistically significant. The shift in carbonate peak position to a higher wavenumber for the 100% D_2O/H_2O treatment group compared to the 25% D_2O/H_2O treatment group was statistically significant. However, the shift in carbonate peak position was less than for phosphate. The apparent carbonate to phosphate ratio was significantly higher for the 100% D_2O/H_2O treatment group

compared to the 25% D_2O/H_2O treatment group, suggesting that with shifts in corresponding peak positions, these bands are no longer fully resolved. The depolarization ratio for phosphate was significantly reduced on equilibration with 100% D_2O/H_2O as compared to 0% D_2O/H_2O solution.

Post hoc multiple comparisons on the collagen bands showed that the hydroxyproline peak position shifted to lower wavenumbers on equilibration with deuterium oxide. Specifically, for the 855 cm^{-1} hydroxyproline band, the peak positions for the 75% and 100% D_2O/H_2O treatment groups were significantly lower compared to that of 0% and 25% D_2O/H_2O treatment groups. The 875 cm^{-1} peak position was significantly lower for the 100% D_2O/H_2O treatment group compared to that of the 50% treatment group. The amide I Raman bands also exhibited a shift to lower wavenumbers on equilibration with deuterium oxide. For the 1660 cm^{-1} amide I band, the peak positions for the 50%, 75% and 100% D_2O/H_2O treatment groups were significantly lower compared to the 0% treatment group. For the 1680 cm^{-1} amide I band, the peak position for the 75% D_2O/H_2O treatment group was significantly lower than that of the 0%, 25% and 50% treatment groups and the peak position of the 100% D_2O/H_2O treatment group was significantly lower compared to the 0% treatment group. Wilcoxon signed-rank tests revealed a medium to large effect size ($r = 0.43$ to 0.72) on D_2O/H_2O treatment. No statistically significant trend within individual treatment groups was observed for other metrics.

All Raman spectroscopic measures of bone mineral and collagen from this study were evaluated for their ability to discriminate between the five D_2O/H_2O treatment groups.

The best RadViz projections for this five class dataset using only collagen measures and only mineral measures are shown in figure 4.1. The classification scores computed by VizRank for these projections were 47% and 39% respectively. Combining collagen and mineral measures provided a projection with an increased classification accuracy of 68% as shown in figure 4.2. However, even with the use of seven Raman measures, the five treatment groups were not discriminated. Specimen points corresponding to 0%, 25% and 50% D_2O/H_2O treatment groups are clustered together and separated from the cluster formed by the 75% and 100% D_2O/H_2O groups. The non-parametric test results also show that significant differences in Raman metrics are observed primarily in the 75% and/or 100% D_2O/H_2O treatment groups compared to other groups.

The five class dataset was converted into a two class dataset by combining the 0%, 25% and 50% D_2O/H_2O treatment groups into one class and the 75% and 100% D_2O/H_2O treatment groups into another. The best RadViz projections for this two class dataset using only collagen measures and only mineral measures (figure 4.3) yielded classification scores of 66% and 67% respectively. Combining collagen and mineral measures provided a projection with a classification accuracy of 96.5% (figure 4.4). The variables holding the most discriminative information were hydroxyproline 855 cm^{-1} peak position, amide I 1660 cm^{-1} peak position and mineral crystallinity.

4.6 Discussion

The decrease in amide I and hydroxyproline wave numbers on deuteration offer insights into the role of hydrogen bonding in collagen fibrils. Water bridges contribute to chain

stabilization [19]. As H/D exchange occurred, labile protons on the amino acids, especially on glycine, were replaced by deuterium ions. On deuteration of the glycine amine and the hydroxyl groups of hydroxyproline, the hydroxyproline Raman bands shifted down in frequency. The shifts in amide I bands could also result from loss of water bridges, i.e. water-mediated hydrogen bonds. These observations indicate a change in the secondary structure and dynamics of collagen as a result of H/D exchange. In these experiments, an increase in the 1685 cm^{-1} component of amide I with deuteration was not observed. Increases in this band have been associated with the lack of mature interfibrillar cross-links, whether from mechanical damage [17], osteoporosis [16] or collagen immaturity [20]. However, we cannot conclude definitively from our measurements whether mature cross-links are broken or distorted with deuteration.

The hydrogen bond in H_2O is shorter and more asymmetric than in D_2O [21]. The influence of H/D exchange on the stability of globular proteins and collagen model peptides has been studied using circular dichroism and differential scanning calorimetry [22, 23]. While the increased strength of the hydrogen bond of D_2O was found to increase the stability of the proteins, the mechanism of stability remains unclear. A recent NMR study on bovine cortical bone specimens reported that dehydration and H/D exchange caused similar spectral changes due to local conformational disorder of the collagen matrix [24]. Dehydration of bone results in closer spacing of collagen fibrils [25]. Hence, the changes in collagen Raman bands on deuteration could be similarly explained by the increased rigidity of the protein structure due to the increased strength of the hydrogen bonds of D_2O.

While the primary effect of H/D exchange was observed in collagen bands, a significant increase in phosphate and carbonate peak positions, mineral crystallinity and carbonate to phosphate ratio occurred on equilibration with 100% D_2O/H_2O. We hypothesize that these observed changes are related to the compression of the mineral phase in response to stiffening of collagen fibrils on H/D exchange. It is unlikely that mineral composition was affected by H/D exchange. The reduced spacing of the collagen molecules would change the strain environment of the mineral lattice. This is in agreement with an earlier study which reported that fixation of bones with ethanol and glycerol had a significant effect on apparent mineral crystallinity [26]. Synchrotron diffraction and scattering studies on bone have also shown that drying and consequent stiffening of collagen increases the strain fraction carried by mineral particles in the mineralized fibril [27].

The increased polarization of the phosphate Raman band on deuteration indicates changes to the degree of mineral crystallite orientation. The mineral crystallites are mainly within the gap regions within the collagen fibril [28] and the crystallographic c-axes are aligned with the fibril long axis [29, 30]. In a polarized Raman study of dental caries, disordered mineral was reported to increase the depolarization ratio of the phosphate 959 cm^{-1} peak [31]. In contrast, collagen stiffening on deuteration would compress the mineral crystallites, causing them to become better oriented, which is reflected in the decreased Raman depolarization ratio of the 959 cm^{-1} peak in this study.

Compression of the mineral crystallite lattice causes the anions within the apatite unit cell to be compressed. However, the carbonate ion compresses less than the phosphate ion

[32, 33]. This could explain why the observed change in Raman shift for carbonate was less than for phosphate. Similar changes in bone mineral bands have been observed during high-pressure Raman spectroscopy [34]. While spectroscopic changes were observed in amide I collagen even at 50% H/D exchange, a significant increase in wavenumber for the mineral bands were evident only at 100% H/D exchange. In addition, spectral changes in the mineral bands on H/D exchange were no greater than ~1-2 cm^{-1}. These observations for the mineral bands can be understood on the basis that compression of the phosphate ion is two to four times smaller than lattice compression [33]. Therefore, as collagen fibrils stiffen on H/D exchange and compress the mineral lattice, the spectroscopic changes reflecting the compression on the phosphate ion can be too small to be detected by Raman spectroscopy until a certain compressive stress threshold is reached.

Interpretation of Raman spectral shifts in terms of stress distribution in the mineral lattice is not straightforward [35]. However, assuming uniaxial compressive stress along the main crystallographic direction, the wavenumber shifts of the mineral band can be converted into compressive stress values using known values of $\delta V/\delta P$, the compressive coefficient. $\delta V/\delta P$ represents the average change in position of the mineral Raman band per unit pressure. We used the $\delta V/\delta P$ value of 5.152 cm^{-1}/GPa for phosphate and 3.228 cm^{-1}/GPa for carbonate measured in powdered mouse bone under hydrostatic compression [34]. For spectroscopic shifts of 1.2 cm^{-1} for phosphate peak and 0.4 cm^{-1} for carbonate peak in the 100% D_2O/H_2O treatment group, the corresponding compressive stresses on the phosphate and carbonate ions are estimated to be 233 MPa and 123 MPa

respectively. We hypothesize that these stress values represents the threshold compressive stresses exerted by the stiffening collagen matrix, below which changes in mineral components will be difficult to resolve spectroscopically.

Non-linear, multidimensional visualization of the dataset confirmed that significant changes in bone mineral and matrix Raman bands were observed predominantly in the 75% and 100% D_2O/H_2O groups. When all five treatment groups were included in the classification, collagen and mineral spectroscopic measures provided poor discrimination of the different groups. However, when specimens were grouped into two classes (0%-50% D_2O/H_2O and 75%-100% D_2O/H_2O), the RadViz projections confirmed that classification accuracy improved. The visual quality of the classification showed that specimens belonging to the 0%, 25% and 50% D_2O/H_2O groups exhibited similar mineral and matrix spectroscopic measures. Likewise, classification accuracy improved dramatically when both mineral and matrix Raman measures were included in the classification.

Our results suggest that equilibration with D_2O alters the aqueous and chemical environment of bone tissue. This has practical implications for the interpretation of NMR studies involving H/D exchange in bone tissue. These results also hold clinical relevance for the study of changes in collagen structure accompanying bone disorders [36] and changes in water content bonded to bone mineral and collagen with increasing age [37]. While the present work has focused on the Raman spectroscopic changes due to deuteration, future work will employ cross-polarization NMR studies to study the spatial

relationships between the chemical components of bone mineral and matrix and the influence of water on these interactions.

4.7 Conclusion

Using a combination of D_2O/H_2O concentrations and Raman spectroscopy, we have studied the response of bone mineral and the matrix components to the substitution of H_2O with D_2O. Although the increase in hydrogen bond strength upon deuteration is small, we identified significant shifts in the Raman bands of bone mineral and matrix at high D_2O concentrations. A striking result is that D_2O equilibration not only enhances collagen stability but also compresses the mineral phase. We hypothesize that changes in mineral Raman bands reflect orientation and stress effects and not compositional changes.

Table 4.1: Raman measures of the mineral (top) and matrix (bottom) components reported as mean (SD)

D_2O/H_2O concentration	Phosphate Peak (cm^{-1})	Phosphate crystallinity	Carbonate Peak (cm^{-1})	Carbonate /Phosphate ratio	Phosphate Depolarization Ratio
0%	958.30	.0545	1070.43	0.154	0.088
	(0.39)	(.0013)	(0.63)	(0.007)	(0.054)
25%	958.35	.0546	1069.97	0.153	0.041
	(0.58)	(.0015)	(0.67)	(0.013)	(0.029)
50%	958.47	.0546	1070.81	0.161	0.042
	(0.95)	(.0015)	(0.83)	(0.025)	(0.016)
75%	958.44	.0558	1070.83	0.164	0.035
	(0.66)	(.0021)	(0.47)	(0.019)	(0.009)
100%	959.53	.0564	1070.82	0.178	0.028
	(0.10)	(.0011)	(1.14)	(0.019)	(0.008)
p-value*	<0.05	<0.05	<0.05	<0.05	<0.05

D_2O/H_2O concentration	Hydroxyproline Peak (cm^{-1})		Amide I Peak (cm^{-1})		Mineral to Matrix Ratio
0%	853.05	874.54	1662.25	1682.59	7.80
	(0.65)	(1.49)	(0.79)	(0.98)	(1.18)
25%	851.84	874.46	1660.24	1681.73	7.61
	(0.97)	(0.95)	(0.85)	(1.85)	(1.36)
50%	851.59	875.43	1659.47	1681.29	7.04
	(0.65)	(0.87)	(0.99)	(2.13)	(1.87)
75%	850.50	873.91	1656.75	1677.95	7.53
	(1.01)	(1.48)	(1.78)	(2.30)	(177)
100%	850.09	872.99	1658.24	1679.78	7.93
	(0.80)	(0.90)	(0.64)	(1.51)	(1.56)
p-value*	<0.05	<0.05	<0.05	<0.05	>0.05

(* - p-value comparing the median among 5 treatment groups using Friedman's ANOVA)

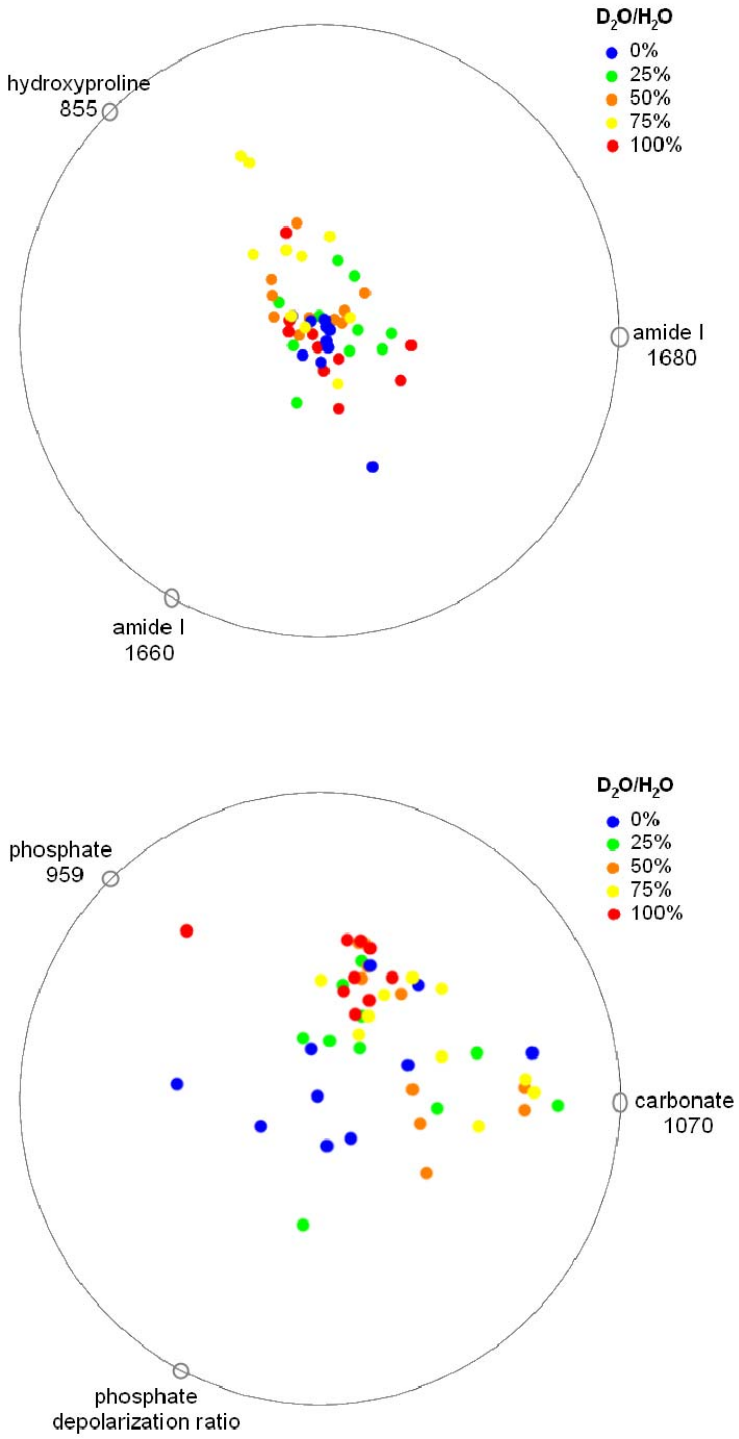

Figure 4.1 Classification of five D_2O/H_2O treatment groups involving only collagen measures (top) and only mineral measures (bottom). The projection scores of the best quality RadViz projections computed by VizRank were 47% and 39% respectively.

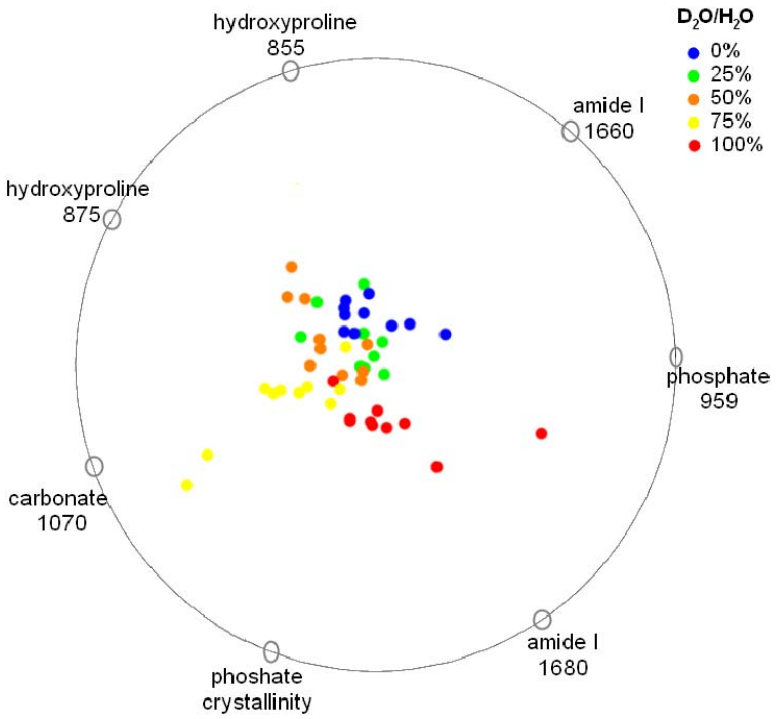

Figure 4.2 Classification of five D_2O/H_2O treatment groups involving both collagen and mineral measures. The projection score of the best quality RadViz projection computed by VizRank was 68%. The specimen points are scaled up by a factor of 1.3 to assist with visualization.

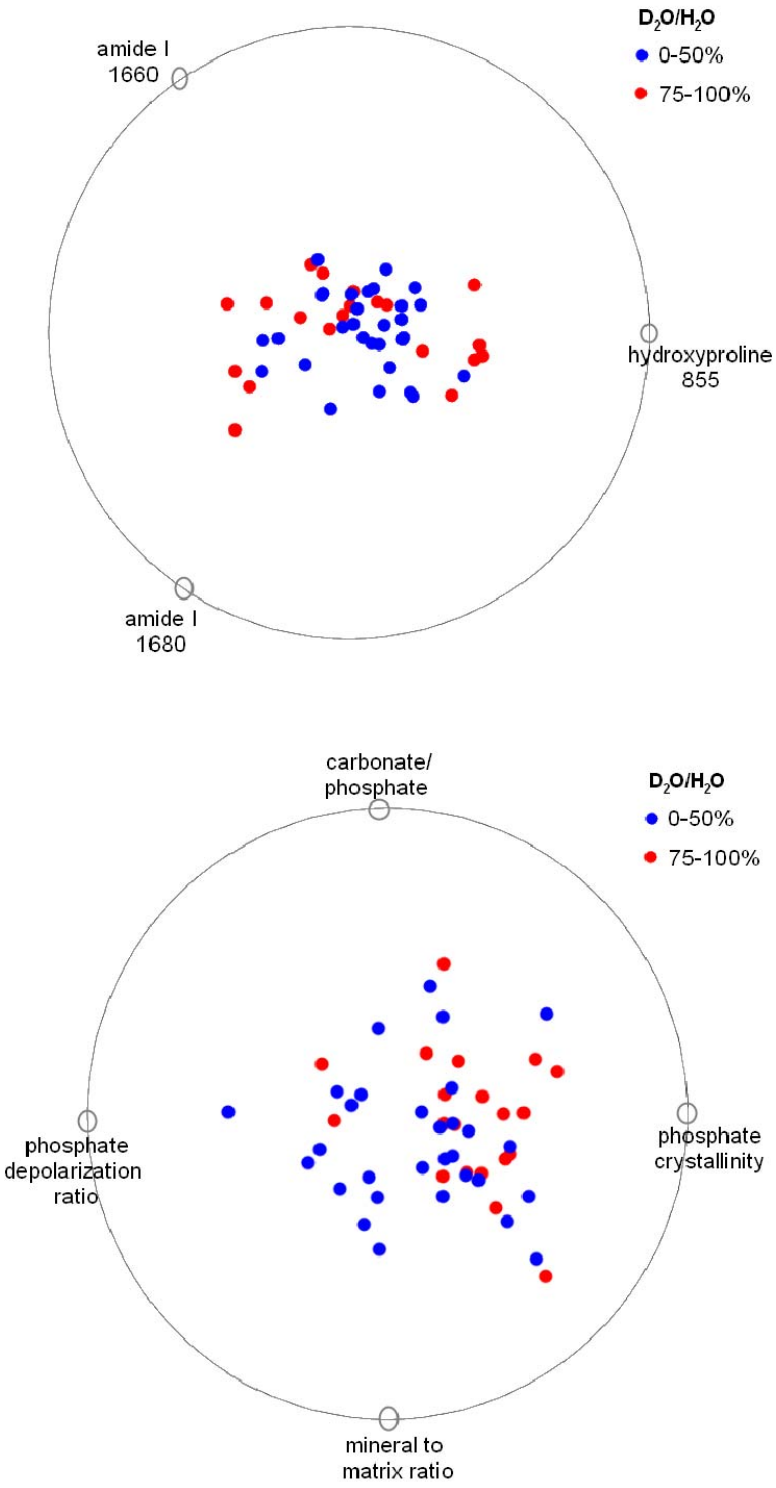

Figure 4.3 Classification of two D_2O/H_2O treatment groups involving only collagen measures (top) and only mineral measures (bottom). The projection scores of the best quality VizRank projections computed by VizRank were 66% and 67% respectively.

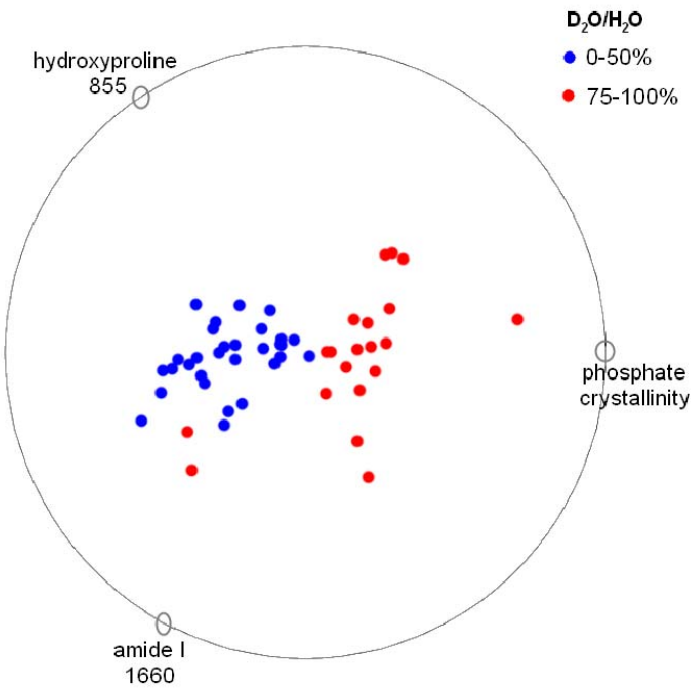

Figure 4.4 Classification of two D_2O/H_2O treatment groups involving both collagen and mineral measures. The projection score of the best quality RadViz projection computed by VizRank was 96.5%.

References

[1] J. Engel, H. P. Bachinger, Structure, stability and folding of the collagen triple helix, In: J. Brinckmann, H. Notbohm, P. K. Muller, editors. Collagen: Primer in Structure, Processing and Assembly: Springer Berlin / Heidelberg; 2005, pp. 7-33.

[2] B. Brodsky, A. V. Persikov, Molecular structure of the collagen triple helix, In: D. A. D. Parry, J. M. Squire, editors. Advances in Protein Chemistry: Academic Press; 2005, pp. 301-339.

[3] A. Rich, F. H. Crick, The molecular structure of collagen, Journal of Molecular Biology 3 (1961) 483-506.

[4] G. N. Ramachandran, R. Chandrasekharan, Interchain hydrogen bonds via bound water molecules in the collagen triple helix, Biopolymers 6 (1968) 1649-1658.

[5] E. E. Wilson, A. Awonusi, M. D. Morris, D. H. Kohn, M. M. J. Tecklenburg, L. W. Beck, Three structural roles for water in bone observed by solid-state NMR, Biophysical Journal 90 (2006) 3722–3731.

[6] K. T. Maciel, R. M. Carvalho, R. D. Ringle, C. D. Preston, C. M. Russell, D. H. Pashley, The effects of acetone, ethanol, HEMA, and air on the stiffness of human decalcified dentin matrix, Journal of Dental Research 75 (1996) 1851-1858.

[7] D. H. Pashley, K. A. Agee, R. M. Carvalho, K. W. Lee, F. R. Tay, T. E. Callison, Effects of water and water-free polar solvents on the tensile properties of demineralized dentin, Dental Materials 19 (2003) 347-352.

[8] D. H. Pashley, K. A. Agee, M. Nakajima, F. R. Tay, R. M. Carvalho, R. S. Terada, F. J. Harmon, W. K. Lee, F. A. Rueggeberg, Solvent-induced dimensional changes in EDTA-demineralized dentin matrix, Journal of Biomedical Materials Research 56 (2001) 273-281.

[9] A. Kishen, A. Asundi, Experimental investigation on the role of water in the mechanical behavior of structural dentine, Journal of Biomedical Materials Research. Part A 73 (2005) 192-200.

[10] R. K. Nalla, M. Balooch, J. W. Ager III, J. J. Kruzic, J. H. Kinney, R. O. Ritchie, Effects of polar solvents on the fracture resistance of dentin: role of water hydration, Acta Biomaterialia 1 (2005) 31-43.

[11] R. K. Nalla, J. H. Kinney, A. P. Tomsia, R. O. Ritchie, Role of alcohol in the fracture resistance of teeth, Journal of Dental Research 85 (2006) 1022-1026.

[12] P. Lucksanasombool, W. A. Higgs, R. J. Higgs, M. V. Swain, Fracture toughness of bovine bone: influence of orientation and storage media, Biomaterials 22 (2001) 3127-3132.

[13] M. A. Fernández-Seara, S. L. Wehrli, F. W. Wehrli, Diffusion of exchangeable water in cortical bone studied by nuclear magnetic resonance, Biophysical Journal 82 (2002) 522-529.

[14] N. Colthup, L. Daly, S. Wiberley, Introduction to Infrared and Raman Spectroscopy. New York: Academic Press; 1975.

[15] R. Mendelsohn, E. P. Paschalis, P. J. Sherman, A. L. Boskey, IR microscopic imaging of pathological states and fracture healing of bone, Applied Spectroscopy 54 (2000) 1183-1191.

[16] E. P. Paschalis, E. Shane, G. Lyritis, G. Skarantavos, R. Mendelsohn, A. L. Boskey, Bone fragility and collagen cross-links, Journal of Bone and Mineral Research 19 (2004) 2000-2004.

[17] A. Carden, R. M. Rajachar, M. D. Morris, D. H. Kohn, Ultrastructural changes accompanying the mechanical deformation of bone tissue: a Raman imaging study, Calcified Tissue International 72 (2003) 166-175.

[18] N. J. Crane, M. D. Morris, M. A. Ignelzi Jr., G. G. Yu, Raman imaging demonstrates FGF2-induced craniosynostosis in mouse calvaria, Journal of Biomedical Optics 10 (2005) 031119.

[19] J. Bella, B. Brodsky, H. M. Berman, Hydration structure of a collagen peptide, Structure 3 (1995) 893-906.

[20] E. P. Paschalis, K. Verdelis, S. B. Doty, A. L. Boskey, R. Mendelsohn, M. Yamauchi, Spectroscopic characterization of collagen cross-links in bone, Journal of Bone and Mineral Research 16 (2001) 1821-1828.

[21] A. K. Soper, C. J. Benmore, Quantum differences between heavy and light water, Physical Review Letters 101 (2008) 065502.

[22] Y. M. Efimova, S. Haemers, B. Wierczinski, W. Norde, A. A. v. Well, Stability of globular proteins in H2O and D2O, Biopolymers 85 (2007) 264-273.

[23] K. Mizuno, H. P. Bächinger, The effect of deuterium oxide on the stability of the collagen model peptides H-(Pro-Pro-Gly)10-OH, H-(Gly-Pro-4(R)Hyp)9-OH, and Type I collagen, Biopolymers 93 (2010) 93-101.

[24] P. Zhu, J. Xu, N. Sahar, M. D. Morris, D. H. Kohn, A. Ramamoorthy, Time-resolved dehydration-induced structural changes in an intact bovine cortical bone revealed by solid-state NMR spectroscopy, Journal of the American Chemical Society 131 (2009) 17064-17065.

[25] S. Lees, A mixed packing model for bone collagen, Calcified Tissue International 33 (1981) 591-602.

[26] Y. Yeni, J. Yerramshetty, O. Akkus, C. Pechey, C. Les, Effect of fixation and embedding on Raman spectroscopic analysis of bone tissue, Calcified Tissue International 78 (2006) 363-371.

[27] H. S. Gupta, J. Seto, W. Wagermaier, P. Zaslansky, P. Boesecke, P. Fratzl, Cooperative deformation of mineral and collagen in bone at the nanoscale, Proceedings of the National Academy of Sciences of the United States of America 103 (2006) 17741-17746.

[28] R. A. Robinson, M. L. Watson, Collagen-crystal relationships in bone as seen in the electron microscope, The Anatomical Record 114 (1952) 383-409.

[29] W. J. Landis, M. J. Song, A. Leith, L. McEwen, B. F. McEwen, Mineral and organic matrix interaction in normally calcifying tendon visualized in three dimensions by high-voltage electron microscopic tomography and graphic image reconstruction, Journal of Structural Biology 110 (1993) 39-54.

[30] S. Weiner, W. Traub, Organization of hydroxyapatite crystals within collagen fibrils, FEBS Letters 206 (1986) 262-266.

[31] A. C. T. Ko, L.-P. i. Choo-Smith, M. Hewko, M. G. Sowa, C. C. S. Dong, B. Cleghorn, Detection of early dental caries using polarized Raman spectroscopy, Optics Express 14 (2006) 203-215.

[32] P. Gillet, C. Biellmann, B. Reynard, P. McMillan, Raman spectroscopic studies of carbonates part I: High-pressure and high-temperature behaviour of calcite, magnesite, dolomite and aragonite, Physics and Chemistry of Minerals 20 (1993) 1-18.

[33] P. Comodi, Y. Liu, M. L. Frezzotti, Structural and vibrational behaviour of fluorapatite with pressure. Part II: in situ micro-Raman spectroscopic investigation, Physics and Chemistry of Minerals 28 (2001) 225-231.

[34] O. de Carmejane, M. D. Morris, M. K. Davis, L. Stixrude, M. Tecklenburg, R. M. Rajachar, D. H. Kohan, Bone chemical structure response to mechanical stress studied by high pressure Raman spectroscopy, Calcified Tissue International 76 (2005) 207-213.

[35] A. Atkinson, S. C. Jain, Spatially resolved stress analysis using Raman spectroscopy, Journal of Raman Spectroscopy 30 (1999) 885-891.

[36] C. Laurent Benhamou, Bone ultrastructure: evolution during osteoporosis and aging, Osteoporosis International 20 (2009) 1085-1087.

[37] J. S. Nyman, Q. Ni, D. P. Nicolella, X. Wang, Measurements of mobile and bound water by nuclear magnetic resonance correlate with mechanical properties of bone, Bone 42 (2008) 193-199.

CHAPTER 5

Raman spectroscopic study of bone mineral behavior on tensile loading

5.1 Introduction

The Raman spectrum is sensitive to changes in mineral parameters such as crystal structure, crystallite size and deviations from stoichiometry [1] and to changes in protein conformation [2]. Because these ultrastructural parameters change with age and mechanical loading, Raman spectroscopy is a powerful tool for assessing the effects of these parameters on the bone tissue. Biomechanical studies on the bone have focused on relating the biology and the mechanics of the tissue. Because of the hierarchical nature of bone, the biomechanical testing of bone at different levels of scale can be used to isolate changes at each level which affect the bone quality. It is well-known that the organization of the bone ultrastructure i.e., collagen conformation, cross-linking, mineral type, crystal alignment and collagen-mineral interfaces, determine the mechanical behavior of bone [3]. However, the structural behavior of mineral and its influence on the overall mechanical properties of bone has been more difficult to evaluate.

Raman spectroscopy is well-suited to study atomic-level deformations in mineral due to mechanical loading. Previous spectroscopic studies during mechanical testing of bone demonstrated that mechanical damage caused spectral shifts and that different changes in

collagen and mineral occur in response to mechanical loading and deformation [4-7]. Mineral spectral shifts were attributed to ionic movement and distortion. Polarized Raman spectroscopic imaging has been used to study the orientation and composition of cortical bone tissue [8-10]. In the present study, we used polarized Raman microspectroscopy to investigate about mineral crystallite behavior in bovine bone tissue under tensile loading in the elastic regime.

5.2 Specimen preparation

Three bovine bone specimens were milled from a bovine femur obtained from a local abattoir and stored at -80˚C until use. Each specimen was machined to about 3 cm in length and 2mm x 2mm in cross sectional area, while being irrigated with Calcium-buffered saline. To prepare the specimens for mechanical testing, the ends were embedded in a cold-setting acrylic and the exposed section was kept moist with gauze soaked in phosphate-buffered saline. A custom-made fixture was used to align the specimen. The thawed specimens were loaded onto a custom designed mechanical testing apparatus [6]. Under computer control, a DC motor was used to extend the specimen, while a load cell measured the applied load. The specimens were photo-bleached for 15 minutes at 200 mW prior to the experiments and kept moist throughout the experiment using phosphate buffered saline.

5.3 Polarized Raman spectroscopy

The Raman microspectroscopy system employed in the present study consisted of a research grade microscope (E600, Nikon USA), a 2 Watt 532 nm laser (Millennia II,

Spectra Physics, Mountain View, CA), and an f/1.8 axial transmissive spectrograph (HoloSpec, Kaiser Optical Systems, Inc., Ann Arbor, MI) [6]. The spectrograph was fitted with a 512 x 512 pixel back-illuminated EMCCD (iXon, Andor Technology, Belfast, Northern Ireland). The mechanical tester containing the specimen was placed on the micrometer stage with the laser line focused parallel to the long axis of the bone diaphysis. All Raman spectra were acquired through a 100X, 0.90 NA plan apochromatic objective (Nikon USA) with an exposure time of 30s. The polarization direction of the beam was selected using a half-wave plate and the collected Raman scatter was passed through an analyzing polarizer and directed onto the slit of the spectrograph. A wedge depolarizer after the analyzer eliminated intensity artifacts caused by the polarization dependence of the grating transmission efficiency. In all experiments the polarization of the incident laser beam was maintained parallel to the long axis of the diaphysis. The analyzer was adjusted to pass either the parallel or perpendicular component of the Raman scatter. The intensities (I) of the two polarized components of the Raman scatter are described by their excitation and detection polarizations: I_{par} and I_{perp} respectively.

5.4 Mechanical testing

The three bovine bone samples were loaded in tension in a series of discrete steps. The specimens were first loaded to 12.5 MPa, unloaded back to 0 MPa. Polarized Raman spectra were acquired from the mid-diaphysis region of the bone specimens at each loading magnitude.

5.5 Data analysis

Spectra were analyzed and peak fitted using GRAMS/AI 7.01 (Thermo Galactic, Waltham, MA) and the intensities of the characteristic mineral band, phosphate ν_1 (959 cm^{-1}), were measured. Depolarization ratios, i.e., the ratio of the intensity of the perpendicularly polarized component (I_{perp}) to that of the parallel polarized component (I_{par}), were calculated. Two-factor ANOVA (polarization direction x load magnitude) without replication was used to calculate significance in the shift in peak position and width on tensile loading. Paired t-test was performed on the depolarization ratio data from the first loading cycle.

5.6 Results

Table 5.1 compares the depolarization ratios and peak positions calculated for the phosphate ν_1 band (958 cm^{-1}) along the long axis of the bone diaphysis at various tensile loads. As the bone specimens were loaded in tension, the depolarization ratio (I_{perp}/I_{par}) decreased to about 0.6 times the original ratio ($p<0.05$). This significant decrease in depolarization ratio suggested that the mineral crystals have become more well-ordered when loaded in tension. As the specimens were unloaded, no significant increase in depolarization ratio was observed ($p>0.05$). No significant changes in phosphate peak position were observed on tensile loading of the bone tissue (table 5.1). The sample size and low signal-to-noise ratio made it difficult to ascertain if the bone mineral crystallites undergo a very small change in response to stress. The phosphate peak positions for the two polarization components of the Raman scatter were also not significantly different.

Figure 5.1 compares the full width at half maximum (FWHM) for the phosphate band at different tensile stresses. The two polarization components showed significantly different FWHM's ($p<0.01$) and underwent significantly different shifts in width at different applied loads ($p<0.01$). The width of the phosphate band increased by about 2.9 cm^{-1} and 3.2 cm^{-1} for the parallel and perpendicular components as the bone was loaded from 0 MPa to 12.5 MPa. On unloading to 0 MPa, the width decreased by 1.6 cm^{-1} and 1.8 cm^{-1} for the parallel and perpendicular components respectively.

5.7 Discussion

For murine cortical femora, the phosphate ν_1 band is highly polarized at zero load, indicating highly oriented mineral crystallites [10]. In this study, a depolarization ratio of about 0.5 was measured for bovine bone tissue at the starting zero load point. This indicates that the mineral crystallites in bovine bone are less well-ordered than the crystallites in murine cortical bone. While mineral crystallites are generally oriented parallel to the long axis of the bone in bovine plexiform tissue, there is a significant number of crystallites that are oriented in other directions [11]. Tensile loading of the bovine bone samples caused the phosphate bands to be more strongly polarized, which was reflected in a decrease in the depolarization ratio in the first loading step. This suggests that the mineral crystallites are becoming more ordered on extension of the bone tissue.

It is well-known that the crystallographic c-axes of the mineral crystallites align along the long axis of the collagen fibrils in bone tissue [12, 13]. Studies have reported that the

mineral particle orientation and the degree of alignment trace the orientation of the mineralized collagen fibrils within the bone material [14-16]. We suggest that the increase in orientation of the mineral crystallites at higher loads is due to collagen chains becoming extended, more aligned and tighter on application of tensile loads. The mineral crystallite orientation is increased because crystallites remain bonded to a matrix that is more-ordered with tensile loading. Comparison of the depolarization ratio of the phosphate band before and after loading suggests that the mineral crystallite ordering was not completely reversible in the time frame of the experiment.

That the mechanical properties of bone tissue are dependent on the properties of the mineral crystallites and the matrix proteins as well as the interactions between them is well-known [17]. Our present data confirms that mineral crystallites undergo change in response to macro-scale stress. The broadening of the phosphate band at higher stress is similar to that seen at increasing pressure [18]. The change in width can be attributed to both the strain on the crystallite and the change in its ordering on tensile loading. It is highly unlikely that these shifts in width reflect a change in the mineral crystallinity. This is in agreement with a recent NMR study on bone tissue which reported that even sub-physiological loads induce changes in phosphate ion spacing, but do not change the mineral structure itself [19].

Different widths of the phosphate band were observed in the parallel and perpendicular directions of the Raman scatter. When a uniaxial tensile stress is applied to a crystalline sample (i.e. mineral), the crystal lattice expands along the applied stress direction and

compresses along directions normal to the applied stress axis. These bidirectional strains on the mineral, i.e. tensile strain parallel to and compressive strain perpendicular to the long axis of bone, are reflected in the changes in phosphate peak width in the two polarized Raman spectra. This is in agreement with results from synchrotron diffraction studies which reported that mineral crystallites in bone tissue experience varying strains along different crystal planes and loading directions [20, 21]. There is greater load-induced broadening perpendicular to the collagen axis. It is known that increased pressure decreases anion-cation spacing in the a,b crystallographic plane in flourapatite [1]. We propose that the same behavior occurs in bone mineral, resulting in band width dispersion in the polarization direction perpendicular to the collagen axis.

We see very small changes in peak position of up to 0.8 cm^{-1} on tensile loading and unloading of the bovine bone tissue. Further experiments on a larger number of samples are necessary to comment on the effect of mechanical loading on the phosphate peak position. Peak width appears to be a more sensitive metric for the change in mineral crystallite lattice on tensile loading of bone tissue. The observed changes in the phosphate band width are likely a consequence of the changes in mineral crystallite structure and ordering due to the applied stress.

5.8 Conclusion

Milled bovine bone samples were elastically loaded in tension and the spectral changes in the phosphate band component were followed using polarized Raman spectroscopy. Significant orientation dependent changes in broadening of the phosphate bands were

observed at increased tensile loads and these were partially reversible on unloading of the bone tissue. Further, a decrease in the depolarization ratio of the phosphate band was observed on tensile loading, indicating that the mineral crystallites were becoming more ordered. Thus, our preliminary results show that polarized Raman spectroscopy can be used to study orientation dependent deformation of mineral crystallites in bone tissue. This technique can be extended to study deformation behavior of mineral crystallites in dehydrated or diseased bone tissue in response to applied load. Such studies will provide unique insight into the role of water and mineral-collagen interactions at the nano-scale and help understand the nano-scale mechanisms of bone fracture.

Table 5.1: Depolarization ratio and peak position of the phosphate v_1 band as a function of applied stress. Measurements from the parallel and perpendicular polarized components along the long axis direction are reported. (* $p<0.05$)

	Phosphate Depolarization Ratio	**Phosphate Peak Position (cm^{-1})**	
		Parallel polarization	Perpendicular polarization
0 MPa	0.49 ± 0.07	958.1 ± 0.22	957.8 ± 0.03
12.5 MPa (loading)	0.28 ± 0.01*	958.4 ± 0.50	958.0 ± 0.45
0 MPa (unloading)	0.39 ± 0.04	957.9 ± 0.20	958.1 ± 0.05

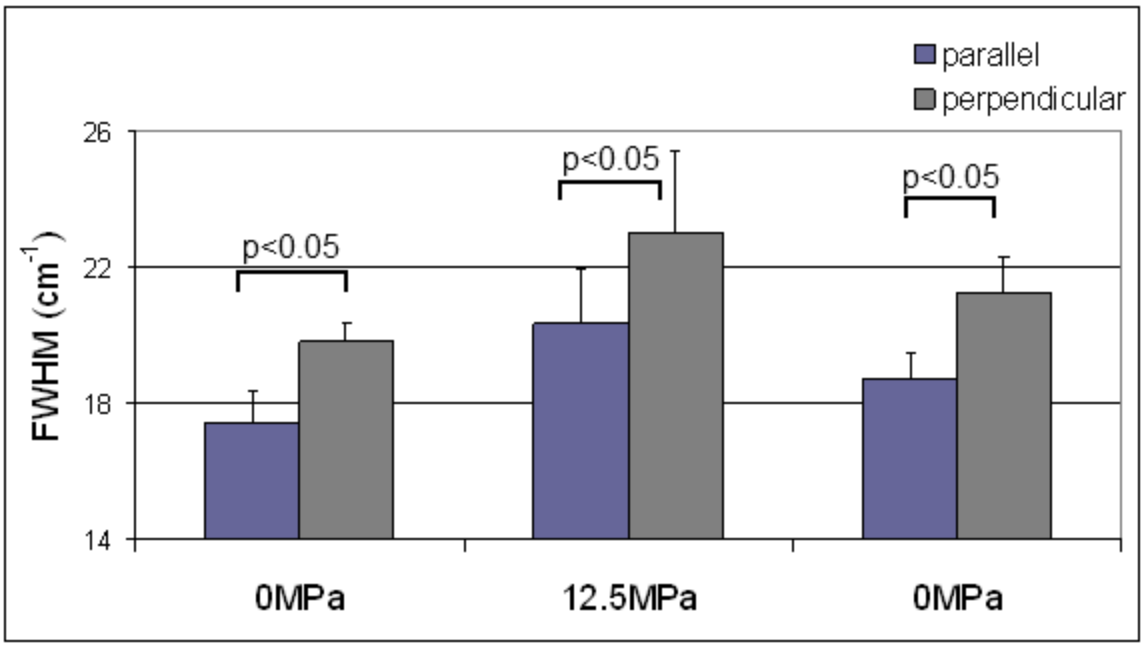

Figure 5.1 Full width at half maximum (FWHM) of the phosphate ν_1 band as a function of applied stress. The measurements from the parallel and perpendicular components of the Raman scatter along the long axis direction are reported.

References

[1] P. Comodi, Y. Liu, M. L. Frezzotti, Structural and vibrational behaviour of fluorapatite with pressure. Part II: in situ micro-Raman spectroscopic investigation, Physics and Chemistry of Minerals 28 (2001) 225-231.

[2] J. T. Pelton, L. R. McLean, Spectroscopic methods for analysis of protein secondary structure, Analytical Biochemistry 277 (2000) 167-176.

[3] P. Fratzl, H. S. Gupta, E. P. Paschalis, P. Roschger, Structure and mechanical quality of the collagen-mineral nano-composite in bone, Journal of Materials Chemistry 14 (2004) 2115-2123.

[4] A. Carden, R. M. Rajachar, M. D. Morris, D. H. Kohn, Ultrastructural changes accompanying the mechanical deformation of bone tissue: A Raman imaging study, Calcified Tissue International 72 (2003) 166-175.

[5] M. D. Morris, W. F. Finney, R. M. Rajachar, D. H. Kohn, Bone tissue ultrastructural response to elastic deformation probed by Raman spectroscopy, Faraday Discussions 126 (2004) 159-168.

[6] A. F. Callender, W. F. Finney, M. D. Morris, N. D. Sahar, D. H. Kohn, K. M. Kozloff, S. A. Goldstein, Dynamic mechanical testing system for Raman microscopy of bone tissue specimens, Vibrational Spectroscopy 38 (2005) 101-105.

[7] K. A. Dooley, J. McCormack, D. P. Fyhrie, M. D. Morris, Stress mapping of undamaged, strained, and failed regions of bone using Raman spectroscopy, Journal of Biomedical Optics 14 (2009) 044018-044018.

[8] M. Kazanci, P. Roschger, E. P. Paschalis, K. Klaushofer, P. Fratzl, Bone osteonal tissues by Raman spectral mapping: Orientation-composition, Journal of Structural Biology 156 (2006) 489-496.

[9] M. Kazanci, H. D. Wagner, N. I. Manjubala, H. S. Gupta, E. Paschalis, P. Roschger, P. Fratzl, Raman imaging of two orthogonal planes within cortical bone, Bone 41 (2007) 456-461.

[10] M. Raghavan, N. D. Sahar, R. H. Wilson, M.-A. Mycek, N. Pleshko, D. H. Kohn, M. D. Morris, Quantitative polarized Raman spectroscopy in highly turbid bone tissue, Journal of Biomedical Optics 15 (2010) 037001-037007.

[11] N. Sasaki, N. Matsushima, T. Ikawa, H. Yamamura, A. Fukuda, Orientation of bone mineral and its role in the anisotropic mechanical properties of bone--Transverse anisotropy, Journal of Biomechanics 22 (1989) 157-159, 161-164.

[12] W. Traub, T. Arad, S. Weiner, Three-dimensional ordered distribution of crystals in turkey tendon collagen fibers, Proceedings of the National Academy of Sciences 86 (1989) 9822-9826.

[13] S. Weiner, W. Traub, Organization of hydroxyapatite crystals within collagen fibrils, FEBS Letters 206 (1986) 262-266.

[14] O. Paris, I. Zizak, H. Lichtenegger, P. Roschger, K. Klaushofer, P. Fratzl, Analysis of the hierarchical structure of biological tissues by scanning X-ray scattering using a micro-beam, Cellular and Molecular Biology 46 (2000) 993-1004.

[15] S. Rinnerthaler, P. Roschger, H. F. Jakob, A. Nader, K. Klaushofer, P. Fratzl, Scanning small angle X-ray scattering analysis of human bone sections, Calcified Tissue International 64 (1999) 422-429.

[16] P. Roschger, B. M. Grabner, S. Rinnerthaler, W. Tesch, M. Kneissel, A. Berzlanovich, K. Klaushofer, P. Fratzl, Structural development of the mineralized tissue in the human L4 vertebral body, Journal of Structural Biology 136 (2001) 126-136.

[17] A. L. Boskey, T. M. Wright, R. D. Blank, Collagen and bone strength, Journal of Bone and Mineral Research 14 (1999) 330-335.

[18] O. de Carmejane, M. D. Morris, M. K. Davis, L. Stixrude, M. Tecklenburg, R. M. Rajachar, D. H. Kohan, Bone chemical structure response to mechanical stress studied by high pressure Raman spectroscopy, Calcified Tissue International 76 (2005) 207-213.

[19] P. Zhu, J. Xu, M. D. Morris, N. Sahar, D. H. Kohn, A. Ramamoorthy. Chemical structure effects on bone response to mechanical loading. In: Orthopedic Research Society Transactions. Las Vegas, NV; 2009. p. 0670.

[20] B. Giri, S. Tadano, K. Fujisaki, N. Sasaki, Deformation of mineral crystals in cortical bone depending on structural anisotropy, Bone 44 (2009) 1111-1120.

[21] J. D. Almer, S. R. Stock, Internal strains and stresses measured in cortical bone via high-energy X-ray diffraction, Journal of Structural Biology 152 (2005) 14-27.

CHAPTER 6

Conclusions and recommendations

6.1. Conclusions

Although bone fracture occurs at the organ level, physical mechanisms at the micro- and nano-scales underlie several physiologically important properties of bone. The sophisticated structure and interaction of collagen and mineral at the molecular level give rise to exceptional fracture resistance and mechanical capabilities at the whole bone level. Insights into such structure – function relationships across many spatial scales (nano to macro) are vital to understand transfer of loads and stresses, dissipation of energy, distribution of damage and resistance to cracking within the bone composite. However, there is still only limited understanding of how these structural and mechanical properties control bone quality and adapt in response to aging and disease.

As outlined in Chapter 1, the principal goal of this thesis is to investigate molecular structure and organization in bone tissue using Raman spectroscopy. Much of the challenge lies in studying the anisotropic behavior and nano-scale interactions of mineral and collagen components. This chapter discusses some of the key contributions of this thesis towards these challenges and highlights some useful avenues of inquiry for further work.

The results presented in Chapter 2 confirm that quantitative information on molecular orientation in bone tissue can be extracted from polarized Raman spectra. It was demonstrated for the first time that orientation distributions of mineral and collagen can be calculated simultaneously and even from intact, non-deproteinated bone tissue. The profound effect of collagen genetic disorder on collagen/mineral ordering in Osteogenesis Imperfecta was observed using polarized Raman spectroscopy. Depolarization problems due to tissue turbidity can be overcome by choosing an appropriate objective. This work suggests that polarized Raman spectroscopy will be a powerful tool to investigate molecular order and composition in healthy and diseased bones.

Chapters 4 and 5 examined the effects of disrupting the aqueous environment and tensile loading on the molecular organization in bone tissue. Equilibration of bone with D_2O not only affected collagen conformation but also mineral properties. Disruption of matrix hydration caused collagen stiffening which in turn compressed the mineral crystallite lattice as evidenced by shifts in peak positions and widths of the mineral Raman bands. On deformation of bone tissue by tensile loading, changes in mineral lattice strains and ordering were observed. Changes in the widths of the mineral Raman bands in the polarized Raman spectra revealed direction-dependent strains in the mineral lattice. These Raman spectroscopic studies highlight the influence of hydrogen bonding on mineral and matrix interactions and allow detection of mineral behavior at the nano-scale.

A ‘top down’ approach to elucidate the complexity of age-related changes in bone tissue was presented in Chapter 3. A higher order analysis method, data mining, was

successfully applied to describe changes in femoral material properties between young and old mice. RadViz and VizRank algorithms were used to infer the underlying non-linear relationships and to select the most informative and biologically relevant compositional (Raman) and mechanical (nanoindentation) properties. Combinations of these selected measures offered good classification of bone quality changes that occur with aging. These results suggest that the complexities of tissue quality far exceed the capability of individual measures, either compositional or mechanical, to provide complete information on bone quality. Further, data mining will be more effective as a general strategy for discovering markers of bone quality than traditional linear regression methods.

6.2 Recommendations

Going forward, the models describing polarized Raman spectroscopic approaches will increase in complexity to better describe the sophisticated bone material. The current study made a reasonable assumption of a uniaxially oriented material with cylindrical symmetry for calculating molecular orientation distributions. However, it might be worthwhile to investigate molecular orientations assuming a biaxially oriented material. In this case, polarized Raman spectra have to be measured in backscattering as well as right-angle scattering geometries [1]. Although this increases the experimental complexity, biaxial models may improve the accuracy of orientation calculations. This can be verified by comparing molecular orientation distributions with and without the assumption of a biaxial orientation against those obtained by X-ray scattering. A variety of bone-related research areas will benefit from this quantitative molecular orientation

approach combined with other analytical tools. Some of these include bone diseases (such as osteogenesis imperfecta, Paget's disease, osteomalacia, osteonecrosis and osteoporosis), biomineralization, osseointegration, and tissue engineering [2-6]. Information on molecular orientation will provide better insights into macroscopic mechanical properties, crystallite growth direction, or structural optimization.

Raman spectroscopy is widely used as an indirect probe of crystallite behavior in response to deformation. Our preliminary results suggest that polarized Raman spectra provide information on the anisotropy-dependent deformation of mineral crystallites. Future work will involve investigating stress/strain distributions across a wider range of physiological loads to establish correlations between structural anisotropy and deformation behavior at the nano-scale. Challenges will involve shortening measurement times and employing dynamic mechanical loading while still maintaining a good signal-to-noise ratio for the Raman scatter. Extending this technique to bones from different anatomical locations will throw more light on adaptation of nano-scale mineral deformation and orientation to macro-scale functional requirement [7]. For instance, femur and tibia in the lower limbs resist bending while vertebrae in the chest resist compression. Another area of application will be to study the effect of metabolic disorders, and aging on molecular order and mineral deformation behavior. Understanding how nano-scale mechanisms adapt to exercise, nutrition, aging, therapy and disease will prove critical in bridging the gap between the nano- and macro-scale properties of bone.

Although the water component in bone is often overlooked, our work highlights the importance of the hydrated environment within bone tissue. Hence, the traditional two phase composite model of bone has to be extended to include water [8]. Future work should address the role of solvent environment in influencing the organization and interaction of mineral and matrix at the ultrastructural scale. By dehydrating and/or replacing water with solvents like ethanol, acetone, urea, etc., hydrogen bonding effects on molecular deformation mechanisms and ordering can also be studied using polarized Raman spectroscopy. Another avenue of enquiry is to study nano-scale behavior in bones from different species that have different volumetric combinations of mineral, matrix and water. These experiments will provide new insights on the role of water in bone ultrastructure. All these studies put together may impact the medical field by providing important information on the mechanisms of disease and aging which will help in designing better therapies.

The Holy Grail in bone material research is to fully understand how the hierarchical levels and composite nature contribute to its varied physiological roles, particularly to maintain bone quality. However, most studies have focused on a single type of analysis (mechanics, composition, microdamage, etc) or a single hierarchical level for investigation of bone quality. It is clear that single measures are unlikely to provide complete information about bone quality or age- and disease-related skeletal changes. There is a need to implement strategies that integrate data from different analytic techniques and different hierarchical and time scales. More attention should be focused on the use of multiple metrics to improve overall predictive accuracy and to develop

stable models that reflect bone dynamics. With the increasing use of atomistic and molecular simulations in bone materials research, approaches such as data mining and multi-scale models are necessary to bridge the gap in time- and length-scales [9, 10]. By understanding how nano-, micro- and macro-scale properties of bone control and respond to a variety of biochemical and mechanical cues, we might be able to better understand skeletal fragility and identify biomarkers or metrics of bone quality that are clinically significant.

Most techniques that assess aspects of bone quality are confined to research settings. It is important to identify biologically relevant bone quality metrics that can be measured non-invasively in the clinic. Imaging techniques such as Raman tomography, quantitative ultrasound, high-resolution computed tomography and MRI show good translational potential [11-13]. Another important approach is identifying genes relevant to fracture susceptibility by performing genetic analyses on bone [14]. Fracture risk prediction can be improved by involving information from different hierarchical scales because bone is a complex organ. Future work on fracture risk algorithms should consider bone quality metrics, biomarkers and fracture susceptible genes in addition to areal bone mineral density and clinical risk factors. With osteoporosis and musculoskeletal disorders posing a global challenge, fracture risk assessment using bone mineral density is costly and often unavailable [15, 16]. Hence, researchers should also address the development of effective and inexpensive tools for fracture risk prediction and diagnosis that are appropriate for low-resource settings.

References

[1] D. I. Bower, Orientation distribution functions for biaxially oriented polymers, Polymer 23 (1982) 1251-1255.

[2] F. Rauch, F. H. Glorieux, Osteogenesis imperfecta, The Lancet 363 (2004) 1377-1385.

[3] P. Chavassieux, E. Seeman, P. D. Delmas, Insights into material and structural basis of bone fragility from diseases associated with fractures: how determinants of the biomechanical properties of bone are compromised by disease, Endocrine Reviews 28 (2007) 151-164.

[4] P. I. Okagbare, F. W. L. Esmonde-White, S. A. Goldstein, M. D. Morris, Development of non-invasive Raman spectroscopy for in vivo evaluation of bone graft osseointegration in a rat model, Analyst 135 (2010) 3142-3146.

[5] S. Weiner, Biomineralization: A structural perspective, Journal of Structural Biology 163 (2008) 229-234.

[6] B. Stevens, Y. Yang, A. Mohandas, B. Stucker, K. T. Nguyen, A review of materials, fabrication methods, and strategies used to enhance bone regeneration in engineered bone tissues, Journal of Biomedical Materials Research Part B: Applied Biomaterials 85B (2008) 573-582.

[7] B. Demes, In vivo bone strain and bone functional adaptation, American Journal of Physical Anthropology 133 (2007) 717-722.

[8] M. L. Oyen, M. Galli. Bone Composite Mechanics Related to Collagen Hydration State. In: K. Garikipati, E. M. Arruda, editors. IUTAM Symposium on Cellular, Molecular and Tissue Mechanics: Springer Netherlands; 2008. p. 269-276.

[9] M. J. Buehler, S. Keten, T. Ackbarow, Theoretical and computational hierarchical nanomechanics of protein materials: Deformation and fracture, Progress in Materials Science 53 (2008) 1101-1241.

[10] A. J. Weiss, A. Lipshtat, J. I. Mechanick, A systems approach to bone pathophysiology, Annals of the New York Academy of Sciences 1211 (2010) 9-24.

[11] M. V. Schulmerich, J. H. Cole, K. A. Dooley, M. D. Morris, J. M. Kreider, S. A. Goldstein, S. Srinivasan, B. W. Pogue, Noninvasive Raman tomographic imaging of canine bone tissue, Journal of Biomedical Optics 13 (2008) 020506-020503.

[12] K. S. Davison, D. L. Kendler, P. Ammann, D. C. Bauer, D. W. Dempster, L. Dian, D. A. Hanley, S. T. Harris, M. R. McClung, W. P. Olszynski, C. K. Yuen, Assessing fracture risk and effects of osteoporosis drugs: bone mineral density and beyond, The American Journal of Medicine 122 (2009) 992-997.

[13] M. L. Bouxsein, Technology Insight: noninvasive assessment of bone strength in osteoporosis, Nature Clinical Practice Rheumatology 4 (2008) 310-318.

[14] K. J. Jepsen, Systems analysis of bone, Wiley Interdisciplinary Reviews: Systems Biology and Medicine 1 (2009) 73-88.

[15] R. Handa, A. Ali Kalla, G. Maalouf, Osteoporosis in developing countries, Best Practice & Research Clinical Rheumatology 22 (2008) 693-708.

[16] N. Harvey, E. Dennison, C. Cooper, Osteoporosis: impact on health and economics, Nature Reviews Rheumatology 6 (2010) 99-105.

APPENDIX

A1. Determination of the orientation distribution function

The orientation of a molecule is a description of its spatial position with respect to a macroscopic xyz coordinate system as described by three Euler's angles *(θ, φ, ε)*. For a complete orientation description of the molecule, an orientation distribution function *N(θ, φ, ε)* is required. By assuming a uniaxial system with cylindrical symmetry, the orientational distribution function only depends on the angle θ and can be expanded in a series of even Legendre polynomials.

$$N(\theta) = \sum_{1}^{even}\left(i + \frac{1}{2}\right) \cdot \langle P_i \rangle \cdot P_i(\cos(\theta)) \tag{1}$$

where $P_i(\cos\theta)$ is the Legendre polynomial of degree *i*, and its average value, also defined as the orientation order parameter, is

$$\langle P_i \rangle = \int_0^{\pi} P_i(\cos\theta) \cdot N(\theta) \cdot \sin(\theta) d\theta \tag{2}$$

Using polarized Raman spectroscopy, the order parameters $\langle P_i \rangle$ can be obtained for $i = 2$ and 4 only. With only these order parameters (hereafter referred to as P_2 and P_4), the orientation distribution function, N(θ), can be predicted as the most probable orientation distribution function by maximizing the information entropy of the distribution:

$$S[N(\theta)] = -\int_0^{\pi} N(\theta) \cdot \ln(N(\theta)) \cdot \sin(\theta) d\theta \tag{3}$$

This is subject to the probability constraint:

$$\int_0^{\pi} N(\theta)\cdot\sin(\theta)d\theta = 1 \tag{4}$$

Lagrangian multipliers, λ_2 and λ_4, are introduced to take care of the constraints while defining the maximum. λ_2 and λ_4 are numerically calculated from equation 2 and from the first derivative of equation 3. The most probable distribution function is then given by:

$$N(\theta) = \frac{\exp\left[\lambda_2 P_2 + \lambda_4 P_4\right]}{\int_{-1}^{+1}\exp\left[\lambda_2 P_2 + \lambda_4 P_4\right]d(\cos(\theta))} \tag{5}$$

To determine the order parameters, P_2 and P_4, Raman depolarization ratios are calculated for different orientations of the incident laser with respect to the sample. The depolarization ratios, R_1 and R_2, are dependent on the collection geometry and the Raman tensor components.

$$R_1 = \frac{I_{zx}}{I_{zz}} = \frac{A\left\langle(\alpha_{zx})^2\right\rangle + B\left\langle(\alpha_{zy})^2\right\rangle}{A\left\langle(\alpha_{zz})^2\right\rangle + B\left\langle(\alpha_{zy})^2\right\rangle} \tag{6}$$

$$R_2 = \frac{I_{xz}}{I_{xx}} = \frac{A\left\langle(\alpha_{xz})^2\right\rangle + B\left\langle(\alpha_{xy})^2\right\rangle}{A\left\langle(\alpha_{xx})^2\right\rangle + B\left\langle(\alpha_{xy})^2\right\rangle} \tag{7}$$

where I_{ij} is the scattered Raman intensity polarized in the *j* direction when the incident light is polarized along the *i* direction *(i, j being x* or *z)*. Constants A and B quantify the influence of objective semi-angular aperture (θ_m) and sample refractive index (n).

$$A = \pi^2\left(\frac{4}{3} - \cos\theta_m - \frac{1}{3}\cos^3\theta_m\right) \tag{8}$$

$$B = 2\pi^2\left(\frac{2}{3} - \cos\theta_m - \frac{1}{3}\cos^3\theta_m\right) \tag{9}$$

$$\theta_m = \sin^{-1}(NA/n) \tag{10}$$

$\left\langle (\alpha_{ij})^2 \right\rangle$ is the average component of the Raman tensor *(i, j being x, y, z)* and is related to the order parameters, P_2 and P_4, as follows:

$$\left\langle (\alpha_{xx})^2 \right\rangle = \frac{1}{15}c - \frac{2}{21}dP_2 + \frac{3}{35}bP_4 \tag{11}$$

$$\left\langle (\alpha_{xz})^2 \right\rangle = \left\langle (\alpha_{zx})^2 \right\rangle = \left\langle (\alpha_{zy})^2 \right\rangle = b\left(\frac{1}{15} + \frac{1}{21}P_2 - \frac{4}{35}P_4 \right) \tag{12}$$

$$\left\langle (\alpha_{zz})^2 \right\rangle = \frac{1}{15}c + \frac{4}{21}dP_2 + \frac{8}{35}bP_4 \tag{13}$$

$$\left\langle (\alpha_{xy})^2 \right\rangle = b\left(\frac{1}{15} - \frac{2}{21}P_2 + \frac{1}{35}P_4 \right) \tag{14}$$

where $b = \alpha_3{}^2 (1-a)^2$ (15)

$$c = \alpha_3{}^2 (3 + 4a + 8a^2) \tag{16}$$

$$d = \alpha_3{}^2 (3 + a - 3a^2) \tag{17}$$

The Raman tensor parameter, *a*, is determined from the depolarization ratio of an isotropic sample, R_{iso}, by setting $P_2 = P_4 = 0$ in equations 8-11.

$$R_{iso} = R_1 = R_2 \tag{15}$$

The order parameters, P_2 and P_4, are obtained using the experimentally measured R_1 and R_2 and the parameter *a* (see Appendix A2 for MATLAB code). The limiting values for P_2 and P_4 are 1 and -0.5 for perfect orientation at 0˚ and 90˚ from the axis of reference. Based on the values of P_2 and P_4, Lagrangian multipliers are calculated using equations 2 and 3 (see Appendix A3 for MATLAB code). Finally, the Lagrangian multipliers are inserted into equation 5 to plot the most probable orientation distribution function (see Appendix A4 for MATLAB code).

A2. MATLAB program code for calculating order parameters, P_2 and P_4, from Raman depolarization ratios, R_1 and R_2

```
% polarization.m: Calculates the orientation order parameters
% Requires depolarization ratios (R1, R2 and Riso) as inputs
% Mekhala Raghavan, University of Michigan

% Enter sample refractive index and numerical aperture of objective
n=1.55;
NA=0.90;
theta=asind(NA/n)

% Calculate constants A and B based on theta.
A=(pi^2)*(1.33-cosd(theta)-((cosd(theta))^3/3))
B=(2*pi^2)*(0.67-cosd(theta)+((cosd(theta))^3/3))

% Calculate parameter 'a' from the isotropic depolarization ratio.
% Roots of the polynomial gives 'a'. Use one of the two.
riso=0.44;
poly=[08*riso-1 4*riso+2 3*riso-1];
roots(poly)

% Solve for order parameters, P2 and P4.
% Enter depolarization ratios (R1 & R2), a (polynomial root), A & B
% X gives P2 and P4.

a=-0.147;
A=3.3157;
B=0.705;
R1=0.65;
R2=0.56;
P21=((((4*A*(3+a-4*a^2))+(B*(1-a)^2))*R1)-((A+B)*(1-a)^2))/21;
P22=(-(2*((A*(3+a-4*a^2))+(B*(1-a)^2))*R2)-((A-2*B)*(1-a)^2))/21;
P41= ((R1*(8*A-4*B)*(1-a)^2)+(4*(A+B)*(1-a)^2))/35;
P42=((3*R2*(A+B)*(1-a)^2)-((B-4*A)*(1-a)^2))/35;
C1=((R1*(A*(3+4*a+8*a^2)+B*(1-a)^2))-((A+B)*(1-a)^2))/15;
C2=((R2*(A*(3+4*a+8*a^2)+B*(1-a)^2))-((A+B)*(1-a)^2))/15;
A=[P21 P41
  P22 P42];
B=[-C1
  -C2];
X=A\B
```

A3. MATLAB program code for calculating Lagrangian multipliers, λ_2 and λ_4 , from order parameters, P_2 and P_4

```
% Lagrangian Multipliers for Maximum Entropy
% Determines Lagrangian multipliers L2 and L4 using order parameters P2 and P4
% Requires Appendix A2 results as input
% Mekhala Raghavan & Raghu Kainkaryam, University of Michigan

% lagmult_int_main.m: Main File - where parameters can be set
% this script calls for lagmult_int_opt.m, lagrange_int.m listed below
tic
% Set P2 and P4
P2=-0.37;
P4=0.17;
P=[P2 P4];
% L_orig=[L2 L4];
% Guess for L2, L4
L0=[0 0];
options = optimset('Display','iter','MaxIter',100,'TolX',1e-8,'TolFun',1e-10);
[x,fval,exitflag] = fsolve(@(x)lagmult_int_opt(x,P),L0,options);
% L_orig
L_opt=x
residual=sum(fval.^2)
exitflag
P_orig=P
[P2_opt P4_opt]=lagrange_int(L_opt(1),L_opt(2));
P_opt=[P2_opt P4_opt]
time_mins=toc/60


% lagmult_int_opt.m: Optimization File - sets up the search for L2 & L4
% this script calls for lagrange_int.m described below
function F=lagmult_int_opt(L,P)
[P2 P4]=lagrange_int(L(1),L(2));
F=[P(1)-P2;P(2)-P4];
% End of Function


%lagrange_int.m: Integral File - Calculates P2 & P4 from L2 & L4
% this script calls for P2top.m, P4top.m and Pdenom.m listed below
function [P2 P4]=lagrange_int(L2,L4)
del_t=1e-2;
t_min=0;
t_max=1;
t=t_min:del_t:t_max;
% MATLAB's integration method
```

```
P2=quad(@(t)P2top(t,L2,L4),t_min,t_max);
P4=quad(@(t)P4top(t,L2,L4),t_min,t_max);
denom=quad(@(t)Pdenom(t,L2,L4),t_min,t_max);
P2=P2/denom;
P4=P4/denom;
% End of Function
```

```
%P2top.m: For integration
function f = P2top(t,L2,L4)
f=0.5*(3*t.^2-1).*exp((L2/2)*(3*t.^2-1)+(L4/8)*(35*t.^4-30*t.^2+3));
% End of Function
```

```
%P4top.m: For integration
function f=P4top(t,L2,L4)
f = 0.125*(35*t.^4-30*t.^2+3).*exp((L2/2)*(3*t.^2-1)+(L4/8)*(35*t.^4-30*t.^2+3));
% End of Function
```

```
%Pdenom.m: For integration
function f=Pdenom(t,L2,L4)
f=exp((L2/2)*(3*t.^2-1)+(L4/8)*(35*t.^4-30*t.^2+3));
% End of Function
```

A4. MATLAB program code for calculating most probable orientation distribution function from Lagrangian multipliers, λ_2 and λ_4

```
% odf.m: Calcualtes most probable orientation distribution function
% % Determines most probable ODF from Lagrangian multipliers, L2 and L4
% Uses p2cosx and p4cosx derivation to determine ODF
% Requires Appendix A2 and A3 as inputs
% Mekhala Raghavan, University of Michigan

clear
syms l2 l4 x y z P2 P4 t
L2=-3.99;
L4=5.83;
x= (0:90);
y=cosd(x);
z=sind(x);

% to get answer in radians
% x= 0:.01:2*pi;
% y=cos(x);
% z=sin(x);

P2=0.5*((3*y.^2)-1);
P4=0.125*((35*y.^4)-(30*y.^2)+3);
num=exp(L2*P2+L4*P4);
deno=num.*z;
den=trapz(deno);
func=num/den;
% multiply by sind(x) considering uniaxial cylindrical symmetry
func2=func.*z;
% plots the most probable odf
plot(x,func2,'r')
% calculate first moment (mean) of distribution which gives the
% average orientation angle
angle=trapz(x.*func2)
```

A5. RadViz multidimensional visualization

RadViz (radial coordinate visualization) uses an analog of Hooke's law to map a set of n-dimensional points into a 2D plane. The main advantage of using such a method is that no projections of data are necessary and a global view of the multidimensional data is provided.

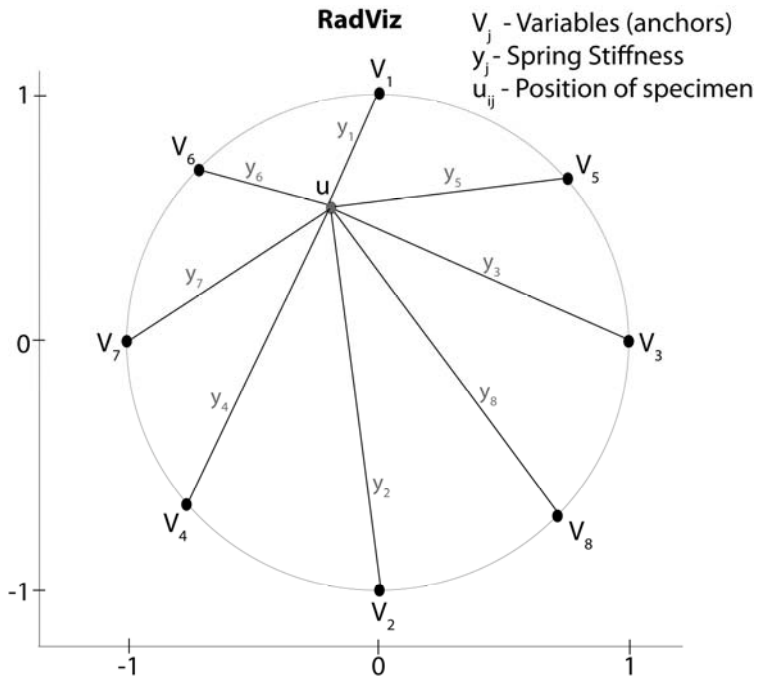

Figure A1: Definition of RadViz mapping

Input:

i is the number of specimens, where i= 1 to m

j is the number of variables (dimensions), where j=1 to n

y_{ij} is the value of variable j for specimen i

Output:

u_i and u_j are the resulting specimen coordinates in 2D space, i= 1 to m

Algorithm:

1. The dimension anchors (variables), V_j, are equally spaced around the perimeter of a circle (see Figure A1)
2. The data for each variable is normalized to interval <0, 1>

   $$\bar{x}_{ij} = \left(x_{ij} - \min_j\right)/\left(\max_j - \min_j\right) \qquad (1)$$

3. The location of the specimen point, u_i, in the 2D plane is next determined as follows:

   - For each anchor (variable) V_j, the stiffness of the spring connecting it to u_i is calculated to be y_j, where

     $$y_j = \sum_{j=1}^{n} \bar{x}_{ij} \qquad (2)$$

   - The location of u_i is the point where all spring forces are in equilibrium (according to Hooke's law of mechanics)

     i.e. $$\sum_{j=1}^{n}\left(\vec{V}_j - \vec{u}\right)y_j = 0 \qquad (3)$$

   - The position of $u = [u_1, u_2]$ is calculated for each specimen i using:

     $$u_1 = \sum_{j=1}^{n} y_j \cos\left(\alpha_j\right) \Big/ \sum_{j=1}^{n} y_j \qquad (4)$$

     $$u_2 = \sum_{j=1}^{n} y_j \sin\left(\alpha_j\right) \Big/ \sum_{j=1}^{n} y_j \qquad (5)$$